LIGHT SCATTERING EXPERIMENTS ON BROWNIAN MOTION IN SHEAR FLOW AND IN COLLOIDAL CRYSTALS

proefschrift

ter verkrijging van de graad van doctor aan de
Technische Universiteit Eindhoven, op gezag van
de Rector Magnificus, prof. ir. M. Tels, voor een
commissie aangewezen door het College van Dekanen
in het openbaar te verdedigen op
dinsdag 12 februari 1991 te 16.00 uur

door

Jacobus Johannes Derksen

geboren te Raalte

Dit proefschrift is goedgekeurd door de promotoren
prof. dr. ir. P.P.J.M. Schram
en
prof. dr. B.U. Felderhof

Co-promotor
dr. ir. W. van de Water

Daar bevindt zich een andere wereld.

Jan Siebelink

Contents

Chapter 1 INTRODUCTION

1.1. Brownian motion and dynamic light scattering

In 1827 the Scottish botanist Robert Brown observed under the microscope that pollen grains in water were in a continual state of erratic motion. It appears that all particles of colloidal size ($10^{-8} - 10^{-6}$ m) exhibit this Brownian motion when they are immersed in a fluid. The driving force of Brownian motion is provided by the thermally excited fluid molecules; they constantly collide with the much larger particles. Because of the random nature of the driving force both the particle velocity and the particle position are stochastic processes. Chandrasekhar (1943) showed that the characteristic time of the velocity fluctuations (denoted by β^{-1}) is determined by the particle's mass m and the Stokes resistance of the particle in the fluid; for a sphere: $\beta^{-1} = m/6\pi\eta a$ (a is the sphere radius; η is the dynamic viscosity of the fluid). β^{-1} is much larger than the correlation time of the random driving force. For times much larger than β^{-1} one arrives at the Stokes-Einstein result (Einstein 1905) that qualifies Brownian motion as a diffusion process, i.e. the mean-square displacement of a Brownian particle is proportional to time. The diffusion constant of a spherical particle equals $k_B T/6\pi\eta a$ (k_B is the Boltzmann constant, T is the absolute temperature).

Experimental work on the motion of small particles in a fluid received major impulses with the introduction of intensity interferometry or light beating spectroscopy (Hanbury-Brown & Twiss 1956) and with the invention of the laser. Intensity fluctuations of light scattered by a sample of Brownian particles illuminated with a beam of coherent light contain information on particle position fluctuations. The statistical properties of the fluctuating light intensity are determined by measuring its time correlation function. Nowadays standard equipment can measure correlation functions with a resolution down to 10^{-7} s. Hence, most dynamic light scattering experiments on Brownian motion are in the diffusion regime. The characteristic time of the light intensity fluctuations is then of the order of λ^2/D ; λ is the wavelength of the used light; D is the diffusion constant of the particle.

A central problem in the field of dynamic light scattering experiments on Brownian motion is the interpretation of the measured data (scattered light

correlation functions) in terms of more familiar properties of the sample of particles in the fluid. This may be elucidated by an example. If a sample of non-interacting particles with uniform size is probed the fluctuating scattered light intensity in a point has only one characteristic time that can be obtained easily when a correlation function is measured. The particle size can be calculated from this characteristic time. If the particle size is distributed over a finite-size interval one could expect that an accurately measured correlation function can be decomposed in a spectrum of characteristic times and therefore in a particle size distribution function. This decomposition, however, is an ill conditioned problem; McWhirter & Pike (1978) showed that already the slightest noise in the correlation function can lead to large errors in the size distribution function. The same kind of problem arises when Brownian motion is affected by, for instance, particle interactions, macroscopic fluid flow or external force fields, i.e. systems that involve several characteristic times. Sometimes a special choice of the experimental conditions or an extension of the elementary dynamic light scattering experiment provides the possibility of measuring well interpretable correlation functions in rather complex systems. In this thesis two such quite unconventional light scattering experiments on Brownian motion are described. The first is a cross-correlation experiment on Brownian motion that is affected by an externally applied shear flow. The second experiment studies the dispersion of Brownian waves in a so-called colloidal crystal, a solidlike structure of charged colloidal particles in a fluid.

1.2. Thesis overview

In chapter 2 a summary of the basic concepts of dynamic light scattering off colloidal particles is presented. A central theme in this chapter is the relation between the measured scattered intensity correlation function and the, from a theoretical viewpoint desired, second-order scattered electric field correlation function. There are two well known ways to establish this relation (Jakeman 1974). The starting point of the first is the assumption of Gaussian light scattering. Often the scattered light is the sum of a large number of independent contributions. The scattered electric field in a point then has Gaussian statistics;

higher order moments of the electric field (the intensity correlation function is a fourth-order moment) can be expressed in terms of first- and second-order moments. A second and direct way to measure the second-order electric field correlation function of the scattered light is the measurement of the intensity correlation function of scattered light that is coherently mixed with a much more intense reference light beam; so-called heterodyne scattering. In section 2.5 a unique setup for heterodyne experiments is described. In section 2.4 photon correlation is introduced. This is a very fast and efficient technique to obtain intensity correlation functions under low light level circumstances (Jakeman & Pike 1969; Schätzel 1987).

Our experiments on Brownian motion in shear flow (described in chapter 3) owe much to the work by Fuller *et al.* (1980) and by Foister & Van de Ven (1980). Foister & Van de Ven derived explicit expressions for the probability density of the position of a Brownian particle in shear flow. Fuller *et al.* distinguished the various time scales involved in a light scattering experiment on Brownian motion in shear flow. The two most important are the time scale of (deterministic) convective particle motion $\tau_c = \lambda/\gamma d$ (where λ is the wavelength of the used light, d is the linear size of the scattering volume and γ is the shear rate) and the time scale on which the influence of shear on Brownian motion is visible: $\tau_b = \gamma^{-1}$. The ratio τ_c/τ_b equals λ/d which in general is much smaller than one. The conventional light scattering experiment is dominated by the shortest time scale and therefore the fluctuations on the Brownian motion time scale τ_b are obscured by the fluctuations due to deterministic motion. A cross-correlation experiment, i.e. an experiment that probes light scattered in two separate directions, under certain circumstances introduces a time delay of the order of τ_b . This allows us to observe the effects of Brownian motion in shear flow on the scattered light correlation function. A similar cross-correlation experiment was reported by Keveloh & Staude (1983). They were, however, interested in point measurements of shear rates in a flow, not in Brownian motion.

In a colloidal crystal the identical colloidal particles are arranged in a lattice. In the dilute crystals described in this thesis electrostatic repulsion between the charged particles is responsible for the long-range crystalline order. An extensive review on colloidal crystals is given by Pieranski (1983). In ordered colloids hydrodynamic interaction is much more important than in random swarms of

particles in a fluid; hydrodynamic interaction enters at order $\phi^{1/3}$ instead of order ϕ, where ϕ is the volume fraction occupied by the spheres (Hasimoto 1959; Saffman 1973). Because of the regular arrangement of the colloidal particles, explicit expressions for the frequency and damping of crystal waves initiated by Brownian motion can be derived (Hurd *et al.* 1982 and 1985; Felderhof & Jones 1986 and 1987). The damping is intimately connected to hydrodynamic interaction. It therefore depends on the wavelength and the polarization direction of the crystal waves: longitudinal waves are strongly damped because they always show backflow; long-wavelength transverse waves are characterized by coherent motion of fluid and particles, their relatively low damping is determined by the relaxation of shear modes in the fluid (Joanny 1979).

The colloidal crystals that are discussed in this thesis are formed of monodisperse spheres with a typical diameter of 0.1 μm suspended in water. The lattice parameter is typically 1 μm, so that crystallography can be done with visible light. Light that is scattered by Brownian crystal waves has been probed with photon correlation spectroscopy (Hurd *et al.* 1982) in order to measure the damping and the frequency of the waves as a function of their wavelength. In contrast to their hydrodynamic theory the experimental findings by Hurd *et al.* showed that transverse waves have finite damping in the long-wavelength limit. This discrepancy prompted Felderhof & Jones to reconsider the original hydrodynamic theory (1986) and to introduce electrodynamic effects caused by the motion of counter ions in the fluid (1987). We performed light scattering experiments on colloidal crystals similar to the experiments by Hurd *et al.*. Our attention was focussed on the shape of scattered light correlation functions and on long-wavelength transverse modes. The experiments employed the flexible heterodyne setup described in section 2.5. This allowed us to measure unambiguously the shape of correlation functions. The measurements on the weakly damped long-wavelength transverse crystal modes demonstrate that sample-cell walls can have a strong impact on crystal dynamics.

Chapter 4 is a review on colloidal crystal dynamics, including the electrodynamic effects introduced by Felderhof & Jones (1987). In chapter 5 the dynamic light scattering experiment on colloidal crystals is described and results are presented.

Chapter 2 DYNAMIC LIGHT SCATTERING TECHNIQUES

2.1. Introduction

Illumination of a sample of Brownian particles with coherent light reveals the fluctuating particle positions, even if these positions change on a scale comparable to the wavelength of light. The statistical properties of the fluctuating scattered light intensity are intimately connected to the statistical particle positions. The scattering of light, therefore, is a prime experimental tool for the study of Brownian motion.

With the advent of fast digital electronics it became possible to measure correlation functions of the scattered light intensity in real time through registration of individual photon counts. This chapter will elucidate the relation between photon correlation functions and correlations of particle positions.

Light scattering experiments can be done in a variety of configurations, one example is the situation where scattered light is mixed with part of the incident beam, so-called heterodyne scattering. This chapter will also describe a unique setup for performing heterodyne experiments that has emerged from the research described in this thesis.

2.2. Light scattering

The basic light scattering setup is sketched in Fig. 2.1. Linear polarized light from the incident laser beam (with wavevector $\underline{k}_i$) is scattered by a collection of N Brownian particles at positions $\underline{r}_j(t)$, $j = 1...N$. The detector accepts scattered light with wavevector $\underline{k}_s$, defining the scattering angle θ. The light scattered by single pointlike particles is linearly polarized. If the polarization direction of the incident beam is perpendicular to the plane defined by $\underline{k}_i$ and $\underline{k}_s$, the polarization direction of the scattered light at the detector equals that of the incident beam. The only non-zero component of the scattered electric field at the detector surface $\underline{R}$ is then

$$e_s(\underline{R},t) = E(\underline{R},t)\, e^{i(\underline{k}_s.\underline{R}-\omega t)} . \qquad (2.1)$$

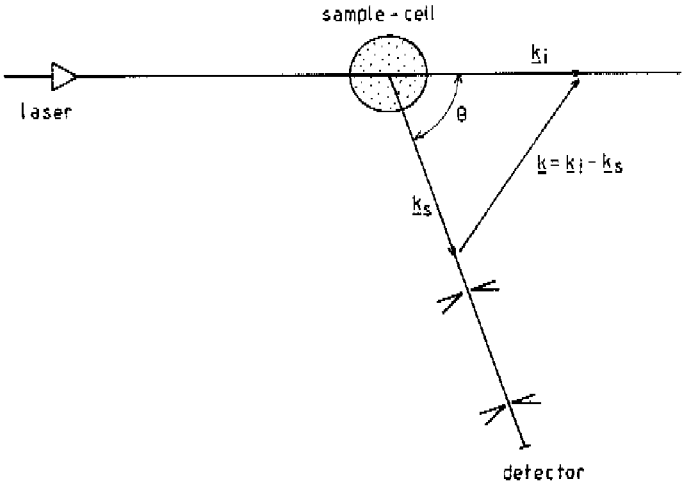

Fig. 2.1 Schematical experimental setup for dynamic light scattering experiments. Light with wave vector $\underline{k}_i$ emerges from a laser and strikes the sample cell. The scattered light wave vector $\underline{k}_s$ is defined through two pinholes.

In the single-scattering Born approximation the scattered field amplitude $E(\underline{R},t)$ becomes:

$$E(\underline{R},t) = \sum_{j=1}^{N} E_0[\underline{r}_j(t)]\, e^{i\underline{k}\cdot\underline{r}_j(t)}, \qquad (2.2)$$

where $\underline{k}$ is the scattering vector $\underline{k} = \underline{k}_i - \underline{k}_s$ and $E_0[\underline{r}_j(t)]$ is the electric field amplitude at the location of particle j. $E_0[\underline{r}]$ is determined by the incident beam profile and the profile function of the collecting optics. The area within the sample with $E_0[\underline{r}] \neq 0$ is called the scattering volume. It is the region that is both illuminated by the laser beam and seen by the detector. Because the time scale on which the particles move is slow with respect to $1/\omega$, light will be

scattered elastically, $|\underline{k}_i| = |\underline{k}_s|$ and

$$k \equiv |\underline{k}| = (4\pi n/\lambda)\sin(\theta/2), \tag{2.3}$$

where n is the refractive index of the fluid and λ is the wavelength of the light in vacuum.

Due to the Brownian motion of the illuminated particles the phase factor in the right-hand side of Eq. 2.2 will fluctuate. On a finite-size detector surface different points (corresponding to different scattering vectors $\underline{k}$) will see a different phase factor. This results in an effective reduction of the observed fluctuations due to averaging over a finite-size detector surface. The observability of Brownian motion therefore imposes a restriction on the maximum detector size. The criterion is that the phases in Eq. 2.2 should be essentially the same for different points on the detector surface. In other words, the angle δ subtended by the detector should satisfy

$$\delta << \lambda/d\,, \tag{2.4}$$

where d is the linear size of the scattering volume (see also Jakeman *et al.* 1970).

Photodetectors are sensitive to light intensities so that information about the phases of the electric field is partially lost. Without a special scattering setup all that remains is information about the phase differences of the individual contributions in the right-hand side of Eq. 2.2. As we will see, it may be that phase factors involving phase differences have statistical properties that are different from those involving the phases $i\underline{k}.\underline{r}_j(t)$ in Eq. 2.2.

Write the scattered electric field amplitude as

$$E(\underline{k},t) \equiv E(\underline{R},t) = \sum_{j=1}^{N} E_0[\underline{r}_j(t)]\, e^{i\underline{k}\cdot\underline{r}_j(t)}\,. \tag{2.5}$$

In the homodyne scattering setup the intensity of the scattered light is detected:

$$I(\underline{k},t) = \tfrac{1}{2}\epsilon_0 c\, E(\underline{k},t)\, E^*(\underline{k},t) \tag{2.6}$$

where E^* denotes the complex conjugate of E, c is the speed of light in vacuum

and ϵ_0 is the dielectric constant of the vacuum. Heterodyne scattering is a technique that does preserve full phase information. To that aim the scattered light is on the detector surface mixed with a reference beam that is split off the incident laser beam. The latter is called a local oscillator, its complex electric field amplitude is E_r and its polarization direction matches that of the scattered light. The detected intensity is due to both scattered and reference electric field amplitude:

$$I(\underline{k},t) \simeq \left| \sum_{j=1}^{N} E_0[\underline{r}_j(t)]\, e^{i\underline{k}\cdot\underline{r}_j(t)} \right|^2 + E_r\, E_r^* + 2\,\mathrm{Re}\left[E_r^* \sum_{j=1}^{N} E_0[\underline{r}_j(t)]\, e^{i\underline{k}\cdot\underline{r}_j(t)} \right] \qquad (2.7)$$

(the symbol $\simeq$ denotes proportionality). When the intensity of the local oscillator is much larger than the time-averaged intensity of the scattered light, the first term on the right-hand side of Eq. 2.7 can be neglected. In that case the time-dependent part of the intensity at the detector is a direct measure for the scattered field amplitude.

Quite often attempts to measure a pure homodyne signal are thwarted by reflections of the incident beam off glass surfaces e.g. of the scattering cell. These reflections give rise to a heterodyne contribution to the measured intensity. Explicit heterodyning using a much stronger local oscillator will resolve the ambiguous nature of such experiments.

The directly scattered light and the reference beam constitute an interferometer. When the mechanical stability of this interferometer is not perfect the pathlength difference between its two legs does not only fluctuate due to particle motion but also due to mechanical vibrations. These can ruin the heterodyne signal if they take place on a time scale comparable to the time scale associated with the fluctuation of scattered light due to Brownian motion.

2.3. Homodyne and heterodyne correlation functions

The statistical properties of the fluctuating scattered light intensity signal contain information on (relative) position fluctuations in a sample of Brownian particles. An instrument to characterize the statistical properties of the

scattered light is the time autocorrelation function. The homodyne correlation function is defined by

$$G_{hom}(\tau) \equiv \tfrac{1}{4}\epsilon_0{}^2c^2 <E(\underline{k},0)\, E^*(\underline{k},0)\, E(\underline{k},\tau)\, E^*(\underline{k},\tau)>, \qquad (2.8)$$

where $E(\underline{k},t)$ is the (complex) scattered field amplitude at the detector, the angular brackets denote an average over time.

The intensity correlation function in a heterodyne experiment for the case of a local oscillator with high intensity compared to the scattered intensity is given by (see Eq. 2.7)

$$G_{het}(\tau) = I_r{}^2 + I_r\, \epsilon_0 c\, \mathrm{Re}<E(\underline{k},0)\, E^*(\underline{k},\tau)> +$$

$$+ \tfrac{1}{2}\epsilon_0{}^2c^2\, \mathrm{Re}[E_r^*\, E_r^* <E(\underline{k},0)\, E(\underline{k},\tau)>], \qquad (2.9)$$

with $I_r \equiv \tfrac{1}{2}\epsilon_0 c\, E_r\, E_r^*$, the index r refers to the reference beam. When Eq. 2.5 is substituted into Eq. 2.9 a relation between particle position correlations and a light scattering correlation function is obtained:

$$G_{het}(\tau) = I_r{}^2 + I_r\, \epsilon_0 c\, \mathrm{Re}\Big[\sum_{i,j} <E_0[\underline{r}_i(\tau)]\, E_0^*[\underline{r}_j(0)]\, e^{i\underline{k}.[\underline{r}_i(\tau)-\underline{r}_j(0)]}>\Big] +$$

$$+ \tfrac{1}{2}\epsilon_0{}^2c^2\, \mathrm{Re}\Big[\, E_r^*\, E_r^* \sum_{i,j} <E_0[\underline{r}_i(\tau)]\, E_0[\underline{r}_j(0)]\, e^{i\underline{k}.[\underline{r}_i(\tau)+\underline{r}_j(0)]}>\Big]. \quad (2.10)$$

In many applications $E(\underline{k},t)$ can be assumed to have Gaussian statistics. For instance when the scattering volume can be divided in very many sections, each section giving a statistically independent contribution to the scattered electric field. This division within the scattering volume can be made when its linear dimensions are large compared to both the wavelength of the light and the correlation lengths within the sample. In case of a Gaussian scattered field amplitude the fourth-order correlation $G_{hom}(\tau)$ can be written in terms of second-order correlations, the so called Siegert relation (Dhont & De Kruif 1983):

$$<E(\underline{k},0)\ E^{*}(\underline{k},0)\ E(\underline{k},\tau)\ E^{*}(\underline{k},\tau)> = |<E(\underline{k},0)\ E^{*}(\underline{k},0)>|^2 +$$

$$+ |<E(\underline{k},0)\ E^{*}(\underline{k},\tau)>|^2 + |<E(\underline{k},0)\ E(\underline{k},\tau)>|^2. \quad (2.11)$$

Through this relation homodyne and heterodyne correlation functions are linked. In media with correlation lengths small compared to the scattering volume the correlation $<E(\underline{k},0)\ E(\underline{k},\tau)>$ will be zero except for very small scattering vectors. This may be elucidated by the following argument. $E(\underline{k},t)$ is the sum of very many statistical independent contributions, it can be looked upon as a random walk in the complex plane. When $|\underline{k}|^{-1}$ is small with respect to the linear size of the scattering volume the phases of the product $E(\underline{k},t)\ E(\underline{k},t+\tau)$ will be uniformly distributed over 2π radians. Therefore averaging over many particle configurations leaves $<E(\underline{k},0)\ E(\underline{k},\tau)>$ zero (the angular brackets represent time averaging, when ergodicity is assumed, time-averaged correlations equal ensemble-averaged correlations (Pusey & Van Megen 1989)). Dividing Eq. 2.11 by $|<E(\underline{k},0)\ E^{*}(\underline{k},0)>|^2 = <I(\underline{k},0)>^2$ then leads to a more familiar expression of the Siegert relation:

$$G^{(2)}(\tau) = 1 + |G^{(1)}(\tau)|^2, \quad (2.12)$$

with $G^{(2)}(\tau)$ and $G^{(1)}(\tau)$ the normalized intensity and field correlation functions respectively.

Correlation functions of stationary signals are connected to power spectra through the Wiener-Khintchin theorem (Wang & Uhlenbeck 1945). Spectral information of scattered light is therefore contained in the correlation function, correlation techniques can be looked upon as time-domain spectroscopy (Schätzel 1987).

2.4. Photon counting

The detector signal consists of noise due to the stochastic nature of both the particle motion and the light detection process. Measurement of correlation functions is a way to characterize the detector signal and therefore characterize

Brownian motion. Photon correlation very efficiently and very rapidly measures light intensity correlation functions under very low light level circumstances.

A photomultiplier serves as optical detector. Its output is a time series of pulses, each pulse represents a detected photon. This logical signal is processed by a digital correlator: the signal is sampled (i.e. the numbers of detected photons in consecutive time intervals with length τ_s are counted) and the photon correlation function is (real time) calculated:

$$G_N(j\tau_s) = \frac{1}{N-j} \sum_{i=j}^{N} n_i \, n_{i-j} \, , \qquad (2.13)$$

where n_i is the number of photons detected in time interval i and N is the total number of time intervals processed, typically $N >> j$. In general τ_s is chosen such that the light intensity at the detector surface changes slowly compared to τ_s. The stochastic process of photon detection is assumed to have two fundamental properties (Schätzel 1987). In the first place the expectation of n_i is assumed to be proportional to the average light intensity in the interval i (i.e. $<n_i> \simeq I_i$). In the second place one assumes statistical independence of n_i and n_j, $i \neq j$, for arbitrary but fixed values of the averaged intensity in the intervals i and j (i.e. $<n_i n_j | I_i, I_j> = <n_i | I_i> <n_j | I_j>$). These two properties guarantee a linear relationship between the normalized photon correlation function and the normalized intensity correlation function:

$$G(j\tau_s) \equiv \frac{<n_i \; n_{i-j}>}{<n_i>^2} \simeq \frac{<I(\underline{k}, 0) \; I(\underline{k}, j\tau_s)>}{<I(\underline{k},0)>^2} \; ; j \neq 0. \qquad (2.14)$$

2.5. Heterodyning with a single mode optical fiber

Homodyne experiments are easier to perform than heterodyne experiments. The main problem of heterodyne light scattering experiments is the mechanical stability of the setup. Severe distortion of correlation functions already occurs when the optical pathlength difference between the two interferometer legs

fluctuates with an amplitude that is a small fraction of the wavelength of the used light and with a timescale comparable to the time scale of interest. The measurement of homodyne correlation functions does not suffer from these problems. There are, however, two important reasons why in some cases heterodyne experiments are preferred.

The first reason is of practical nature and is already mentioned in section 2.2: resolving the ambiguous nature of homodyne experiments that suffer from heterodyne contributions due to unwanted reflections of direct light into the detector. In the thin cells that are used in colloidal crystal experiments (see chapter 5) this is an important effect because the scattering volume is in one direction bounded by two glass surfaces.

The second reason for heterodyning is of more fundamental nature. Only when the scattered light has Gaussian statistics do homodyne and heterodyne experiments bear equivalent information. Both types of correlations are then related by the Siegert relation. In some experiments, however, presence of Gaussian light is not obvious. In these cases heterodyne experiments are preferred because field correlation functions can be translated more easily in terms of particle position correlations than intensity correlation functions.

In our heterodyne experiments the reference beam was guided through a single-mode optical fiber (Fig. 2.2), constituing an interferometer with one flexible leg. The main reason for doing this is that a change of the optical configuration, for instance a change of the scattering angle, does not necessitate new alignment of the reference beam, it flexes with the optical fiber. In this heterodyne setup one can manipulate the detector as if one was doing homodyne light scattering. Because the interferometer is very asymmetric we had to pay a high price for this ease, namely the construction of an extremely stable setup and strict requirements for the pointing stability of the laser, all in order to avoid unwanted optical pathlength fluctuations. The stability of the setup was obtained by using stiff construction elements and mechanical isolation of the optical table from the laboratory floor. Experiments with the setup did not show unwanted vibrations in heterodyne correlation functions with frequencies higher than 15 Hz .

The optical fiber was single mode at the used wavelength (0.633 μm) and polarization preserving (Newport F–SPA, core diameter 4 μm). To launch part of the laser beam into the fiber we used a $\lambda/2$ plate to match the beam

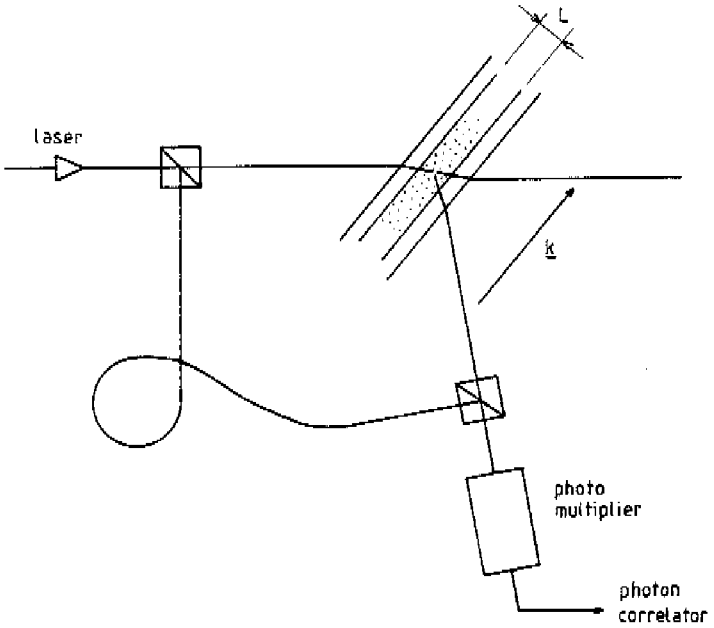

Fig. 2.2 An experimental setup in which heterodyning of the scattered light is performed by a single-mode optical fiber.

polarization and the fiber orientation, and a $f = 5$ cm lens to focus the beam at the fiber-end. A high incoupling efficiency was not necessary because not much light is needed for effectively heterodyning the scattered light. In fact the incoupling efficiency was used as a means of tuning the local oscillator intensity to the scattered light intensity. The beam that emerged from the fiber had a Gaussian profile, the radius of the waist at the fiber-end was approximately 2.5 μm (Marcuse 1982). Because this is only a few wavelengths, the beam strongly diverged. A single, small focal length lens ($f = 10$ mm) placed in front of the fiber-end provided an almost flat reference beam wavefront. By simply rotating the fiber-end the reference beam polarization direction can be chosen.

The apparatus in which the scattered light is mixed with the reference beam is shown in Fig. 2.3. Through careful manipulation of the position and orientation of a beam splitter cube, part of the reference beam is directed through a front pinhole towards a 0.1 mm diameter multimode optical fiber-end (Fig. 2.3). Dependent on scattered light intensity levels and pinhole diameters a 50 : 50 or an approximately 10 : 90 (90 % passes through) beam splitter cube was used. Scattered light enters the detector through the same front pinhole, part of it falls on the multimode fiber-end. The mixed optical signal is transported through the multimode fiber to a photomultiplier.

The heterodyne setup of Fig. 2.2 was tested in a standard dynamic light scattering experiment: the determination of the diffusion coefficient of non-interacting spherical particles. When a very dilute monodisperse sample of spheres is probed with dynamic light scattering spectroscopy, the field correlation function is an exponential with a decay rate that is dependent on the diffusion coefficient of the particles (D) and the length of the scattering vector (k) (see e.g. Schätzel 1987):

$$G^{(1)}(\tau) \simeq e^{-Dk^2\tau} . \qquad (2.15)$$

The Siegert relation (Eq. 2.12) shows that the time-dependent part of the homodyne correlation function is also an exponential. Its decay rate equals $2Dk^2$.

A thin-film cell, consisting of two flat quartz windows, separated by an O ring (cell thickness $L = 77$ μm ; for more details on the thin-film cell see chapter 5) contained a sample of $a = 0.099$ μm radius polystyrene spheres (The Dow Chemical Company; particle size from the manufacturer) in water of 20 °C. The ratio of cell thickness to particle size was so large that the influence of the walls on diffusion could be neglected (Hurd *et al.* 1980). The number concentration of the spheres was $n = 2.5 \times 10^{16}$ m^{-3}; this concentration is small enough to neglect direct and hydrodynamic particle interactions. We measured homodyne and heterodyne correlation functions with the scattering vector $\underline{k}$ parallel to the quartz windows at three values of the scattering angle θ. The measured correlation functions were described with the following formula:

$$G(j\tau_s) = c_1 e^{-\Gamma j \tau_s} + c_2 , \qquad (2.16)$$

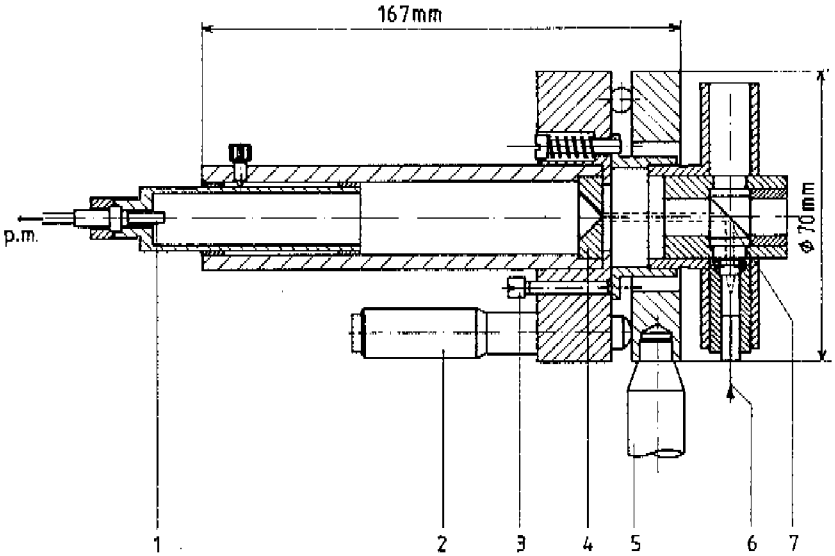

Fig. 2.3 *The heterodyne detector. The scattered light vector* $\underline{\mathbf{k}}_s$ *is defined by the first pinhole (4) and the multimode fiber end (1) that serves as a second pinhole. The beam splitter cube (7) in front of the first pinhole directs the reference beam emerging from the single-mode fiber (6) through the first pinhole towards the multimode fiber. The mixed optical signal is transported to a photomultiplier.*

The detector is mounted on the light scattering stage by means of a rod (5). The screws (3) allow small adjustment of the orientation of the reference beam. The micrometer screws (2) are used to direct the detector. Notice that once the reference beam is aligned the detector can be manipulated freely without losing the alignment.

where the parameters c_1, c_2 and Γ followed from a least-squares fit. The sample times τ_s were chosen such that the correlation functions extended over approximately $8\ \Gamma^{-1}$, all 10^3 correlator channels were used in the fitting procedure. The deviation of the points of the measured heterodyne correlation functions from the exponentials was less than 0.6 % of c_1 over the entire $8\ \Gamma^{-1}$ interval (0.006 c_1 was approximately two times the photon noise of the correlation function). Whereas homodyne correlation functions deviated about 1 % of their c_1 from single exponentials. Figure 2.4 shows the results in the form of Γ versus k^2. The expected linear relationship between Γ and k^2 is confirmed in our results. In this thin-film cell setup the heterodyne measurements are better than homodyne measurements. The homodyne measurements suffer from a systematic error: the decay rates are too low. This is

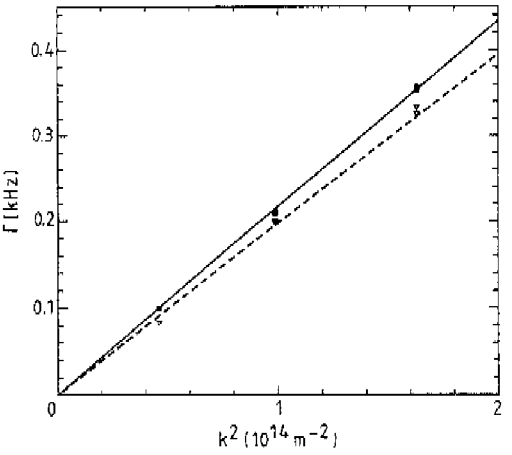

Fig. 2.4 Decay rate versus square scattering vector for homodyne (∇) and heterodyne (o) experiments. The decay rates of the homodyne experiments have been divided by two for comparison with the heterodyne experiments. The theoretical line for $a = 0.099$ μm radius spheres in water of 20 °C (solid line) covers the heterodyne experiments.

probably due to a heterodyne contribution to the intensity correlation function of the scattered light. With a least-squares fit of a homodyne correlation function to a linear combination of the corresponding heterodyne function and the square of the heterodyne function one can estimate the amount of static light in the homodyne experiment:

$$G_{hom}(j\tau_s) = c_0 + c_1\, G_{het}(j\tau_s) + c_2\, [G_{het}(j\tau_s)]^2\,;\;\; c_1/c_2 = 2\, I_r/\langle I_s \rangle\,,$$

where I_r is the static light intensity and $\langle I_s \rangle$ is the time averaged scattered light intensity. This procedure showed that of the order of 5 % of the light detected in the homodyne experiments was static, i.e. was not scattered by the particles.

Chapter 3 LIGHT SCATTERING OFF BROWNIAN PARTICLES IN SHEAR FLOW

3.1. Introduction

Dynamic light scattering is employed to probe the microscopic fluctuations of the positions of particles immersed in a fluid that undergoes shear. With a conventional experimental setup it is not possible to extract information on Brownian motion from this non-equilibrium system; the correlation functions are dominated by the deterministic motion of the particles (due to fluid flow), Brownian motion is obscured. The reason for this is that the time scales associated with fluid flow are widely separated from those associated with Brownian motion. Effects of deterministic particle motion are interesting for laser-Doppler velocimetry, because they can be exploited to procure the velocity gradient in a point (Fuller *et al.* 1980; Keveloh & Staude 1983).

A cross-correlation technique can be used to introduce a time shift such that the Brownian motion time scale comes within the reach of the scattered light correlation function. In this chapter a cross-correlation experiment on shear-influenced Brownian motion of non-interacting particles is described.

3.2. Brownian motion in shear flow

Colloidal particles in a host fluid exhibit Brownian motion. Collisions with thermally excited fluid molecules provide the stochastic driving force of this motion. The particle motion is damped by the Stokes friction with the solvent fluid. The microscopic equation of motion, the Langevin equation, for a Brownian particle reads:

$$\frac{d^2\underline{r}}{dt^2} + \beta \frac{d\underline{r}}{dt} = \frac{1}{m}\underline{X}(t), \tag{3.1}$$

where $\underline{r}(t)$ is its time-dependent position. The first and second moment of the random force $\underline{X}(t)$ are

$<\underline{e}_i.\underline{X}(t)> = 0$ and $<\underline{e}_i.\underline{X}(t)\ \underline{e}_j.\underline{X}(t+\tau)> = (2k_B T\beta m)\ \delta_{ij}\ \delta(\tau)$ $(i, j = x, y, z)$,

where k_B is the Boltzmann constant and T is the absolute temperature. The friction coefficient β for an isolated spherical particle with radius a, and mass m in a fluid with dynamic viscosity η is $\beta=6\pi\eta a/m$, it is also the inverse of the characteristic time of the velocity autocorrelation function. For large times, such that $t>>\beta^{-1}$, an equation for the probability density $P(\underline{r},t)$ of the particle position may be derived (Wang & Uhlenbeck 1945):

$$\frac{\partial P}{\partial t} = D\,\nabla^2 P. \tag{3.2}$$

The Stokes-Einstein result:

$$<|\Delta_{\underline{r}}|^2> = 6Dt,\ D=k_B T/6\pi\eta a \tag{3.3}$$

expresses that the mean-square displacement of a free Brownian particle is proportional to time. The diffusion coefficient D is determined by the kinetic energy of the fluid molecules, $k_B T$, and the Stokes resistance of a sphere, $6\pi\eta a$.

When a Brownian particle is subjected to simple shear ($v_x = v_0 + \gamma y$, $v_y = 0$, $v_z = 0$), the Langevin equation becomes:

$$\frac{d^2x}{dt^2} + \beta\frac{dx}{dt} = \beta(\gamma y + v_0) + \frac{1}{m}X_x(t), \tag{3.4a}$$

$$\frac{d^2y}{dt^2} + \beta\frac{dy}{dt} = \frac{1}{m}X_y(t), \tag{3.4b}$$

$$\frac{d^2z}{dt^2} + \beta\frac{dz}{dt} = \frac{1}{m}X_z(t), \tag{3.4c}$$

where γ is the shear rate. The counterpart of Eq. 3.2 in case of fluid flow is the convective-diffusion equation:

$$\frac{\partial P}{\partial t} + \underline{v}.\nabla P = D\,\nabla^2 P. \tag{3.5}$$

The equation has been solved for simple shear flow by Foister & Van de Ven (1980) with initial condition $P(\underline{r},0) = \delta(\underline{r})$ and boundary condition $P(\underline{r},t) = 0$ for $|\underline{r}| \to \infty$. The result is

$$P(\underline{r},t) = (4\pi Dt)^{-3/2} \left[\frac{3}{(\gamma t)^2+12} \right]^{1/2} \exp\left[-\frac{3(x-v_0 t-y\gamma t/2)^2}{Dt[(\gamma t)^2+12]} - \frac{y^2+z^2}{4Dt} \right] . \quad (3.6)$$

When $v_0 = 0$, it follows

$$\langle x^2 \rangle = 2Dt[1 + (\gamma t)^2/3]; \quad \langle y^2 \rangle = 2Dt; \quad \langle z^2 \rangle = 2Dt; \quad \langle xy \rangle = D\gamma t^2.$$

An at first sight surprising result is that the mean-square displacement of a particle is proportional to t^3 (see also San Miguel & Sancho 1979). Strictly speaking there is then no longer diffusive behaviour. Furthermore, the spreading of the particles becomes anisotropic; displacements in the x-direction are enhanced by the flow. An intuitive understanding for this behaviour may be reached as follows. In the y-direction there is ordinary diffusion with rms displacement $\Delta y \simeq t^{1/2}$. This gives rise to a displacement in the x-direction of $(\Delta y \gamma)t \simeq t^{3/2}$, resulting in a mean-square displacement in x-direction proportional to t^3.

3.3. Dynamic light scattering in shear flow

The first study of light scattering in shear flow was reported by Fuller *et al.* (1980). Their main interest was in point measurements of velocity gradients, not in Brownian motion. As will be demonstrated here, in a conventional experimental setup fluctuations due to Brownian motion are obscured by a modulation of the correlation function due to particles traversing the scattering volume.

We extended the conventional experiment with an extra scattering vector and study the cross correlation between light scattered in both directions. The autocorrelation experiment is the special case in which both scattering vectors are equal. The scattered field amplitudes are coherent sums of the contributions

of N particles:

$$E(\underline{k}_m,t) = \sum_{j=1}^{N} E_m[\underline{r}_j(t)]\, e^{i\underline{k}_m\cdot\underline{r}_j(t)}\ ;\ m = 1,\ 2; \tag{3.7}$$

where $\underline{k}_1$ and $\underline{k}_2$ are the scattering vectors and $E_1[\underline{r}]$ and $E_2[\underline{r}]$ are the field amplitude profile functions belonging to each of the scattering vectors. They are determined by the incident beam and the collecting optics profile functions. The electric field cross correlation $g_1(\underline{k}_1,\underline{k}_2,\tau) \equiv \langle E^*(\underline{k}_1,0)\, E(\underline{k}_2,\tau)\rangle$ is given by

$$g_1(\underline{k}_1,\underline{k}_2,\tau) = \sum_i \sum_j \langle E_1^*[\underline{r}_i(0)]\, E_2[\underline{r}_j(\tau)]\, e^{-i[\underline{k}_1\cdot\underline{r}_i(0)-\underline{k}_2\cdot\underline{r}_j(\tau)]}\rangle\ . \tag{3.8}$$

In the case of non-interacting particles only the terms with $i = j$ contribute to the correlation. The ensemble average in Eq. 3.8 is factorized in a part involving the phases and a part involving the amplitudes (which is permitted if the linear size of the scattering volume is large with respect to the wavelength of the used light):

$$g_1(\underline{k}_1,\underline{k}_2,\tau) = \sum_j E_1^*[\underline{r}_j]\, E_2[\underline{r}_j]\, \langle e^{-i[\underline{k}_1\cdot\underline{r}_j(0)-\underline{k}_2\cdot\underline{r}_j(\tau)]}\rangle. \tag{3.9}$$

The particle position may be written as the sum of a deterministic component due to convection and a stochastic part, $\tilde{\underline{r}}(t)$, due to Brownian motion:

$$\underline{r}_j(\tau) - \underline{r}_j(0) = \tau\,(v_0 + y_j(0)\gamma)\,\underline{e}_x + \tilde{\underline{r}}_j(\tau) - \tilde{\underline{r}}_j(0). \tag{3.10}$$

Accordingly the electric field cross correlation can be written as

$$g_1(\underline{k}_1,\underline{k}_2,\tau) = \sum_j E_1^*[\underline{r}_j]\, E_2[\underline{r}_j]\, e^{ik_{2x}(v_0+y_j\gamma)\tau}\, e^{-i\Delta\underline{k}\cdot\underline{r}_j}\, \langle e^{i\underline{k}_2\cdot[\tilde{\underline{r}}_j(\tau)-\tilde{\underline{r}}_j(0)]}\rangle, \tag{3.11}$$

with $\Delta\underline{k} = \underline{k}_1 - \underline{k}_2$. The function $B(\underline{k},\tau) \equiv \langle e^{i\underline{k}\cdot[\tilde{\underline{r}}_j(\tau)-\tilde{\underline{r}}_j(0)]}\rangle$ is independent of the initial position of particle j. It is the spatial Fourier transform of $P(\underline{r},\tau)$ with $v_0 = 0$ (Fuller *et al.* 1980). Therefore (see Eq. 3.6)

$$B(\underline{k},\tau) = e^{-D[k_x^2(1+(\gamma\tau)^2/3)-\gamma\tau k_x k_y+k_y^2+k_z^2]\tau} \qquad (3.12)$$

In the absense of shear the well known exponential correlation $e^{-Dk^2\tau}$ is obtained. In order to observe the influence of shear in the correlation function $B(\underline{k},\tau)$ the experiment has to be arranged in such a way that $\gamma\tau$ is at least of the order of one. Therefore the most important time scale for Brownian motion in shear flow is $\tau_b \equiv \gamma^{-1}$.

Fuller *et al.* (1980) measured autocorrelation functions, i.e. correlations with $\underline{k}_1 = \underline{k}_2 \equiv \underline{k}_0$ and $E_1(\underline{r}) = E_2(\underline{r}) \equiv E_0(\underline{r})$. When the sum in Eq. 3.11 is approximated with an integral over the scattering volume V (that is defined by the cross section of the laser beam and the acceptance cone of the light collecting optics) the field autocorrelation function is given by

$$g_1(\underline{k}_0,\underline{k}_0,\tau) = e^{ik_{0x}v_0\tau}\, B(\underline{k}_0,\tau)\, \frac{2}{\epsilon_0 c} \int_V d^3r\, I(\underline{r})\, e^{ik_{0x}y\gamma\tau}, \qquad (3.13)$$

with $I(\underline{r}) = \frac{1}{2}\epsilon_0 c\, E_0(\underline{r})\, E_0^*(\underline{r})$. Equation 3.13 contains three time-dependent factors. The first factor, $e^{ik_{0x}v_0\tau}$, vanishes when an intensity correlation is measured and this factor is multiplied by its complex conjugate (application of the Siegert relation). The third factor is a spatial Fourier transform of the intensity distribution $I(\underline{r})$ over the scattering volume. It is completely determined by the deterministic motion of the particles in the scattering volume. This factor will decay on a time scale $\tau_c=(k_{0x}\gamma d)^{-1}$, where d is the size of the scattering volume. The second factor is due to shear-induced Brownian motion: $B(\underline{k}_0,\tau)$. Its most important time scale is τ_b. This is much larger than τ_c: their ratio is of the order of d/λ, that is the macroscopic size of the scattering volume over the wavelength of light. Due to the finite signal to noise ratio in the experiment only the phenomenon associated with the shortest time scale will be observable. Thus, the function $B(\underline{k}_0,\tau)$ will be obscured by the integral in Eq. 3.13.

Summarizing, the naive autocorrelation experiment produces a correlation function that consists of a peak at $\tau = 0$ whose width is inversely proportional to the size of the scattering volume (we speak of a peak in relation to the

Brownian motion time τ_b). Cross correlation can shift the peak to positive times τ_0. Inspection of Eq. 3.11 shows that the time shift is performed when $\Delta\underline{k}$ is in the y-direction, i.e. perpendicular to the flow. The cross-correlation function then reads:

$$g_1(\underline{k}_1,\underline{k}_2,\tau) = B(\underline{k}_1,\tau)\, e^{ik_x v_0 \tau} \int_V d^3r\, E_1^*(\underline{r})\, E_2(\underline{r})\, e^{iy(k_x\gamma\tau-\Delta k)}\,; \qquad (3.14)$$

with $\Delta k = \Delta\underline{k}.\underline{e}_y$. Because $\Delta\underline{k}$ is in the y-direction $k_{1x} = k_{2x} \equiv k_x$. The Fourier transform of the product of profile functions $E_1^*(\underline{r})\, E_2(\underline{r})$ is shifted towards $\tau_0 = \Delta k/k_x\gamma$. When $\Delta k/k_x$ is of the order of one the Brownian motion time scale τ_b comes within sight.

Cross correlation can be done directly by feeding the correlator with two detector signals, each signal representing light scattered in a certain direction (Keveloh & Staude 1983). The time shift due to the shear flow provides another possibility for cross correlation: autocorrelation of a signal that represents the coherent sum of scattered light characterized by two scattering vectors. In general this leads to a sum of auto- and cross-correlation functions. In this specific situation separation of the several terms is simple because they are shifted in time with respect to one another. Write the electric field amplitude at the detector as

$$E(\underline{k}_1,\underline{k}_2,t) = E(\underline{k}_1,t) + E(\underline{k}_2,t)\,, \qquad (3.15)$$

the electric field autocorrelation function then reads explicitely

$$\begin{aligned} <E^*(\underline{k}_1,\underline{k}_2,0)\, E(\underline{k}_1,\underline{k}_2,\tau)> &= <E^*(\underline{k}_1,0)\, E(\underline{k}_1,\tau)> + <E^*(\underline{k}_2,0)\, E(\underline{k}_2,\tau)> + \\ &+ <E^*(\underline{k}_1,0)\, E(\underline{k}_2,\tau)> + <E^*(\underline{k}_2,0)\, E(\underline{k}_1,\tau)>\,. \end{aligned} \qquad (3.16)$$

The first two terms on the right-hand side are autocorrelations, the third term is the cross correlation $g_1(\underline{k}_1,\underline{k}_2,\tau)$ which is shifted towards $\tau_0 = \Delta k/k_x\gamma$, the fourth term ($g_1(\underline{k}_2,\underline{k}_1,\tau)$) is shifted towards $\tau_0 = -\Delta k/k_x\gamma$. In our experiments we used two incident beams (originating from the same laser) and one detector to make a geometry with two scattering vectors (see Fig. 3.1).

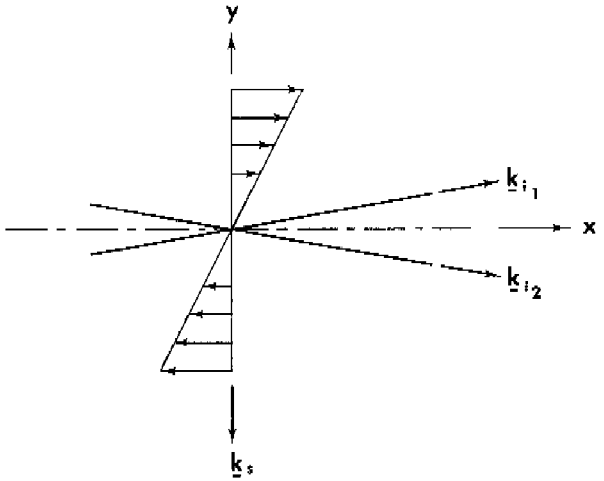

Fig. 3.1 *Scattering geometry in shear flow with two beams* $\underline{k}_{i1}$, $\underline{k}_{i2}$. *Scattered light is detected in the direction of* $\underline{k}_s$.

Provided that the physics of the experiment allows application of the Siegert relation the intensity correlation becomes

$$<I(0)I(\tau)> = <I(0)>^2 + \tfrac{1}{4}\epsilon_0^2 c^2 \left| <E^*(\underline{k}_1,0)\, E(\underline{k}_1,\tau)> + <E^*(\underline{k}_2,0)\, E(\underline{k}_2,\tau)> \right|^2 +$$

$$+ \tfrac{1}{4}\epsilon_0^2 c^2 \left| <E^*(\underline{k}_1,0)\, E(\underline{k}_2,\tau)> \right|^2 + \tfrac{1}{4}\epsilon_0^2 c^2 \left| <E^*(\underline{k}_2,0)\, E(\underline{k}_1,\tau)> \right|^2. \quad (3.17)$$

The cross products between auto- and cross correlations and between the two cross correlations are approximately zero because of the shifts towards $\tau_0 = \pm\, \Delta k/k_x\gamma$ of the latter. The phase factors $e^{ik_x v_0 \tau}$ vanish in the intensity correlation. The resulting intensity correlation function for $\tau \geq 0$ will therefore have two peaks, the autocorrelation peak is located at $\tau = 0$, the cross-

correlation peak is located at $\tau_0 = |\Delta k/k_x\gamma|$. The height of this secondary peak is proportional to $|B(\underline{k},\tau_0)|^2$. The position of the secondary peak can be varied by varying Δk, i.e. by varying the mutual beam angle, or by changing the shear rate γ. The time dependence of $|B(\underline{k},\tau)|^2$ can therefore be obtained by measurement of the secondary peak height as a function of its position.

Only when light that is scattered from the region where the two beams cross is detected, a cross-correlation peak is obtained; it is required that three lines (two beams and the line defined by the detection optics) pass through one point. In case of misalignment the cross correlation in Eq. 3.17 becomes zero and the squared absolute value of the sum of autocorrelations becomes oscillatory. The latter is due to the $e^{ik_x v_0 \tau}$–factors: in case of misalignment v_0 differs for both autocorrelations. This oscillatory behaviour of the intensity correlation function is used as a tool for alignment. The detector is adjusted such that the correlation function ceases to show oscillations.

3.4. Experimental setup

The scattering geometry of Fig. 3.1 was realised in the experimental setup shown in Fig. 3.2. The flow was generated in a Couette device with counter-rotating cylinders. The radial position of the center of the scattering volume was chosen such that $v_0 = 0$, this ensured that the time scales of phase fluctuations are much smaller than amplitude fluctuation time scales (see the approximation in Eq. 3.9). In order to define accurately the position of the crossing region of the beams, their mutual angle and the scattering angles a glass cylinder is placed concentric with the scattering volume. All of the apparatus within its perimeter, including fluid and glass cylinders of the Couette apparatus, had a uniform refractive index at the used wavelength of 0.5145 μm. The index-matching fluid in which the particles were suspended was a mixture of tetraethylene glycol and glycerol. We used polystyrene spheres with 0.19 μm diameter and volume fraction 2.5 x 10^{-5}. The laser beam emerged from an Argon-ion laser and was subsequently divided into three parts in a modified Köster prism. Two beams entered the Couette device, the third beam was used to check and control the position of the crossing region in the fluid. This setup

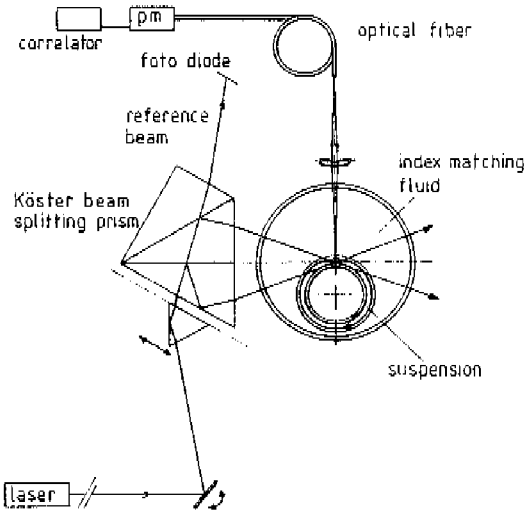

Fig. 3.2 Experimental setup. Two laser beams cross between the counter-rotating cylinders of a Couette device, the reference beam is used to monitor the position of the scattering volume.

enabled to alter the beam crossing angle while keeping the crossing region fixed in space by rotating a mirror and translating a small prism such that the reference beam remained at a fixed position. A quadrant diode monitored the reference beam position to an accuracy of approximately 5 μm. The symmetric way in which the beam is splitted ensured that the phase relation between the two beams that enter the Couette device is insensitive for mechanical vibrations or pointing fluctuations of the laser beam. However, beam stability is required for a different reason. An unstable beam gives rise to position fluctuations of the beam crossing region relative to the detector. This leads to fluctuations of the profile function $E_1^*(\underline{r})\ E_2(\underline{r})$ (see Eq. 3.14) which have a direct influence on the secondary peak height. Scattered light passed through a pinhole-lens combination and was transported to the photomultiplier using a multimode

optical fiber. The size of the resulting scattering volume was 30×100×100 μm. The logical photon signal is fed into a digital correlator. The measured photon correlation function is proportional to the intensity correlation function.

3.5. Results and conclusions

Figure 3.3 shows an example of a measured double-peaked photon correlation function. The two relevant parameters, the position and the height of the secondary peak are found by fitting a Gaussian function. Figure 3.4a shows the secondary peak position as a function of the inverse rotating velocity ω^{-1} ($\simeq \gamma^{-1}$) of the counter-rotating cylinders of the Couette device. The two incident beams cross under an angle of 16°. The predicted relation between τ_0 and γ is also drawn in the figure, and demonstrates that the present setup allows point measurements of shear rates. Figure 3.4b shows the log of the measured

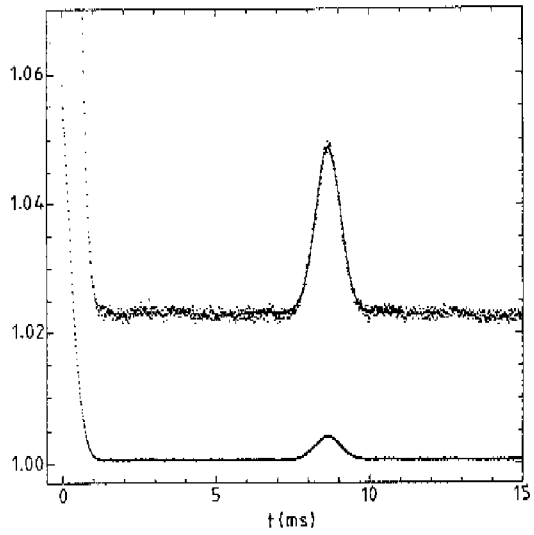

Fig. 3.3 Measured normalized photon correlation function; the upper part is an enlargement of the lower part. The full line represents a Gaussian function that has been fitted to the experimental results.

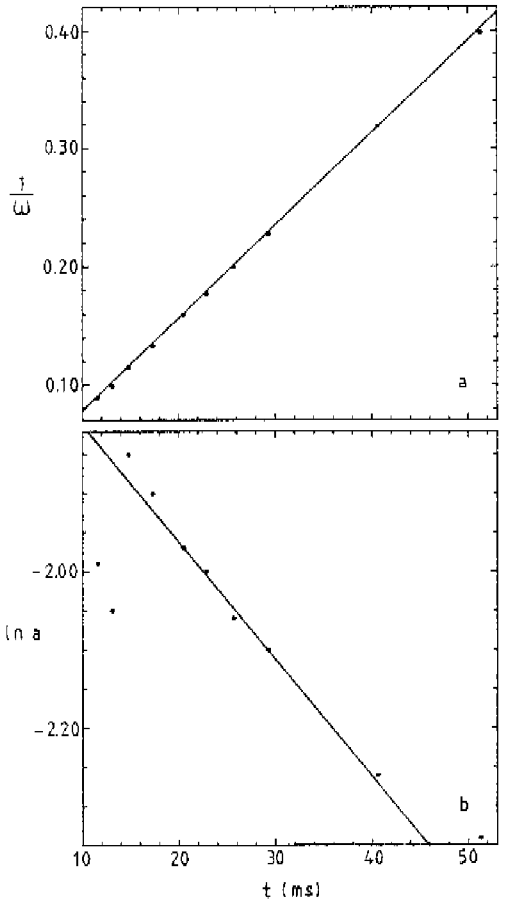

Fig. 3.4 (a) Dots: position of the secondary peak as a function of inverse angular velocity. Full line: expected behaviour for a mutual beam angle of 16°. *(b) Dots: log of height of secondary peak as a function of delay time. Full line: prediction based on Eq. 3.12 (see text), the line has been shifted vertically.*

secondary peak height as a function of the peak delay time τ_0. The delay time was varied by varying the shear rate while keeping the beam crossing angle constant, as a consequence, the product $\gamma\tau_0$ ($= \Delta k/k_x$) is also constant. At a beam crossing angle of 16° and a scattering wave vector $\underline{k}_s$ which is perpendicular to the bisector of the incident beams, $\gamma\tau_0 = 0.28$. When $\gamma\tau_0$ is constant, $B(\underline{k},\tau_0)$, which embodies the Brownian motion, is a negative exponential function of time (Eq. 3.12). This is in agreement with the observed

behaviour, however, deviations are evident at short times (high shear rates), and long times (low shear rates).

There have been earlier reports of an attempt to meausure Brownian motion in a sheared fluid (Ackerson & Clark 1981). The present experiment is, to our knowledge, the first to demonstrate the feasibility of a two-beam setup. Apart from the fundamental interest in obtaining information about non-equilibrium fluids, there are a few important practical ramifications. First, we have again demonstrated the possibility of point measurements of the shear rate (Fuller *et al.* 1980; Keveloh & Staude 1983). Second, our method could be used to obtain information about the sizes of particles in a sheared fluid; this would be of relevance in those situations where the particle size may alter due to shear stress. There are also quite a few experimental intricacies. The most important experimental circumstance is the definition of the scattering volume, which requires an extremely stable setup.

4.1. Introduction

A colloidal crystal is a regular array of identical colloidal particles immersed in a fluid. In the dilute crystals studied in this thesis electrostatic repulsion is responsible for the long-range crystalline order. Monodisperse polystyrene colloids can be produced by means of emulsion polymerization. The entangled macromolecular chains that constitute the spherical particles have salt end groups (e.g. $-SO_4K$) that dissociate in water. This provides the particles with a net negative electrostatic charge. By chemically removing extraneous ions from the water sufficiently long-range electrostatic interactions between the particles can be obtained for crystallization to occur. Colloidal crystals have been observed directly under the microscope (Kose *et al.* 1973; Van Winkle & Murray 1986). With these studies a clear view on the crystalline structure and on dislocations and defects is acquired. An extensive review on colloidal crystals has been presented by Pieranski (1983).

Colloidal crystals are very well suited for the study of Brownian motion in the presence of particle interaction. Especially hydrodynamic interaction is much more important in ordered colloids than in random swarms of particles. Hydrodynamic interaction enters at order $\phi^{1/3}$ instead of order ϕ in a random medium (Hasimoto 1959; Saffman 1973), where ϕ is the volume fraction occupied by the particles. Explicit expressions for the frequency and damping of crystal waves initiated by Brownian motion can be derived (Hurd *et al.* 1982; Felderhof & Jones 1986). The damping of crystal waves depends on their wavelength and (very important) on their polarization direction. Longitudinal waves are strongly damped because they are always accompanied by backflow; i.e. in these modes the particles move relative to the fluid. Long-wavelength transverse waves are characterized by coherent motion of the particles and the fluid. Their damping is determined by the relaxation of shear modes in the fluid (Joanny 1979). Information on the elasticity of single colloidal crystals is contained in the frequency of the Brownian (i.e. thermally) excited modes. Mechanical tests on the elasticity of colloidal crystals (see e.g. Lindsay & Chaikin 1982) involve polycrystalline samples.

This chapter is a review of the theoretical results on colloidal crystal dynamics

obtained by Hurd *et al.* (1982 and 1985) and by Felderhof & Jones (1986). Section 4.4 is devoted to the effects of the finite counter ionic diffusivity on colloidal crystal dynamics; a topic introduced by Felderhof & Jones (1987) in order to explain the discrepancy between the experimental findings of Hurd *et al.* and their hydrodynamic theory.

4.2. Crystal dynamics

In this section a theory on colloidal crystals that includes linear electrostatic and hydrodynamic interactions is presented. It is based on the work by Hurd *et al.* (1982 and 1985) and by Felderhof & Jones (1986).

Consider a set of N charged identical spherical particles (radius a, charge $-Ze$) that are immersed in a fluid. The particles, driven by a random force, wander about lattice sites $\underline{R}_j$, j = 1...N. The dynamics of the system is described by the equations of motion of the particles and the equations for fluid flow, both are coupled through hydrodynamic friction. In case of incompressible and low-Reynolds-number flow we have linear flow equations:

$$\rho \frac{\partial \underline{v}}{\partial t} = \eta \nabla^2 \underline{v} - \nabla p + \underline{F}(\underline{r},t) , \tag{4.1}$$

$$\nabla . \underline{v} = 0 , \tag{4.2}$$

where $\underline{v}$ is the fluid velocity, ρ its density and η its dynamic viscosity. The particles exert a force density $\underline{F}(\underline{r},t)$ on the fluid. We assume that $\underline{F}(\underline{r},t)$ is due to a set of point forces located at the lattice sites $\underline{R}_j$:

$$\underline{F}(\underline{r},t) = \sum_{j=1}^{N} \underline{f}_j(t)\, \delta(\underline{r} - \underline{R}_j) . \tag{4.3}$$

The dynamics of the particles is described by a stochastic (or Langevin) equation

$$m \frac{d\underline{u}_j}{dt} = \underline{F}_j - \underline{f}_j + \underline{X}_j \,, \tag{4.4}$$

where $\underline{u}_j$ is the particle velocity and m is the mass of the particle. Of the three forces in the right-hand side of Eq. 4.4, $\underline{X}_j$ is the stochastic force that induces Brownian motion. The reaction force that is exerted by the fluid on the particle is $-\underline{f}_j$. The relatively short-range direct electrostatic interaction between the particles is $\underline{F}_j$. It is induced by Coulomb forces that are screened by counter ions in the fluid. It is the main goal of this section to derive expressions for $\underline{F}_j$ and $\underline{f}_j$, the latter containing the essential hydrodynamics.

Concerning the electrostatics we assume central pair interactions. Every particle carries with it a screened Coulomb potential $-\psi(|\underline{r} - \underline{R}_j|)$ (with $\psi > 0$). The spherical symmetry of ψ will be a good approximation in case of dilute crystals. In the harmonic approximation, which is valid when the particle diplacements are small compared to the characteristic length scale of ψ, the forces are proportional to the displacements $\underline{s}_j \equiv \underline{r}_j - \underline{R}_j$:

$$\underline{F}_j = -\sum_{\substack{k=1 \\ k \neq j}}^{N} \mathbf{D}(\underline{R}_j - \underline{R}_k).(\underline{s}_j - \underline{s}_k) \,, \tag{4.5}$$

with

$$\mathbf{D}(\underline{r}) = Ze\,\nabla\nabla\,\psi(r) = Ze\Big[\mathbf{I}\psi'(r)/r + \hat{\mathbf{r}}\hat{\mathbf{r}}[\psi''(r) - \psi'(r)/r]\Big] \,, \tag{4.6}$$

where $\hat{\mathbf{r}}$ equals $\underline{r}/r$ and $\mathbf{I}$ is the unit tensor.

Assuming harmonic time dependence, $\underline{v} = \underline{v}_\omega\, e^{-i\omega t}$, and similarly for $\underline{s}$, $\underline{f}$ and $\underline{X}$, the equations of motion for the fluid and particles become

$$-i\omega\rho\underline{v} = \eta\nabla^2\underline{v} - \nabla p + \sum_j \underline{f}_j\, \delta(\underline{r} - \underline{R}_j) \,, \tag{4.7}$$

$$\nabla.\underline{v} = 0 \,, \tag{4.8}$$

$$-\omega^2 m\underline{s}_j = -\sum_{\substack{k \\ k \neq j}} \mathbf{D}(\underline{R}_j - \underline{R}_k).(\underline{s}_j - \underline{s}_k) - \underline{f}_j + \underline{X}_j \,, \tag{4.9}$$

where we have dropped the subscript ω.

From Eqs. 4.7 and 4.8 a linear relationship follows between the flow field at $\underline{r}$ and the point forces at the lattice sites that induce the flow:

$$\underline{v}(\underline{r},\omega) = \sum_{k=1}^{N} \mathbf{T}(\underline{r} - \underline{R}_k,\omega).\underline{f}_k(\omega) \ . \tag{4.10}$$

In the case of zero frequency $\mathbf{T}$ is the well-known Oseen tensor (see e.g. Happel & Brenner 1973). The unknown forces $\underline{f}_j$ can be eliminated from the Eqs. 4.7 and 4.9 through prescription of the boundary condition of the flow field on the sphere surface. Following Hasimoto (1959) and Hurd *et al.* (1985) the particle velocity is required to be equal to the average of the fluid velocity over its surface:

$$\sum_{k=1}^{N} <\mathbf{T}(\underline{r} - \underline{R}_k,\omega)>^{R}_{j}.\underline{f}_k = -\,i\omega\underline{s}_j \ , \tag{4.11}$$

where $< \ >^{R}_{j}$ denotes a surface average over a sphere that is centered at $\underline{R}_j$. The boundary condition, Eq. 4.11, is equivalent to the Faxén theorem to first order in the sphere radius a (Mazur & Bedeaux 1974). Equations 4.9 and 4.11 embody the essential physics of colloidal crystals. They are in the form of 3N–dimensional matrix equations. As is very well known from elementary solid state physics (see e.g. Kittel 1971), these equations can be turned into ordinary three-dimensional matrix equations by an expansion in normal modes:

$$\underline{X}_j = \sum_{q} \underline{X}_q \, e^{i\underline{q}.\underline{R}_j}, \ \underline{f}_j = \sum_{q} \underline{f}_q \, e^{i\underline{q}.\underline{R}_j} \ \text{and} \ \underline{s}_j = \sum_{q} \underline{a}_q \, e^{i\underline{q}.\underline{R}_j} \ ,$$

where the summation over $\underline{q}$ remains within the first Brillouin zone (FBZ) because waves within the crystal with wavelengths shorter than nearest-neighbour distances are of no physical significance. Equations 4.9 and 4.11 then reduce to

$$\underline{f}_q - \omega^2 m\underline{a}_q + \mathbf{D}(\underline{q}).\underline{a}_q = \underline{X}_q, \tag{4.12}$$

$$\mathbf{T}(\underline{q},\omega).\underline{f}_q = -\,i\omega\underline{a}_q \ , \tag{4.13}$$

which is a set of matrix equations for each possible $\underline{q}$ (which in principle takes on discrete values due to the finite size of the crystal). The matrices $\mathbf{D}(\underline{q})$ and $\mathbf{T}(\underline{q},\omega)$ are the following lattice sums:

$$\mathbf{D}(\underline{q}) = \sum_{\substack{k=1 \\ k\neq j}}^{N} \mathbf{D}(\underline{R}_j - \underline{R}_k)\left[1 - e^{i\underline{q}.(\underline{R}_k - \underline{R}_j)}\right], \tag{4.14}$$

$$\mathbf{T}(\underline{q},\omega) = \sum_{k=1}^{N} <\mathbf{T}(\underline{R}_j + \underline{d} - \underline{R}_k,\omega)>^0 e^{i\underline{q}.(\underline{R}_k - \underline{R}_j)} \tag{4.15}$$

($\underline{R}_j + \underline{d}$ is on the j-th sphere surface). These sums are independent of j due to lattice periodicity, we can take $\underline{R}_j = 0$. Elimination of $\underline{f}_q$ from Eqs. 4.12 and 4.13 leads to

$$-\omega^2 m\underline{a}_q + \mathbf{D}(\underline{q}).\underline{a}_q - i\omega\, \mathbf{T}^{-1}(\underline{q},\omega).\underline{a}_q = \underline{X}_q. \tag{4.16}$$

Equation 4.16 shows that each crystal wave (or phonon) with wavevector $\underline{q}$, can be viewed as a damped harmonic oscillator driven by a random force $\underline{X}_q$. By a rotation of coordinates Eq. 4.16 can be decoupled into three modes (one purely longitudinal and two transverse if $\underline{q}$ is chosen in crystal symmetry directions, Hurd *et al.* 1985). In general the potential tensor $\mathbf{D}(\underline{r})$ is of short range, therefore the lattice sum in Eq. 4.14 can be restricted to nearest and next-nearest neighbours. In a BCC lattice with lattice parameter R_0, the nearest-neighbour (nn) distance is $r_0 = \sqrt{3}\, R_0/2$ and the next-nearest-neighbour (nnn) distance equals the lattice parameter. After introducing the following elastic constants

$$\begin{aligned} A_1 = Ze\,\psi'(r_0)/r_0\,, \quad B_1 = Ze[\psi''(r_0) - \psi'(r_0)/r_0], \\ A_2 = Ze\,\psi'(R_0)/R_0 \ \text{ and } \ B_2 = Ze[\psi''(R_0) - \psi'(R_0)/R_0] \end{aligned} \tag{4.17}$$

the tensor of potential interactions becomes

$$\mathbf{D}(\underline{q}) \approx A_1 \mathbf{I} \sum_{nn} (1 - e^{i\underline{q}.\underline{R}_{nn}}) + B_1 \sum_{nn} \hat{R}_{nn}\hat{R}_{nn}(1 - e^{i\underline{q}.\underline{R}_{nn}}) +$$

$$+ A_2 \mathbf{I} \sum_{nnn} (1 - e^{i\underline{q}.\underline{R}_{nnn}}) + B_2 \sum_{nnn} \hat{R}_{nnn}\hat{R}_{nnn}(1 - e^{i\underline{q}.\underline{R}_{nnn}}) , \quad (4.18)$$

where $\underline{R}_{nn}$ and $\underline{R}_{nnn}$ are the positions of the nearest and next-nearest neigbours respectively. The evaluation of the lattice sums in Eq. 4.18 in a BCC lattice is a standard exercise in crystal dynamics (see e.g. Felderhof & Jones 1986).

Long-ranged hydrodynamic interactions are embodied in the friction tensor $\mathbf{T}(\underline{r},\omega)$ that decays as $1/r$. The many body character of hydrodynamic interactions in colloidal crystals is reflected in the fact that the lattice sum in Eq. 4.15 needs to be carried over the entire lattice. The lattice sum $\mathbf{T}(\underline{q},\omega)$ can be written as a Fourier transform:

$$\mathbf{T}(\underline{q},\omega) = \langle e^{i\underline{q}.\underline{d}} \int \sum_{j=1}^{N} \delta(\underline{r} - \underline{R}_j + \underline{d})\, \mathbf{T}(\underline{r},\omega)\, e^{i\underline{q}.\underline{r}}\, d^3r \rangle . \quad (4.19)$$

We now realize that, if $N \to \infty$,

$$\int \sum_{j=1}^{N} \delta(\underline{r} - \underline{R}_j + \underline{d})\, e^{i\underline{q}.\underline{r}}\, d^3r = \frac{8\pi^3}{v_c} e^{-i\underline{q}.\underline{d}} \sum_{\mathbf{l}} \delta(\underline{q} - \underline{K}_l)$$

(i.e. a sum in the reciprocal lattice $\underline{K}_l$), whereas the Fourier transform of $\mathbf{T}(\underline{r},\omega)$ is the well-known Oseen tensor in reciprocal space: $\mathbf{t}(\underline{q},\omega) = \eta^{-1}(q^2 + \alpha^2)^{-1}(\mathbf{I} - \hat{q}\hat{q})$, (Hasimoto 1959; Hurd *et al.* 1982) with $\alpha^2 = -i\omega\rho/\eta$ and v_c is the volume of a unit cell in real space: $v_c = R_0^3/2$. The lattice sum $\mathbf{T}(\underline{q},\omega)$ is the convolution of the two Fourier transforms:

$$\mathbf{T}(\underline{q},\omega) = \frac{1}{v_c \eta} \sum_{\mathbf{l}} \frac{\langle e^{i\underline{Q}_l \cdot \underline{d}} \rangle}{Q_l^2 + \alpha^2} (\mathbf{I} - \hat{Q}_l\hat{Q}_l), \quad \underline{Q}_l = \underline{q} - \underline{K}_l. \quad (4.20)$$

The $l=0$ term is separated from the sum and α^2 is neglected with respect to Q_l^2 in the remaining terms:

$$\mathbf{T}(\underline{q},\omega) = \mathbf{S}(\underline{q}) + \mathbf{Y}(\underline{q},\omega), \quad (4.21a)$$

$$\mathbf{S}(\underline{q}) = \frac{1}{v_c \eta} \sum_{l \neq 0} \frac{<e^{i\underline{Q}_l \cdot \underline{d}}>}{Q_l^2} (\mathbf{I} - \hat{Q}_l \hat{Q}_l), \tag{4.21b}$$

$$\mathbf{Y}(\underline{q},\omega) = \frac{1}{v_c \eta} \frac{<e^{i\underline{q} \cdot \underline{d}}>}{q^2 + \alpha^2} (\mathbf{I} - \hat{q}\hat{q}). \tag{4.21c}$$

Notice that $\mathbf{Y}(\underline{q},\omega)$ vanishes for longitudinal modes. The lattice sum $\mathbf{S}(\underline{q})$ was considered first by Hasimoto (1959), who was interested in the problem of sedimentation of lattices of spheres. It has been worked out to order a/R_0 ($\simeq \phi^{1/3}$, ϕ is the volume fraction occupied by the spheres) by Hurd *et al.* (1985):

$$\mathbf{S}(\underline{q}) = \frac{1}{6\pi\eta a} (\mathbf{I} - \kappa(\underline{q})\phi^{1/3}) . \tag{4.22}$$

Hurd *et al.* also provided a convenient polynomial expansion for $\kappa(\underline{q})$.

4.3. Example: $\underline{q}$ in the [100] direction

To gain some more insight in crystal dynamics, especially in hydrodynamic interaction, we focus on the relatively simple case of $\underline{q}$ lying in the [100] or x-direction. In this situation all tensors are diagonal, i.e. no rotation of coordinates is required to decouple the equations of motion (Eq. 4.16). The equation of motion in x-direction represents a longitudinal mode, the two identical equations in y- and z-direction represent transverse modes.

The x-component of Eq. 4.16 becomes ($\mathbf{T}_{xx}(\underline{q},\omega) \approx \mathbf{S}_{xx}(\underline{q})$)

$$a_q^x[-\omega^2 m - i\omega\, S_{xx}^{-1}(q) + D_{xx}(q)] = X_q^x . \tag{4.23}$$

This is written as

$$a_q^x[-\mu_q^x\, \omega^2 + (\omega_q^x)^2 - i\omega\, \lambda_q^x] = \frac{1}{m} X_q^x \ ; \tag{4.24}$$

the standard equation of motion of a damped harmonic oscillator, where ω_q^x is

its characteristic frequency; λ_q^x its damping and $m\mu_q^x$ its mass. For the longitudinal modes we thus find:

$$(\omega_q^x)^2 = D_{xx}(q)/m\ ;\ \lambda_q^x = S_{xx}^{-1}(q)/m = \frac{6\pi\eta a}{m}\left[1 - \kappa_{xx}(q)\phi^{1/3}\right]^{-1}\ ;\ \mu_q^x = 1\ .$$

Equation 4.18 is used to calculate $D_{xx}(q)$:

$$D_{xx}(q) = 8(A_1 + B_1/3)\,(1 - \cos\tfrac{qR_0}{2}) + 4(A_2 + B_2)\sin^2\tfrac{qR_0}{2}\ . \qquad (4.25)$$

In the case of dilute crystals the friction constant λ_q^x depends only weakly on the length of the wavevector q, it remains close to the Stokes value $6\pi\eta a/m$ for almost all q. The mass of the harmonic oscillator equals the mass of the particle. In all practical situations the damping is much larger than the mode frequency: $\lambda_q^x >> \omega_q^x$. Therefore these longitudinal modes will be strongly overdamped and will not show oscillatory behaviour.

The approximation $T_{xx}(q,\omega) \approx S_{xx}(q)$ obscures the fact that fluid inertia plays an important role in the dynamics of the longitudinal modes. This can be seen if we expand $T_{xx}(q,\omega)$ up to first order in α^2 instead of the zeroth-order approximation $T_{xx}(q,\omega) \approx S_{xx}(q)$:

$$T_{xx}(q,\omega) \approx S_{xx}(q) - \frac{\alpha^2}{v_c\eta}\left[\sum_{1\neq 0}\frac{\langle e^{i\underline{Q}_1\cdot\underline{d}}\rangle}{Q_1^4}(\mathbf{I} - \hat{Q}_1\hat{Q}_1)\right]_{xx}\ . \qquad (4.26)$$

The second term in Eq. 4.26 is written as $i\omega\, M(q)$. A lower boundary of $M(0)$ is obtained if the sum in Eq. 4.26 is constrained to the (four) reciprocal lattice points that are closest to the origin (at distance $\sqrt{2}\pi/R_0$). Then $M(0) \approx 2\rho R_0/(\pi^4\eta^2)$ (in the dilute-crystal limit $\langle e^{i\underline{K}_1\cdot\underline{d}}\rangle$ is unity). If the density of fluid and particles is equal we can write

$$T_{xx}^{-1}(q=0,\omega) \approx 6\pi\eta a[1 - \kappa_{xx}(0)\phi^{1/3}]^{-1} - i\omega\,\frac{54}{\pi^3}\,(\frac{8\pi}{3})^{1/3}\,m\,\phi^{-1/3}\ , \qquad (4.27)$$

and $\mu_q^x \approx 1 + 54/\pi^3(8\pi/3)^{1/3}\,\phi^{-1/3}$. Notice that the mass of the harmonic oscillator is dominated by fluid inertia because in general $\phi^{-1/3} >> 1$. As will

be explained in section 4.5, the experiment is insensitive to this added mass effect because it probes the relaxation rate Γ of overdamped vibrations: $\Gamma = (\omega_q^\alpha)^2/\lambda_q^\alpha$ (α = x, y or z).

The friction tensor (including its imaginary inertial part) for transverse modes in [100] direction is

$$T_{yy}(q,\omega) \approx S_{yy}(q) + \frac{1}{v_c \eta} \frac{<e^{i\underline{q}\cdot\underline{d}}>}{q^2 + \alpha^2} . \qquad (4.28)$$

In the dilute crystal limit , $qa \to 0$, the surface average $<e^{i\underline{q}\cdot\underline{d}}>$ is unity. The equation of motion for transverse crystal waves with $\underline{q}$ in the [100] direction (Eq. 4.16 in y-direction) may be multiplied by $S_{yy}(q)\,(q^2 + \alpha^2) + 1/(v_c\eta)$, yielding the algebraic equation:

$$a_q^y\,[\omega^3 + i\omega^2\,C_1 - \omega\,C_2 - iC_3] = -\frac{1}{m}[\omega + iC_4]\,X_q^y ; \qquad (4.29)$$

with $C_1 = \frac{\eta q^2}{\rho} + \frac{m_f + m}{m_f m}\,S_{yy}^{-1}(q)$; $C_2 = \frac{\eta q^2}{\rho m}\,S_{yy}^{-1}(q) + \frac{1}{m}\,D_{yy}(q)$;

$C_3 = [\frac{\eta q^2}{\rho m} + \frac{1}{m_f m}\,S_{yy}^{-1}(q)]D_{yy}(q)$; $C_4 = \frac{\eta q^2}{\rho} + \frac{1}{m_f}\,S_{yy}^{-1}(q)$;

where $m_f = \rho v_c$; in general $m_f >> m$. The three roots of the characteristic equation, i.e. the zero's of the third-order polynomial in the left-hand side of Eq. 4.29, constitute the spectrum of complex eigenfrequencies of the transverse mode. They are the key quantities of interest in a light scattering experiment, as will be explained in section 4.5. The ω-dependent term in the right-hand side of Eq. 4.29 is of interest for the relative amplitudes of the various relaxation rates of the crystal mode. If $C_1 >> C_2/C_1$ and $C_1 >> C_3/C_2$, which is guaranteed in most practical situations, an approximate root of the characteristic equation is $\omega = -iC_1$. The associated time dependence is dominated by $S_{yy}^{-1}(q)/m \approx 6\pi\eta a/m$. This is the decay rate of the velocity relaxation of Brownian motion, it is of the order of 10^9 Hz, i.e. too fast to observe in a light scattering experiment. If, besides the above stated conditions, $C_4^2 >> C_3/C_1$ the spectrum of the system that contains the two remainig singularities can be

well approximated by

$$[-\frac{C_1}{C_4}\omega^2 - i\omega\frac{C_2}{C_4} + \frac{C_3}{C_4}]a_q^\gamma = \frac{1}{m}X_q^\gamma \,. \tag{4.30}$$

This is the equation of motion of a damped harmonic oscillator. In terms of the physical parameters introduced in Eq. 4.24 and with $R_0 >> a$:

$$\mu_q^\gamma \approx \frac{1}{m}[q^2\eta S_{yy}(q)/\rho + 1/m_f]^{-1} \,,$$

$$\lambda_q^\gamma = \frac{1}{m}[1 + \frac{\rho}{q^2\eta}D_{yy}(q)\,S_{yy}(q)]/[S_{yy}(q) + \rho/(q^2\eta m_f)] \,;$$

since $\frac{\rho}{q^2\eta}D_{yy}(q)\,S_{yy}(q) << 1$:

$$\lambda_q^\gamma \approx \frac{1}{m}\left\{[1 - \kappa_{yy}(q)\phi^{1/3}]/(6\pi\eta a) + \rho/(q^2\eta m_f)\right\}^{-1} \,,$$

$$(\omega_q^\gamma)^2 = \frac{1}{m}D_{yy}(q) = \frac{1}{m}[8(A_1 + B_1/3)(1 - \cos\frac{qR_0}{2}) + 4A_2\sin^2\frac{qR_0}{2}]$$

(see Eq. 4.18). Long-wavelength transverse modes show some interesting features. The damping approaches zero and the mass approaches m_f (i.e the mass of fluid in a unit cell) if q is small. The conclusion is that these modes are characterized by coherent motion of fluid and particles. The small damping of long-wavelength transverse modes bears the promise of underdamped modes. The condition for modes to be underdamped is $\lambda_q^\gamma < 2\omega_q^\gamma\sqrt{\mu_q^\gamma}$. Since for small q $\lambda_q^\gamma \simeq q^2$ and $\omega_q^\gamma \simeq q$ propagating modes induced by Brownian motion can occur. In most practical situations, however, the condition is only satisfied for very long transverse waves with wavelengths that are comparable to the crystal size. For strongly overdamped modes, i.e. modes with $\lambda_q^\gamma >> \omega_q^\gamma\sqrt{\mu_q^\gamma}$ the two roots of the characteristic equation are $-i(\omega_q^\gamma)^2/\lambda_q^\gamma$ and $-i\lambda_q^\gamma/\mu_q^\gamma = -iq^2\eta/\rho$. The first is associated with the interplay of crystal elasticity and hydrodynamic friction; it will show a finite value for small q and is readily visible in a light scattering experiment. The second is connected with the relaxation of shear waves in the fluid (Boon & Yip 1980), for small q its decay rate is within the reach of a light

scattering experiment. These considerations illustrate the importance of experiments that probe long-wavelength transverse modes.

To reach the conclusions on inertia, damping and elasticity of transverse modes quite a lot of assumptions have been made. A numerical example may give some insight in the orders of magnitude of the various terms. Consider a colloidal crystal of polystyrene spheres in water; lattice parameter 1 μm, sphere radius 0.05 μm. $\eta = 10^{-3}$ Pa s; $\rho = 10^3$ kg m^{-3}. The density of water and polystyrene is almost equal. Spring constants will be of the order of 5 10^{-6} N m^{-1}. $S_{yy}^{-1}(q)$ does not show much dispersion, it is of the order of $6\pi\eta a \approx 10^{-9}$ N s m^{-1} from zone center to zone boundary.

* The factor C_1 is dominated by $\frac{m_f+m}{m_f m} S_{yy}^{-1} \approx 2\ 10^9$ s^{-1}.

* The characteristic frequency on the right-hand side of Eq. 4.29 is C_4. At the zone center ($q = 0$): $C_4 \approx 2\ 10^6$ s^{-1}; at the zone boundary ($q = 2\pi/R_0$): $C_4 \approx 4\ 10^7$ s^{-1}.

We made three major assumptions:

1. $C_1 >> C_2/C_1$. At the zone center $C_2 = 0$. C_2 reaches its maximum at the zone boundary: $C_2 \approx 10^{17}$ s^{-2}. Because $C_1 \approx 2\ 10^9$ s^{-1}, $C_2/C_1 \approx 4\ 10^7$ s^{-1}.
2. $C_1 >> C_3/C_2$. C_3/C_2 has its maximum at the zone boundary: $C_3/C_2 \approx 5\ 10^3$ s^{-1}.
3. $C_4^2 >> C_3/C_1$. At the zone center $C_3 = 0$; at the zone boundary $C_3 \approx 4\ 10^{20}$ s^{-3}. Indeed $C_4^2 >> C_3/C_1$.

4.4. Double layer effects in colloidal crystal dynamics

The hydrodynamic theory predicts a finite relaxation rate of overdamped transverse waves at the zone center. This prediction is at variance with the experimental results of Hurd *et al.* (1982) who found a vanishing relaxation rate $(\omega_q^Y)^2/\lambda_q^Y$ of long waves. This important discrepancy prompted Felderhof & Jones (1987) to reconsider the dynamics of colloidal crystals and to introduce

the effects of the ionic double layer in the theory. The basic idea is that the ionic double layer which surrounds each particle is deformed when the particle moves through the fluid. The ions, having finite diffusivity, cannot follow the particle motion instantaneously. Three effects are important. The first is the so called ionic friction: the deformed double layer exerts a drag force on the particle that it surrounds. The second effect is dipole interaction. The deformed double layers constitute, together with the particles, dipoles that have long-range interactions. The third effect is a frequency dependence of the elastic tensor. Due to the finite diffusivity of the counter ions the springs between the particles do not react instantaneously on particle motion.

In this section there is a short sketch of the simplified model developed by Felderhof & Jones (1987) together with its consequences for the phonon spectra. I believe that there are a few caveats to the model described. The first, that was also noted by Felderhof & Jones, is that the model ignores the effect of fluid flow around the moving particle in restoring the ionic balance. The second caveat is (see also Fixman 1987) that double layer effects should be smallest when the relative motion of particles and fluid is least, i.e. for long-wavelength transverse vibrations. Therefore it would be surprising if the addition of electrodynamic effects to the theory sketched in the previous section would cure the noticed discrepancy in the relaxation rates.

In the static situation each particle is surrounded by its Debye cloud, with potential

$$\psi(\underline{r}-\underline{R}_j,\kappa) = Ze\,\frac{e^{-\kappa|\underline{r}-\underline{R}_j|}}{4\pi\epsilon|\underline{r}-\underline{R}_j|}\,; \qquad (4.31)$$

where κ^{-1} is the Debye length (κ^2 is the ionic strength: $\kappa^2 = n_0 z^2 e^2/\epsilon k_B T$; n_0 is the counter ion density, ze is the counter ion charge and ϵ is the dielectric constant of the fluid). When the particles oscillate about their equilibrium position the counter ion density around particle j is perturbed both due to the motion of the particle itself and due to long-range interactions with induced dipoles associated with all other particles that have moved from their equilibrium positions. The motion of the sea of counter ions is described by a generalized diffusion equation.

Accordingly the electrodynamic force can be split into two parts $\underline{H}_j$ and $\underline{G}_j$ and the Langevin equation becomes:

$$m \frac{d\underline{u}_j}{dt} = \underline{F}_j - \underline{f}_j + \underline{G}_j + \underline{H}_j + \underline{X}_j. \tag{4.32}$$

The term $\underline{G}_j$ represents the friction due to deformation of its own Debye cloud by the particle itself; the term $\underline{H}_j$ embodies long-range dipole interactions. In the frequency domain:

$$\underline{G}_j = \frac{\kappa^2}{12\pi\epsilon} (\kappa - \lambda)\ Z^2 e^2\ \underline{s}_j \equiv i\omega\ \zeta_e(\omega)\ \underline{s}_j\ , \tag{4.33}$$

where $\lambda^2 = \kappa^2 - i\omega/D_i$ and D_i is the diffusion constant of the ions. The effect of ionic friction on particles undergoing free Brownian motion in low ionic–strength fluids has been experimentally studied by Schumacher & Van de Ven (1987) who tested a theory by Ohshima *et al.* (1984). When the Debye length is much larger than the particle radius the theory yields the ζ_e of Eq. 4.33 for $\omega = 0$. In order to characterize the strongly deionized solution out of which the crystals were grown, the experiments by Schumacher & Van de Ven were repeated. The results, described in appendix 1, show that the effect of ionic friction on diffusion is of the order of magnitude predicted by the theory.

The force due to the interactions with dipoles created by the other particles is:

$$\underline{H}_j = \frac{Ze}{4\pi\epsilon} \sum_{\substack{k=1 \\ k\neq j}}^{N} \mathbf{U}(\underline{R}_j - \underline{R}_k)\cdot\underline{p}_k \quad ; \quad \mathbf{U}(\underline{r}) = \frac{\mathbf{I} - 3\hat{r}\hat{r}}{r^3}, \tag{4.34}$$

where $\mathbf{U}(\underline{r})$ is the dipole tensor and $\underline{p}_k$ is the dipole strength induced by the particle and its ionic cloud at lattice site $\underline{R}_k$. Normal mode expansion of $\underline{p}_k$ leads to

$$\underline{H}_q = \mathbf{U}(\underline{q})\cdot\underline{p}_q \quad ; \quad \mathbf{U}(\underline{q}) = \frac{Ze}{4\pi\epsilon} \sum_{j=1}^{N}{}' \mathbf{U}(\underline{R}_j)\ e^{i\underline{q}\cdot\underline{R}_j}, \tag{4.35}$$

where the prime indicates that the origin is excluded. In Felderhof & Jones

(1987) expressions for $\underline{p}_q$ and for $\mathbf{U}(\underline{q})$ in the limit of vanishing wavevector are presented:

$$\underline{p}_q = i\omega \frac{Ze}{D_i \lambda^2} \underline{a}_q, \quad \mathbf{U}_0(\underline{q}) = -\frac{Ze}{3 v_c \epsilon} (\mathbf{I} - 3\hat{q}\hat{q}).$$

The ω-dependence of the elastic tensor $\mathbf{D}(\underline{q},\omega)$ is fully contained in λ (Felderhof & Jones 1987):

$$\mathbf{D}(\underline{q},\omega) = Ze \sum_{j=1}^{N}{}' \left[\nabla\nabla\, \psi(\underline{R}_j,\kappa) - \frac{\kappa^2}{\lambda^2} \nabla\nabla\, \psi(\underline{R}_j,\lambda) e^{i\underline{q}.\underline{R}_j} \right] \tag{4.36}$$

with $\psi(\underline{r},\lambda) = Ze\, e^{-\lambda r}/(4\pi\epsilon r)$. If $\kappa = \lambda$ (i.e. if $D_i \to \infty$ or $\omega = 0$) Eq. 4.36 reduces to Eq. 4.14. The equation of motion for a phonon with wavevector $\underline{q}$ becomes:

$$\underline{f}_q - \omega^2 m \underline{a}_q + \mathbf{D}(\underline{q},\omega).\underline{a}_q - i\omega \left[\frac{Ze}{D_i \lambda^2} \mathbf{U}(\underline{q}) + \zeta_e(\omega)\, \mathbf{I} \right].\underline{a}_q = \underline{X}_q. \tag{4.37}$$

Crystal dynamics is described by this equation together with Eq. 4.13 which accounts for the hydrodynamics. We focus on phonons with $\underline{q}$ in [100] direction; the tensors are diagonal for these phonons. The combination of Eqs. 4.13, 4.21 and 4.37 in x-direction reads

$$a_q^x \left[m\omega^2 + i\omega \left[S_{xx}^{-1}(q) + \frac{Ze}{D_i \lambda^2} U_{xx}(q) + \zeta_e(\omega) \right] - D_{xx}(q,\omega) \right] = -X_q^x, \tag{4.38}$$

i.e. the damping of longitudinally polarized crystal waves consists of hydrodynamic friction supplemented with the effects of dipole interactions and ionic friction. For transverse modes the constants of Eq. 4.29 become:

$$C_1 = \frac{\eta q^2}{\rho} + \frac{m_f + m}{m_f m} S_{yy}^{-1}(q) + \frac{1}{m} \left[\frac{Ze}{D_i \lambda^2} U_{yy}(q) + \zeta_e(\omega) \right];$$

$$C_2 = \frac{\eta q^2}{\rho m} S_{yy}^{-1}(q) + \frac{1}{m} D_{yy}(q,\omega) + \left[\frac{1}{m_f m} S_{yy}^{-1}(q) + \frac{\eta q^2}{\rho m} \right] \left[\frac{Ze}{D_i \lambda^2} U_{yy}(q) + \zeta_e(\omega) \right];$$

$$C_3 = [\frac{\eta q^2}{\rho m} + \frac{1}{m m_f} S_{yy}^{-1}(q)] D_{yy}(q,\omega) \; ; \; C_4 = \frac{\eta q^2}{\rho} + \frac{1}{m_f} S_{yy}^{-1}(q) \; .$$

In the characteristic equations of both longitudinal and transverse modes the frequency dependence contained in $Ze/(D_i\lambda^2)$ introduces a new root which is related to the time an ion needs to diffuse over a Debye length: $\omega_\kappa = -iD_i\kappa^2$.

The damping of the transverse waves can be approximated similarly to that in the hydrodynamic case (see Eq. 4.30)

$$\lambda_q^\gamma = \frac{1}{m}\Big[1 + [S_{yy}(q) + \frac{\rho}{m_f \eta q^2}][\frac{Ze}{D_i \lambda^2} U_{yy}(q) + \zeta_e(\omega)]\Big] \Big[S_{yy}(q) + \frac{\rho}{m_f \eta q^2}\Big]^{-1} . \quad (4.39)$$

In marked contrast with the case with only hydrodynamic interaction, the damping at infinite wavelengths remains finite:

$$\lambda_q^\gamma = \frac{1}{m} \frac{Z^2 e^2}{3\kappa^2 \epsilon D_i} \Big[\frac{\kappa^3}{8\pi} - \frac{2}{R_0^3} \Big] .$$

An apparent defect of the theory is that the damping of transverse modes can be negative, depending on the parameters of the crystal.

A numerical example may give an idea of the relative importance of the double layer effect. Starting point is a crystal consisting of $a = 0.05$ μm particles and lattice parameter $R_0 = 1$ μm. Further we take $Z = 500$ and $\kappa R_0 = 3$. H^+ ions in water have diffusion constant $D_i = 9.5\ 10^{-9}$ m^2s^{-1}; OH^- ions in water have $D_i = 5.4\ 10^{-9}$ m^2s^{-1} (Moore 1972). We take $D_i = 7.5\ 10^{-9}$ m^2s^{-1}. Stokes friction equals $6\pi\eta a \approx 10^{-9}$ Nsm^{-1}. Stokes friction is compared to ionic friction and the dipole effect: $\zeta_e(\omega=0) \approx 5\ 10^{-11}$ Nsm^{-1}; $Ze/(D_i\kappa^2)\ U_{0xx}(q) \approx 2\ 10^{-10}$ Nsm^{-1}; $Ze/(D_i\kappa^2)\ U_{0yy}(q) \approx -1\ 10^{-10}$ Nsm^{-1} . With these numerical values the (imaginary) characteristic frequency connected with ionic diffusion becomes $i\omega_\kappa \approx 6\ 10^4$ s^{-1} ; a frequency that is well within the reach of dynamic light scattering experiments.

Chapter 5 LIGHT SCATTERING EXPERIMENTS ON SINGLE COLLOIDAL CRYSTALS

5.1. Introduction

In low ionic-strength fluids colloidal crystals with lattice parameters up to 1.5 μm can be grown. Therefore a large region of the reciprocal lattice can be covered by scattering experiments with visible light. The scattering pattern in transmission one sees when a beam of monochromatic light (with wavelength λ) hits a single crystal is the surface of an Ewald sphere with radius $2\pi/\lambda$ in the reciprocal lattice. Bragg diffraction occurs when the beam and the crystal are mutually oriented in such a way that points of the reciprocal lattice fall on the Ewald sphere. Crystal vibrations initiated by Brownian motion cause diffuse scattering outside Bragg directions (Debye-Waller effect). This flickering anisotropic background of scattered light contains information on the dynamics of the crystal. It has been probed by means of photon correlation spectroscopy (Hurd *et al.* 1982). These experiments show similarity with neutron scattering off atomic solids. Inelastic neutron scattering is employed to measure the dispersion of crystal waves (phonons). From the energy of the scattered neutrons the frequency of the phonons can be derived (Cochran 1973). In the same manner spectral information on the light scattered off a colloidal crystal (obtained by photon correlation spectroscopy) can be used to determine dispersion functions of colloidal crystals.

Light scattering experiments on fairly concentrated colloids (like colloidal crystals) often suffer from multiple scattering: light has been scattered by more than one particle before it reaches the detector. A meaningful interpretation of light scattering data, however, requires detection of singly scattered light. A way to reduce multiple scattering is the use of a thin sample; a sample that is typically thinner than the mean-free path of a photon in the colloid. In their experiments Hurd *et al.* (1982) probed crystals that were grown between two parallel quartz windows close to one another (of the order of 50 μm). Additional advantages of such a thin-film cell setup are in the first place the possibility to identify and probe single crystals and, in the second place, the restriction that is imposed upon the crystal orientation by the bounding walls of the sample cell. Dilute colloidal crystals in general have a BCC structure. The crystals will

orient themselves with their closest-packed planes (the (110)-planes) parallel to the cell walls (Clark *et al.* 1979). Therefore recognition of the order of Bragg scattering becomes very simple. The major disadvantage of the use of a thin cell is the likely influence of the bounding walls on the crystal dynamics, especially on the damping of crystal waves.

The intimate relation between the light scattering geometry and the normal crystal mode whose dynamics is probed in the experiment is the subject of the sections 5.2 and 5.3. In sections 5.4 and 5.5 our experimental setup is described and experimental results are presented. The experiments were guided by the experimental work by Hurd *et al.* (1982). For a large part we used the same techniques as they did, including the concept of the thin-film sample cell. An extension of the experiment is the use of the heterodyne detector described in chapter 2. Heterodyne experiments are prefered because of the ambiguous nature of homodyne correlation functions that suffer from partial heterodyning and because of the a-priori unknown statistics of the light scattered off a colloidal crystal. In many light scattering experiments in disordered systems one can assume Gaussian statistics of the scattered electric field and use the Siegert relation to go from intensity correlation functions to field correlation functions (see e.g. Schätzel 1987 or chapter 2). Colloidal crystals consist of strongly interacting particles and in principle have an infinite spatial correlation length. The validity of the Siegert relation is not obvious. Sections 5.6 and 5.7 close the chapter with a discussion and with a tentative model for the effects of the sample-cell walls on crystal dynamics.

5.2. Dynamic light scattering off colloidal crystals

A schematic view of part of the experimental setup that is relevant for the scattering geometry is given in Fig. 5.1. The crystal is grown in a thin-film cell and illuminated by a laser beam. The scattered light intensity is detected by a photomultiplier. In some cases it may be advantageous to mix the scattered light with a reference beam that is split off the incident laser beam. To that aim the reference beam is transported through a single-mode polarization preserving optical fiber. A judicious choice of the scattering geometry defines the crystal

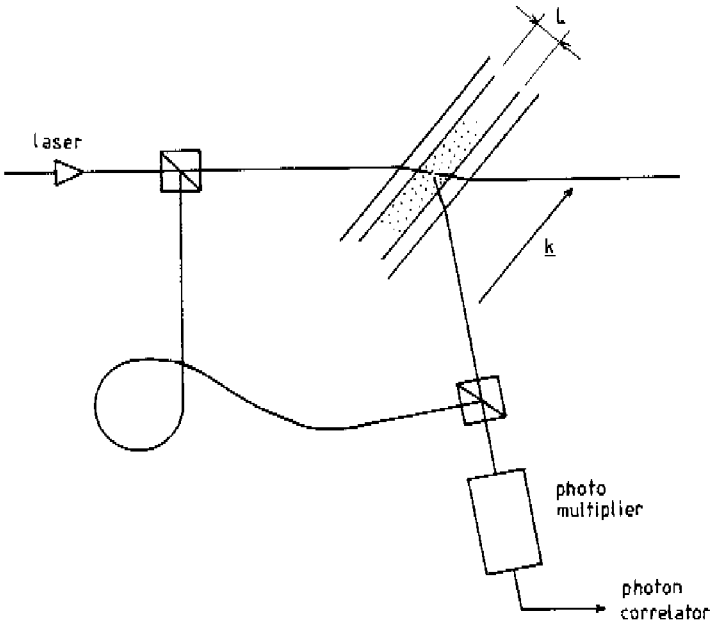

Fig. 5.1 Schematic view of the light scattering setup for probing crystal dynamics. Crystals are grown in a thin cell. Light scattered by the particles is detected by a photomultiplier. The scattered light may be mixed on the detector with a reference beam that is guided through an optical fiber.

modes whose Brownian dynamics is probed in the experiment. The aim of this section is elucidation of the relation between experimental geometry and the internal crystal modes that are detected. Furthermore the relation between the statistical properties of Brownian modes and the statistical properties of the scattered light is discussed. The principal instrument to characterize the statistical properties of the scattered light will be the correlation function.

The self- or homodyne correlation function of the scattered light is defined by:

$$G_{hom}(\tau) = \tfrac{1}{4}\epsilon_0^2 c^2 \langle E(\underline{k},0)\, E^*(\underline{k},0)\, E(\underline{k},\tau)\, E^*(\underline{k},\tau)\rangle, \qquad (5.1)$$

where $E(\underline{k},t)$ is the (complex) scattered field amplitude and $\underline{k}$ is the scattering vector. Angular brackets denote an average over time. When the scattered light is mixed with that of a much more intense reference beam, the correlation function (the so-called heterodyne correlation function) becomes (cf. Eq. 2.10):

$$G_{het}(\tau) = I_r^2 + I_r\, \epsilon_0 c\, \mathrm{Re}\langle E(\underline{k},0)\, E^*(\underline{k},\tau)\rangle + \\ + \tfrac{1}{2}\epsilon_0^2 c^2\, \mathrm{Re}[E_r^*\, E_r^*\, \langle E(\underline{k},0)\, E(\underline{k},\tau)\rangle]; \qquad (5.2)$$

where $I_r = \tfrac{1}{2}\epsilon_0 c\, E_r\, E_r^*$ (the index r refers to the reference beam). For a colloidal crystal we will explore all three of the following correlations: $\langle E(\underline{k},0)\, E^*(\underline{k},\tau)\rangle$, $\langle E(\underline{k},0)\, E(\underline{k},\tau)\rangle$ and $\langle E(\underline{k},0)\, E^*(\underline{k},0)\, E(\underline{k},\tau)\, E^*(\underline{k},\tau)\rangle$. Comparison of the second- and fourth-order correlations is of relevance for inferring the statistical properties of scattered light.

The scattered electric field is a coherent sum of contributions associated with the individual particles, each of which scatters according to the Born approximation:

$$E(\underline{k},t) = \sum_{j=1}^{N} E_0[\underline{r}_j(t)]\, e^{i\underline{k}\cdot\underline{r}_j(t)};\ \underline{k} = \underline{k}_i - \underline{k}_s\ , \qquad (5.3)$$

where $E_0(\underline{r})$ is the incident field amplitude distribution. It is determined by the beam profile, the collecting optics and the cell geometry. The first correlation function, that of the electric field, reads explicitly:

$$g_1(\underline{k},\tau) \equiv \langle E(\underline{k},0)\, E^*(\underline{k},\tau)\rangle = \sum_{j,l} \langle E_0^*[\underline{r}_j(\tau)]\, E_0[\underline{r}_l(0)]\, e^{-i\underline{k}\cdot[\underline{r}_j(\tau)-\underline{r}_l(0)]}\rangle. \qquad (5.4)$$

The particle positions are written as a sum of their equilibrium lattice positions and a random component which is assumed to be much smaller than the wavelength of light: $\underline{r}_j(t) = \underline{R}_j + \underline{s}_j(t)$, with $\langle \underline{k}\cdot\underline{s}_j(t)\rangle = 0$ and $\langle[\underline{k}\cdot\underline{s}_j(t)]^2\rangle << 1$. Expansion of the exponential in Eq. 5.4 then yields :

$$g_1(\underline{k},\tau) = \sum_j E_0^*[\underline{R}_j]\, E_0[\underline{R}_1]\, e^{-i\underline{k}.(\underline{R}_j - \underline{R}_1)} \Big[1 + \langle s_j^k(\tau)\, s_j^k(0)\rangle + \\ - \langle s_j^k(0)\, s_j^k(0)\rangle + O[\langle s_j^k\rangle^4]\Big] , \quad (5.5)$$

where $s_j^k(t) \equiv \underline{k}.\underline{s}_j(t)$ and where stationarity of the correlation function is invoked. The scattered amplitudes $E_0[\underline{r}_j]$ have been replaced by the amplitudes at the lattice sites $E_0[\underline{R}_j]$. This is allowed because the components of $\underline{s}_j(t)$ are very much smaller than the linear size of the scattering volume. In order to unravel the contribution of elementary lattice-vibration modes to the electric field correlation function, we can rewrite the right-hand side of Eq. 5.5 as a sum over reciprocal space. Using the identity

$$\sum_j e^{i\underline{q}.\underline{R}_j} = \frac{8\pi^3}{v_c} \sum_l \delta(\underline{q} - \underline{K}_l) ,$$

where $\underline{K}_l$ is a reciprocal lattice vector, and v_c $(= {R_0}^3/2\ )$ is the volume of a unit cell, we obtain:

$$\sum_j E_0[\underline{R}_j]\, e^{i\underline{q}.\underline{R}_j} = \frac{8\pi^3}{v_c} \sum_l P(\underline{q} - \underline{K}_l). \quad (5.6)$$

The function $P(\underline{q})$ is the Fourier transform of $E_0(\underline{r})$. It is sharply peaked because $E_0(\underline{r})$ extends over many wavelengths of light. The characteristic size of the scattering volume is of the order of 200λ, consequently, $P(\underline{q})$ will have a width of about $(200\lambda)^{-1}$. Because the typical lattice parameters realized in our experiments are of the order of 2λ, the width of $P(\underline{q})$ is small compared with $|\underline{K}_1|$ $(\approx 2\pi/2\lambda)$. Control over the width of the form factor $P(\underline{q})$ can be obtained by changing the size of the focus of the incident light. In appendix 3 I discuss correlation measurements with two detectors that span a reciprocal lattice spacing. These experiments could only be done by increasing the width of $\lambda P(\underline{q})/2\pi$ to a few milliradians. Normal mode expansion of the particle excursions $\underline{s}_j(t)$:

$$\underline{s}_j(t) = \sum_q \underline{a}_q(t)\, e^{i\underline{q}.\underline{R}_j} \quad (\underline{q} \in \mathrm{FBZ};\ \text{because}\ \underline{s}_j(t) \in \mathbb{R}^3\ \ \underline{a}_q(t) = \underline{a}^*_{-q}(t)),$$

and substitution of Eq. 5.6 into Eq. 5.5 leads to

$$g_1(\underline{k},\tau) = \left[\frac{8\pi^3}{v_c}\right]^2 \sum_{\underline{l}_1}\sum_{\underline{l}_2}\Big[\, P^*(\underline{k}-\underline{K}_{l_1})\, P(\underline{k}-\underline{K}_{l_2}) +$$

$$- \sum_{\underline{q}_1}\sum_{\underline{q}_2} P^*(\underline{k}-\underline{q}_1+\underline{q}_2-\underline{K}_{l_1})\, P(\underline{k}-\underline{K}_{l_2}) <a^{\underline{k}}_{\underline{q}_1}(0)\, a^{\underline{k}}_{\underline{q}_2}{}^*(0)> +$$

$$+ \sum_{\underline{q}_1}\sum_{\underline{q}_2} P^*(\underline{k}-\underline{q}_1-\underline{K}_{l_1})\, P(\underline{k}-\underline{q}_2-\underline{K}_{l_2}) <a^{\underline{k}}_{\underline{q}_1}(\tau)\, a^{\underline{k}}_{\underline{q}_2}{}^*(0)> \Big]\,, \quad (5.7)$$

where $a^{\underline{k}}_{\underline{q}} \equiv \underline{k}.\underline{a}_{\underline{q}}$. The interpretation of Eq. 5.7 is simplified when it is noticed that $g_1(\underline{k},0)$ is proportional to the time-averaged light intensity scattered by the crystal as a function of the scattering angle. The scattering vector $\underline{k}$ is confined to an Ewald sphere surface in reciprocal space. Bragg scattering occurs when the crystal is oriented such that one or more reciprocal lattice points fall on this Ewald sphere. The time-averaged intensity of Bragg scattering is given by the first two terms in the right-hand side of Eq. 5.7. Light is scattered outside Bragg directions by Brownian crystal modes. The third, and only time-dependent term in the right-hand side of Eq. 5.7 represents the autocorrelation function of this fluctuating light. The choice of a scattering vector $\underline{k}$ in the experiment restricts the detected crystal modes to a narrow range of $\underline{q}$-vectors, the narrower as the size of the scattering volume increases.

When we select $\underline{q}$-vectors in special symmetry directions of the crystal the tensors $\mathbf{T}^{-1}(\underline{q},\omega)$ and $\mathbf{D}(\underline{q})$ in the equation of motion for a single phonon (Eq. 4.16) can be diagonalised simultaneously by a simple rotation of axes. This coordinate system in which the three equations of motion for a phonon with wavevector $\underline{q}$ are decoupled is represented by the unit vectors $\underline{\alpha}$, $\underline{\beta}$ and $\underline{\gamma}$. The phonon spectrum in the direction of $\underline{\alpha}$, i.e. $a^{\alpha}_{\underline{q}}(\omega) \equiv \underline{\alpha}.\underline{a}_{\underline{q}}(\omega)$ can be written as (see Eq. 4.24):

$$a^{\alpha}_{\underline{q}}(\omega) = \frac{1}{m}\, X^{\alpha}_{\underline{q}}(\omega)/[-\mu^{\alpha}_{\underline{q}}\,\omega^2 + (\omega^{\alpha}_{\underline{q}})^2 - i\omega\,\lambda^{\alpha}_{\underline{q}}]. \quad (5.8)$$

The correlation properties of the random force $X^{\alpha}_{\underline{q}}(t)$ are determined by the thermal equilibrium between the excited lattice modes and their environment:

$$<X^{\alpha}_{q}> = 0 \; ; \; <X^{\alpha}_{q_1}(0)\, X^{\beta *}_{q_2}(\tau)> = 2m\, \lambda^{\alpha}_{q_1}\, k_B T\, \delta_{q_1 q_2}\, \delta_{\alpha\beta}\, \delta(\tau). \qquad (5.9)$$

Because $a^{\alpha}_{q}(t)$ is a stationary process we have a simple relation between the second moments of $a^{\alpha}_{q}(t)$ and $a^{\alpha}_{q}(\omega)$:

$$<a^{\alpha}_{q_1}(\omega_1)\, a^{\beta *}_{q_2}(\omega_2)> = 2\pi\, \delta(\omega_1 - \omega_2)\, A^{\alpha\beta}_{q_1 q_2}(\omega_1)\,, \qquad (5.10)$$

where

$$A^{\alpha\beta}_{q_1 q_2}(\omega) = \int_{-\infty}^{\infty} A^{\alpha\beta}_{q_1 q_2}(\tau)\, e^{-i\omega\tau}\, d\tau \quad \text{and} \quad A^{\alpha\beta}_{q_1 q_2}(\tau) \equiv <a^{\alpha}_{q_1}(0)\, a^{\beta *}_{q_2}(\tau)>. \qquad (5.11)$$

This yields

$$g_1(\underline{k},\tau) = \left[\frac{8\pi^3}{v_c}\right]^2 \sum_{\tau} \Big[|P(\underline{k} - \underline{K}_1)|^2 \,[1 - \sum_{q} \sum_{\alpha} C^{\alpha}_{q}\, (k^{\alpha})^2\, I^{\alpha}_{q}(0)] +$$

$$+ \sum_{q} [\, |P(\underline{k} - \underline{q} - \underline{K}_1)|^2 \sum_{\alpha} C^{\alpha}_{q}\, (k^{\alpha})^2\, I^{\alpha}_{q}(\tau)\,] \Big]\,, \qquad (5.12)$$

with $C^{\alpha}_{q} = 2k_B T\, \lambda^{\alpha}_{q}/m$ and

$$I^{\alpha}_{q}(\tau) = \int_{-\infty}^{\infty} \frac{e^{i\omega\tau}}{[(\omega^{\alpha}_{q})^2 - \mu^{\alpha}_{q}\omega^2 - i\omega\lambda^{\alpha}_{q}]\;[\,(\omega^{\alpha}_{q})^2 - \mu^{\alpha}_{q}\omega^2 + i\omega\lambda^{\alpha}_{q}]}\, d\omega\,. \qquad (5.13)$$

In the time-independent part of Eq. 5.12 we recognize Bragg scattering ($\underline{k} = \underline{K}_1$). Due to particle excursions from lattice sites part of the light is scattered outside Bragg directions. The scattering vector $\underline{k}$ selects light scattered by phonons $\underline{q}$ in a small interval centered at $\underline{q}_0 = \underline{k} - \underline{K}_1$. This light contributes to the time-dependent part of $g_1(\underline{k},\tau)$. The integral is evaluated with the method of residues, with the result:

$$I^{\alpha}_{q}(\tau) = \frac{\pi e^{-\Lambda\tau}}{2(\mu^{\alpha}_{q})^2(\Omega^2 + \Lambda^2)\Omega\Lambda}\, [\Omega\, \cos\Omega\tau + \Lambda\, \sin\Omega\tau], \qquad (5.14)$$

where $\Lambda = \lambda_q^\alpha/(2\mu_q^\alpha)$ and $\Omega^2 = (\omega_q^\alpha)^2/\mu_q^\alpha - (\lambda_q^\alpha)^2/(2\mu_q^\alpha)^2$. In case of strong damping (i.e. $\lambda_q^\alpha >> \omega_q^\alpha \sqrt{\mu_q^\alpha}$), which applies for almost all modes

$$I_q^\alpha(\tau) \simeq \frac{\lambda_q^\alpha}{(\omega_q^\alpha)^2} e^{-(\omega_q^\alpha)^2\tau/\lambda_q^\alpha} - \frac{\mu_q^\alpha}{\lambda_q^\alpha} e^{-\lambda_q^\alpha\tau/\mu_q^\alpha} \qquad (5.15)$$

(the symbol $\simeq$ denotes proportionality). According to Eq. 5.15 the time dependence of the scattered light intensity correlation function is a sum of exponentials involving the zero's of the characteristic equation. Each contribution is weighted by the inverse of the corresponding zero. This is also true when the dynamics of the crystal is more complex, for example when there are retarded electrodynamical forces and the characteristic equation has more than two roots. In most cases the second term in Eq. 5.15 cannot be observed in a light scattering experiment because its decay rate is too large. The integral then reduces to a single exponential that does not contain the inertial factor μ_q^α. As has been explained in section 4.3, the characteristic frequencies depend strongly on the wavelength. In the case of long-wavelegth transverse modes $\omega_q^\alpha \simeq q$ and $\lambda_q^\alpha \simeq q^2$, therefore these modes may become propagating at large enough wavelength, and

$$I_q^\alpha(\tau) \simeq e^{-\lambda_q^\alpha\tau/(2\mu_q^\alpha)} \cos \Omega\tau. \qquad (5.16)$$

The function $g_1(\underline{k},\tau)$ is periodic in reciprocal space, i.e. $g_1(\underline{k},\tau)$ is invariant under a translation over a reciprocal lattice vector. As an interesting consequence one can expect coherence between light scattered in directions that are separated by a reciprocal lattice vector. This hypothesis is tested in a cross-correlation experiment that is described in appendix 3. Mutual coherence of light scattered in two directions was indeed observed.

The second correlation to be investigated (see Eq. 5.2) is $h_1(\underline{k},\tau) \equiv <E(\underline{k},0)\, E(\underline{k},\tau)>$. In the same manner as we did for $g_1(\underline{k},\tau)$ we can derive $h_1(\underline{k},\tau)$ in terms of $P(\underline{q})$ and $I_q^\alpha(\tau)$. The result is:

$$h_1(\underline{k},\tau) = \left[\frac{8\pi^3}{v_c}\right]^2 \sum_{l_1} \sum_{l_2} \Big[[P(\underline{k}-\underline{K}_{l_1})]^2 \, [1 - \sum_{\underline{q}} \sum_{\alpha} C_{\underline{q}}^{\alpha} \, (k^{\alpha})^2 \, I_{\underline{q}}^{\alpha}(0)] +$$

$$- \sum_{\underline{q}} [\, P(\underline{k}+\underline{q}-\underline{K}_{l_1}) \, P(\underline{k}-\underline{q}-\underline{K}_{l_2}) \sum_{\alpha} C_{\underline{q}}^{\alpha} \, (k^{\alpha})^2 \, I_{\underline{q}}^{\alpha}(\tau) \,] \Big] \, . \quad (5.17)$$

The important difference with the expression for $g_1(\underline{k},\tau)$ is that the time-dependent part of $h_1(\underline{k},\tau)$ equals zero except for special values of $\underline{q}$. Only for $\underline{q}$ near zero (and $l_1 = l_2$) and for $\underline{q}$ near $(\underline{K}_{l_1} - \underline{K}_{l_2})/2$ (i.e. near the FBZ center and FBZ boundaries) $h_1(\underline{k},\tau)$ contributes to the heterodyne correlation function. At these specific spots the time dependence is represented by the integral $I_{\underline{q}}^{\alpha}(\tau)$.

In random Brownian media the correlation function of the scattered intensity is related to that of the scattered optical field via the Siegert relation as was discussed in section 2.3. A crucial ingredient of the argumentation was that the Brownian particles are scattered randomly over a scattering volume that is large with respect to the inverse scattering vector. This is clearly violated in the case of colloidal crystals where the scatterers are at orderly positions. We will show that, at least to first order in the particle excursions, there is an analogous relation between the scattered electric field and the scattered intensity correlation function. The correlation function of the scattered light intensity is proportional to

$$g_2(\underline{k},\tau) \equiv \langle E(\underline{k},0) \, E^{*}(\underline{k},0) \, E(\underline{k},\tau) \, E^{*}(\underline{k},\tau) \rangle = \sum_{jlmn} E_0^{*}[\underline{R}_j] \, E_0[\underline{R}_l] \, E_0^{*}[\underline{R}_m] \, E_0[\underline{R}_n]$$

$$e^{-i\underline{k}.(\underline{R}_j - \underline{R}_l + \underline{R}_m - \underline{R}_n)} \, \langle e^{-i[s_j^k(0) - s_l^k(0) + s_m^k(\tau) - s_n^k(\tau)]} \rangle \, . \quad (5.18)$$

The average in Eq. 5.18 is taken over fourth-order correlations that cannot be separated in second order correlations because the factors are no longer individually Gaussian. However, when the particle excursions are small with respect to $|\underline{k}|^{-1}$ the expansion of the exponential can be truncated after the second non-zero (fourth-order) term. Outside Bragg directions $g_2(\underline{k},\tau)$ can then be written as

$$g_2(\underline{k},\tau) = \left[\frac{8\pi^3}{v_c}\right]^4 \sum_{l_i} \sum_{q_i} P^*(\underline{k} - \underline{q}_1 - \underline{K}_{l_1})\, P(\underline{k} + \underline{q}_2 - \underline{K}_{l_2})\, P^*(\underline{k} - \underline{q}_3 - \underline{K}_{l_3})$$

$$P(\underline{k} + \underline{q}_4 - \underline{K}_{l_4}) \langle a^k_{q_1}(0)\, a^k_{q_2}(0)\, a^k_{q_3}(\tau)\, a^k_{q_4}(\tau)\rangle. \qquad (5.19)$$

The time-dependent particle excursions are linear in their Brownian driving force, which is assumed to be Gaussian (Wang & Uhlenbeck 1945). Therefore, each of the factors in the average in Eq. 5.19 is assumed to be Gaussian and it can be separated according to (see e.g. Gardiner 1983)

$$\langle a^k_{q_1}(0)\, a^k_{q_2}(0)\, a^k_{q_3}(\tau)\, a^k_{q_4}(\tau)\rangle = \langle a^k_{q_1}(0)\, a^k_{q_2}(0)\rangle \langle a^k_{q_3}(\tau)\, a^k_{q_4}(\tau)\rangle +$$

$$+ \langle a^k_{q_1}(0)\, a^k_{q_3}(\tau)\rangle \langle a^k_{q_2}(0)\, a^k_{q_4}(\tau)\rangle + \langle a^k_{q_1}(0)\, a^k_{q_4}(\tau)\rangle \langle a^k_{q_2}(0)\, a^k_{q_3}(\tau)\rangle. \qquad (5.20)$$

Substitution of Eq. 5.20 into Eq. 5.19 and $\underline{s}_j \in \mathbb{R}^3$, which implies $a^k_{-q} = a^{k\,*}_q$ gives the Siegert relation for the scattered electric field:

$$\langle E(\underline{k},0)\, E^*(\underline{k},0)\, E(\underline{k},\tau)\, E^*(\underline{k},\tau)\rangle = |\langle E(\underline{k},0)\, E^*(\underline{k},0)\rangle|^2 +$$

$$+ |\langle E(\underline{k},0)\, E^*(\underline{k},\tau)\rangle|^2 + |\langle E(\underline{k},0)\, E(\underline{k},\tau)\rangle|^2. \qquad (5.21)$$

The condition for $E(\underline{k},t)$ obeying the Siegert relation in light scattering experiments on colloidal crystals is very different from the condition in a random medium. In a random medium the dimensions of the scattering volume must be large with respect to both the correlation lengths in the medium and the wavelength of the used light; the scattered light is then the sum of a large number of independent contributions. In a colloidal crystal the Gaussian statistics of the random force causes the Siegert relation to be valid, provided that the displacements of the particles in the crystal are small compared to the wavelength of the light.

5.3. Practice of measuring single modes in colloidal crystals

In section 5.2 we showed that the heterodyne experiment directly measures the first-order correlation function $g_1(\underline{k},\tau)$. When it is assumed that the linear size of the scattering volume is much larger then the lattice parameter the experiment probes light scattered by a single crystal wave with wavevector $\underline{q}$. If we exclude $\underline{k} = \underline{K}_l$ we may write $g_1(\underline{k},\tau)$ as

$$g_1(\underline{k},\tau) \simeq \sum_{\alpha} (k^{\alpha})^2 \, I^{\alpha}_{\underline{q}}(\tau) \quad \text{with} \quad \underline{q} = \underline{k} - \underline{K}_l \quad , \underline{q} \in \text{FBZ}, \tag{5.22}$$

where k^{α} is the component of $\underline{k}$ in the α-direction. The next step is to isolate a single mode, i.e. not only isolation of a single $\underline{q}$ but also of a single polarization direction. Equation 5.22 shows that the weights of the polarizations are proportional to the squares of the projections of the scattering vector $\underline{k}$ on the polarization directions.

Figure 5.2 illustrates the measurement of pure longitudinal modes which is straightforward if the wavevectors $\underline{q}$ point in crystal symmetry directions. Starting point is a horizontal scattering geometry, i.e. beam $\underline{k}_i$ and scattered light vector $\underline{k}_s$ are in the horizontal plane. The BCC crystal has its closest-packed plane, the (110) plane, parallel to the cell walls (Clark *et al.* 1979). The crystal is rotated around the normal on the cell walls and around a vertical axis until Bragg scattering in the horizontal plane is observed (Fig. 5.2a). The detector is now placed as to accept Bragg-scattered light. The next step is rotation of the crystal over an angle θ and of the detector over 2θ around the vertical axis starting from the Bragg-scattering orientation. This leads to a situation where $\underline{k}$ and $\underline{q}$ are parallel and only the longitudinal mode is detected.

Pure transverse modes in symmetry directions of the crystal cannot be probed with a conventional single-beam / single-detector setup. For relatively small $\underline{q}$-vectors, however, transverse modes can dominate the correlation function. The starting point of a transverse mode experiment is the orientation of beam, crystal and detector shown in Fig. 5.2a. To probe transverse modes the cell is rotated around its normal over an angle φ. Figure 5.3 shows a view from behind the cell. The transversal and longitudinal components of the wavevector are $k^T = k \cos \varphi/2$ and $k^L = k \sin \varphi/2$ respectively. For relatively small angles

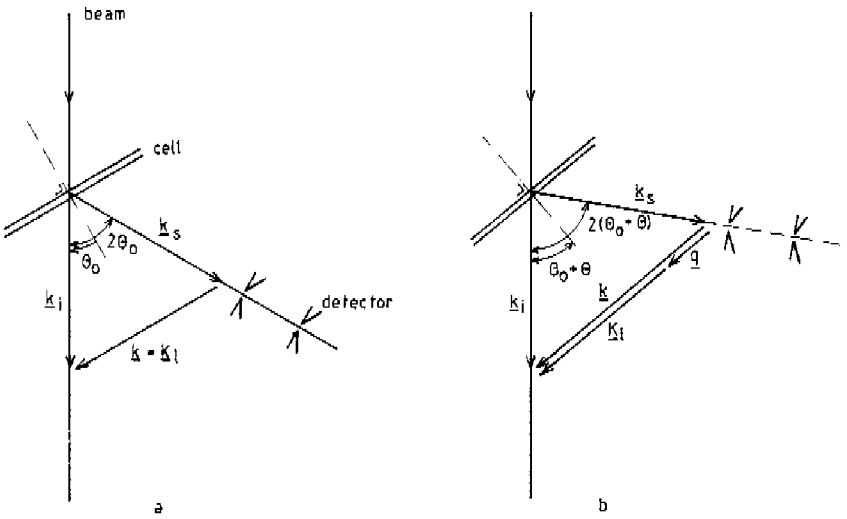

Fig. 5.2 Probing longitudinal modes.
(a) Detection of Bragg-scattered light: $\underline{k} = \underline{K}_l$.
(b) Detection of light scattered by the longitudinal mode with wavevector $\underline{q}$.

$\varphi < 20^0$, the transverse component dominates: $(k^L)^2 < 0.05\ (k^T)^2$. Write $g_1(\underline{k},\tau)$ as follows:

$$g_1(\underline{k},\tau) = W^T\ e^{-(\omega_q^T)^2\tau/\lambda_q^T} + W^L\ e^{-(\omega_q^L)^2\tau/\lambda_q^L}$$

(i.e. a restriction to the slow decay rate of overdamped modes, see Eq. 5.15). The weights of the transverse mode (W^T) and the longitudinal mode (W^L) in the measured correlation function are also gauged by the dynamics of both modes (see Eq. 5.14):

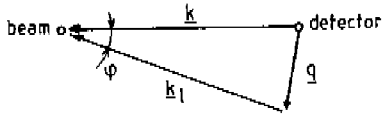

Fig. 5.3 View from behind the scattering cell. For small φ $\underline{k}$ is almost perpendicular to $\underline{q}$: light scattered by the transverse mode with wavevector $\underline{q}$ will dominate the correlation function.

$$W^T = \frac{\pi}{(\omega_q^T)^2}(k^T)^2, \quad W^L = \frac{\pi}{(\omega_q^L)^2}(k^L)^2 . \tag{5.23}$$

The characteristic frequencies ω_q^T and ω_q^L will be of the same order of magnitude.

Suppose that the starting point is a (110) spot (i.e. $\underline{K}_1 = \underline{K}_{110}$, see Fig. 5.3). With the (110) plane parallel to the walls transverse modes with $\underline{q}$ almost in the [100] direction ($\underline{q}$ deviates $\varphi/2$ from the [100] direction) and polarization parallel to the walls are probed. (110) spots appear at $|\underline{K}_{110}| = 2\sqrt{2}\,\pi/R_0$, therefore the [100] transverse mode that is probed when the cell is rotated around an angle φ has wavenumber

$$q_{100} = 4\sqrt{2}\,\pi \sin(\varphi/2) \;/\; R_0$$

or, when we write $Q_{100} = q_{100}\,R_0/4\pi$ ($Q = 0.5$ on the zone boundary): $Q_{100} = \sqrt{2}\,\sin(\varphi/2)$. A φ-range from 0° to 20° gives a Q-range from 0 to 0.25. We can conclude that in this scattering geometry there is quite a large Q-interval for which the correlation function is dominated by the transverse modes.

5.4. Experimental setup

Our dynamic light scattering experiments on colloidal crystals were guided by Hurd *et al.* (1982); for a large part we employed the same techniques and concepts, including the central concept of the thin-film cell in which the crystals are grown. A not unimportant extension of the experiment was the introduction of the heterodyne detector, a light scattering setup in which the local oscillator was guided through a single-mode optical fiber (see section 2.5). This allowed heterodyne experiments to be done with the ease of homodyne experiments. I would like to emphasize that heterodyne scattering is essential when using thin-film cells. Flares of light reflected from glass surfaces always produce heterodyning which can be efficiently put under control by an explicit heterodyne setup.

The use of a thin sample cell had three reasons. The first and main reason was reduction of multiple scattering. The theory of correlation functions (section 5.2) is based on light that is scattered once. Multiple scattering results in averaging over scattering vectors. Because the particle concentration in a colloidal crystal is quite large, the mean-free path of a photon in the colloid is small. Reduction of the pathlengths of scattered light within the sample to lengths typically smaller than the mean-free path of a photon is a condition for well-defined experiments. An estimate for the photon's mean-free path is (Hurd 1981)

$$P = (n\,\sigma\,Q_{sca})^{-1} \tag{5.24}$$

with n the number concentration of the spheres, σ their cross-section and Q_{sca} their scattering efficiency (which can be calculated from Mie theory; Kerker 1969). Our experimental evidence was mainly extracted from crystals consisting of polystyrene spheres in water with particle radius 0.053 μm and lattice parameter 0.8 μm, probed with a HeNe-laser ($\lambda = 0.633$ μm). This gives $P \approx 5$ mm ($Q_{sca} \approx 6\ 10^{-3}$).

The second reason for using a thin cell was its strong influence on the crystal orientation. Dilute colloidal crystals in general have a BCC structure, in the presence of a wall the crystals will orient themselves with the (110) plane parallel to the wall (Clark *et al.* 1979). Therefore the crystal orientation will have only one degree of freedom left: its orientation with respect to the axis

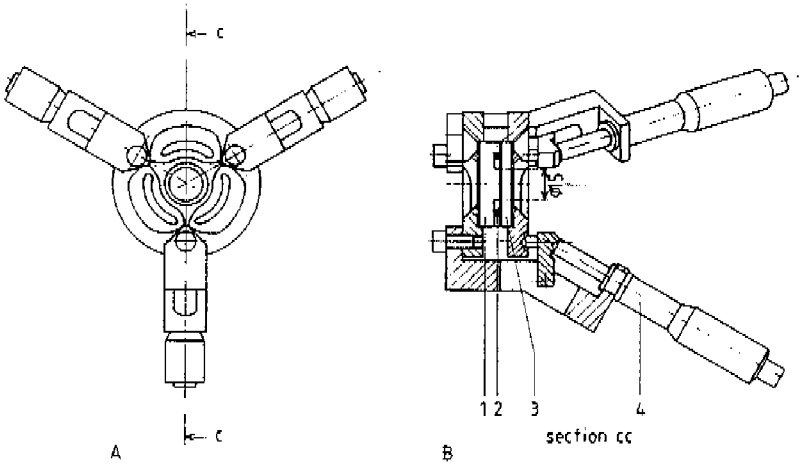

Fig. 5.4 The thin-film sample cell. (a) Front view. (b) Section C–C. The two quartz windows (1 and 3) are held apart by an O ring (2). Three differential micrometer screws (4) settle the mutual position of the windows. The micrometer screws are placed under an angle of about 30° to make the thin film well accesible for the laser beam.

normal to the wall. This simplified identification of Bragg spots emerging from the crystal and allowed a clear definition of the reciprocal lattice. The third reason was the possibility to identify single crystals. Single crystals filled the gap between the two bounding walls. When the cell was probed with white light separate crystals could be identified by the color of the light they scattered in the direction of the observer.

The most important parts of the cell were two quartz windows, separated by a silicone rubber *O* ring (Fig. 5.4). The function of the *O* ring was twofold: it sealed the colloidal crystal reservoir and it served as a spring to allow cell-spacing adjustment. The space within the perimeter of the *O* ring was divided in a (relatively thick) reservoir for ion-exchange resin particles and a 15 mm

diameter thin film. Three differential micrometer screws with an effective pitch of 50 μm were used to settle the mutual position of the quartz plates. The windows outside the O ring perimeter were used for interferometric measurement of the cell spacing, which could be adjusted with an accuracy of 1 μm.

The sample needed to have a low ionic strength in order to obtain dilute crystals. Therefore ionic cleanliness of the parts of the cell in contact with the colloid was very important, particularly for a thin cell which has a large surface to volume ratio. The quartz windows were cleaned with water and soap and with warm sulfochromic acid. Thereafter they were extensively rinsed with deionized and filtered water (resistivity 18 MΩ cm; pore size of the filter 0.22 μm). The silicone O ring was cleaned in an ultrasonic bath and in boiling water.

The colloid was prepared in quartz cuvettes by diluting monodisperse polystyrene latex. After intimate contact with mixed bed ion-exchange resin (amberlite IRN–150, Polysciences inc.) in order to remove extraneous ions from the water, the colloid crystallized spontaneously in the cuvette. The precleaned colloid was injected into the thin cell with a syringe.

Standard use of heterodyne scattering required an extremely stable optical setup. A schematic view is given in Fig. 5.5. The beam and the detector could be translated in vertical direction. Vertical translation of the cell led to a mechanically unstable setup, therefore this degree of freedom was given to the beam. The horizontally polarized beam emerged from a 30 mW HeNe-laser ($\lambda = 0.633$ μm). The beam that entered the cell was vertically polarized (the two right angle prisms P_2 and P_3, see Fig. 5.5, that lifted the beam changed the polarization direction from horizontal to vertical), it was focussed to a waist of about 60 μm in the cell. Part of the beam was coupled into a single-mode polarization preserving optical fiber that provided the local oscillator on the detector. The optical pathlength difference between the local oscillator and the scattered light had to be smaller than the coherence length of the laser (approximately 5 cm). The length of the single-mode fiber was adjusted such that the contrast of the heterodyne correlation function was maximal at a given local oscillator to scattered light intensity ratio. The cell was mounted on a stage with two (horizontal) translational and three rotational degrees of freedom (see Fig. 5.6). The detector could rotate independently of the cell around the

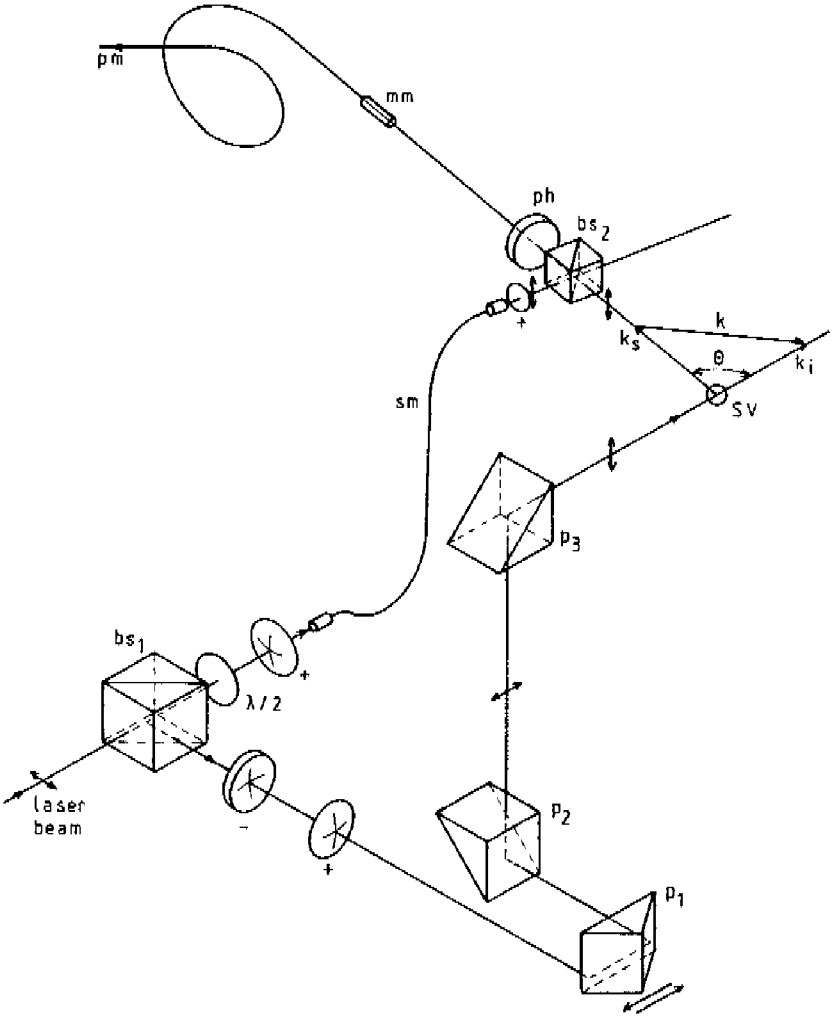

Fig. 5.5 *The optical setup. A horizontally polarized beam emerges from a HeNe laser. Horizontal translation of the right-angle prism P_1 results in vertical translation of the beam that enters the cell. The two right-angle prisms P_2 and P_3 change the polarization direction from horizontal to vertical (polarizations are indicated by the double arrows). The beam enters the scattering volume (sv). Scattered light is mixed with a reference beam that is guided through a single-mode fiber (sm). It passes through a pinhole (ph) and falls on a multimode optical fiber-end (mm) from where it is transported to a photomultiplier (pm).*

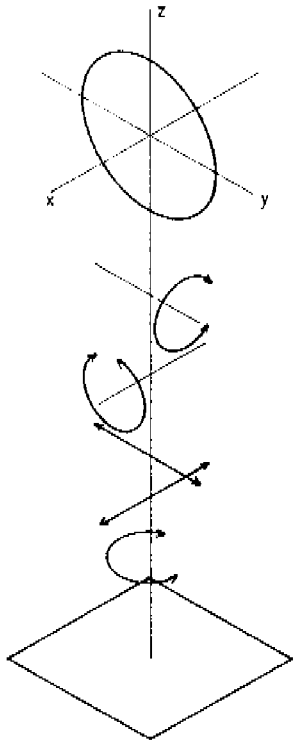

Fig. 5.6 Degrees of freedom of the sample cell. The plane of the cell is represented by the circle. From the bottom (which is fixed to the optical table) to the top the degrees of freedom are: rotation around the z-axis; translation in x- and y-direction; rotation around an axis parallel to the x-axis; rotation around an axis parallel to the y-axis.

same vertical axis as the cell and it could be made to follow the vertical beam displacement with the help of a beam position sensing photodiode mounted on the detector. The detector was equipped with two pinholes with sizes dependent upon the scattered light intensity. The front pinhole had a diameter of 0.1 mm

or 0.3 mm. The back pinhole was in fact formed by the 0.1 mm diameter multimode fiber that transported the scattered light to the photomultiplier. The fiber-end could be partially covered with 0.025 mm or 0.05 mm diameter pinholes. Photon pulses from the cooled photomultiplier were amplified, discriminated and fed into a digital correlator/ structurator (ALV 3000) that computed the correlation function in real time.

5.5. Experimental results

Our main interest was in the behaviour of the wavelength dependent characteristic (complex) frequencies of the damped Brownian motion of colloidal crystals. As was demonstrated in previous sections, overdamped crystal waves give rise to exponential scattered light correlation functions. The decay rate of the correlation function contains the crystal mode damping and eigenfrequency. Experimental results are for a large part condensed into (crystal wave) dispersion functions, i.e. decay rates of scattered light correlation functions as a function of the wavelength.

We prefered a heterodyne to a homodyne setup in light scattering experiments on colloidal crystals. More than in experiments on free Brownian motion there were flares of static light emerging from the cell that gave rise to some heterodyning. If, which was often the case, the intensity of these flares depends on scattering angles, dispersion functions based on homodyne experiments suffer from a systematic error. Of course recognition of this problem is possible (Hurd *et al.* 1982), but often one can not do much about it. In explicit heterodyne experiments the static light intensity exceeds the scattered light intensity by far (we worked with intensity ratios scattered light (including flares) to local oscillator of the order of 1:50) so that ambiguous results are avoided. The effect of partial heterodyning in homodyne experiments is shown in Fig. 5.7a, the squared heterodyne correlation function decays faster than the homodyne correlation function. A least squares fit of a linear combination of the heterodyne and the squared heterodyne function to the homodyne function (Fig. 5.7b) indicates that of the order of 20 % of the detected scattered light was static. The high quality of the fit supports the assumption that the statistics of light scattered by the crystal was Gaussian.

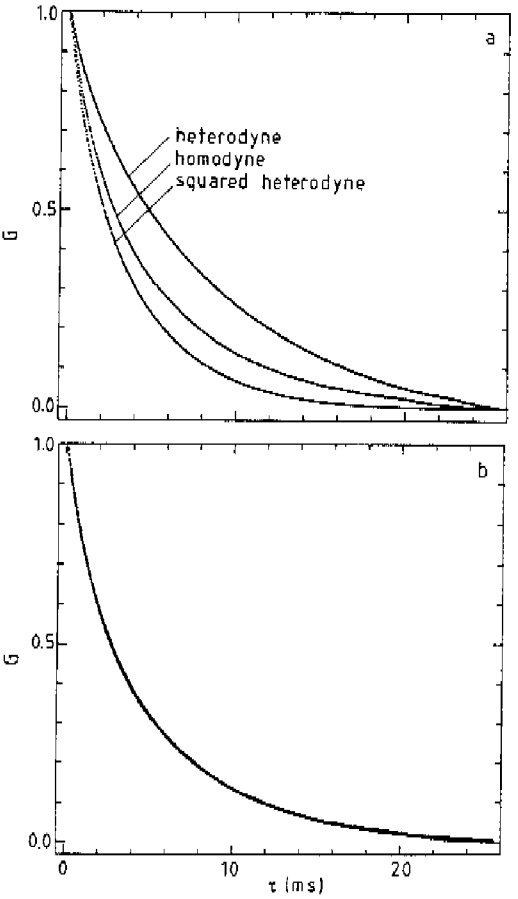

Fig. 5.7 (a) Comparison of the heterodyne, the squared heterodyne and the homodyne correlation function of light scattered from a longitudinal mode in [110] *direction at* Q = 0.14. *The crystal had particle radius* $a = 0.099$ μm, *lattice parameter* $R_0 = 1.8$ μm *and thickness* $L = 43$ μm. *(b) The homodyne correlation has been fitted to* $c_0+c_1G_{het}(\tau)+c_2[G_{het}(\tau)]^2$. *The figure gives both the homodyne function and the fit.* $c_0 = 1.64\ 10^{-3}$, $c_1 = 0.34$, $c_2 = 0.65$. *The curves have been shifted and rescaled in vertical direction.*

The measured dispersion functions presented hereafter originated from a cell filled with colloidal crystal consisting of 0.053 μm radius polystyrene spheres in water. The particle size was measured with heterodyne photoncorrelation spectroscopy of a (very dilute) sample of the particles undergoing free Brownian motion (for details see appendix 2). The lattice parameter varied from 0.80 μm to 0.74 μm, it was stable during the separate dispersion measurement series. Because the lattice parameter is relatively small with respect to the used wavelength (0.633 μm), only (110) Bragg scattering could be used as the starting point of dispersion curves. The cell spacing L ranged from 27 μm to 128 μm. It

appeared that the stability of the crystal orientation, which is important in the course of a dispersion measurement series, was dependent on the cell thickness. Experiments on relatively thick samples sometimes suffered from slight spontaneous rotations of the crystal around an axis normal to the cell.

A qualitative but crucial result from our experiments is that longitudinal mode correlation functions cannot be described by single exponentials, as was predicted by the theory. The dispersion function is formed from the decay rates of correlation functions as a function of the (crystal) wavevector; changing the wavevector was achieved by changing the scattering geometry (which is described in section 5.3, Fig 5.2). However, extracting a single decay rate from longitudinal correlation functions, a typical example of which is shown in Fig. 5.8, was virtually impossible. Nevertheles it was attempted by fitting to a function

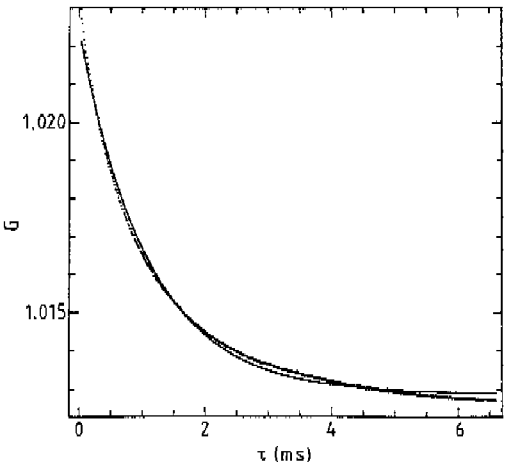

Fig. 5.8 Longitudinal mode photon correlation function (dots) and its least squares single exponential fit (line). q *in* [110] *direction,* Q = 0.11. *The crystal:* $a = 0.053$ μm, $R_0 = 0.80$ μm, $L = 36$ μm.

$$c_1 (1 + k_2 \tau^2) e^{-\Gamma\tau} + c_2 \qquad (5.25)$$

over the time interval $<0\ ,\ 5\Gamma^{-1}]$; where c_1, k_2, Γ and c_2 were the degrees of freedom of the least squares fitting procedure. The longitudinal dispersion curve with $\underline{q}$ in the [110] direction is shown in Fig. 5.9a. It ranges from the zone center (the (110) spot; $Q = 0$) towards the zone boundary ($q = \sqrt{2}\pi/R_0$; $Q = 0.5$).

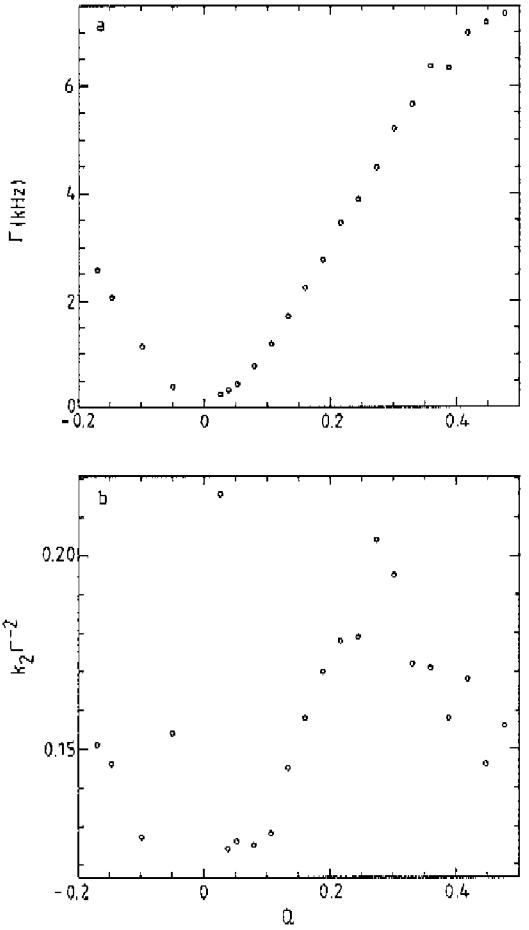

Fig. 5.9 Longitudinal mode dispersion curves. $\underline{q}$ in [110] direction.

The crystal: $a = 0.053$ μm, $R_0 = 0.80$ μm, $L = 36$ μm. $Q = q\ R_0\ \sqrt{2}/4\pi$. The heterodyne correlation functions have been fitted to $c_1(1 + k_2\tau^2)\ e^{-\Gamma\tau} + c_2$ over a time interval $<0{,}5\Gamma^{-1}]$.

(a) Dispersion of the decay rate Γ.

(b) Dispersion of the non-exponentiality. As a measure for non-exponentiality the quantity $k_2\Gamma^{-2}$ was chosen.

Some points at the other side of the zone center demonstrate the crystal symmetry in reciprocal space (this symmetry was also apparent in the cross-correlation experiment described in appendix 3). As a quite arbitrary measure of non-exponentiality we also show the variation of $k_2\Gamma^{-2}$ (Fig 5.9b). The longitudinal dispersion curve in the [110] direction (Fig. 5.9a) was fitted to

$$\Gamma = \frac{(\omega_q^L)^2}{\lambda_q^L} = \frac{1}{6\pi\eta a}\,(8A_1 + 8A_2 + 16B_1/3 + 4B_2)\,\sin^2(\pi Q)\left[1 - \kappa^L_{Y10}(Q)\phi^{1/3}\right],$$

where $\kappa^L_{Y10}(Q)$ is given in polynomial form by Hurd *et al.* (1985). The result is shown in Fig. 5.10, the elastic constant $8A_1 + 8A_2 + 16B_1/3 + 4B_2$ was the only degree of freedom of the fitting procedure.

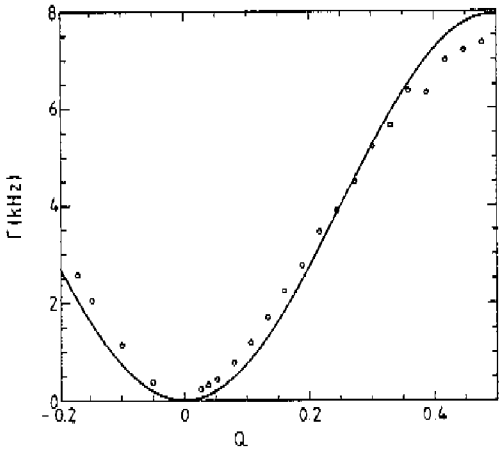

Fig. 5.10 *Fit to the longitudinal mode dispersion curve of Fig. 5.9a. The curve has been fitted to* $\Gamma = c_1/6\pi\eta a\,\sin^2(\pi Q)[1-\kappa^L_{Y10}(Q)\phi^{1/3}]$. *The result is* $c_1 = 1.03\ 10^{-5}\ \mathrm{Nm}^{-1}$.

Transverse mode correlation functions did show, contrary to the longitudinal case, simple exponential behaviour, see Fig. 5.11. Therefore, these measurements could be condensed adequately into dispersion functions. Figure 5.12 shows five transverse mode dispersion curves, all with $\underline{q}$ in [100] direction and polarization parallel to the cell windows, all with a different cell spacing. From Fig. 5.12a to 5.12e the cell thickness decreases. The decay rates Γ were obtained from pure exponential functions ($k_2 \equiv 0$, Eq. 5.25) fitted to the heterodyne photon correlation functions. The least squares fitting procedure extended over the time interval $< 0, 5\Gamma^{-1}]$. The transverse mode correlation functions measured at cell spacing $L = 78\ \mu$m (Fig. 5.12b) were also fitted to functions that contained a second cumulant k_2 (see Eq. 5.25). Results on the dispersion of $k_2\Gamma^{-2}$ are given

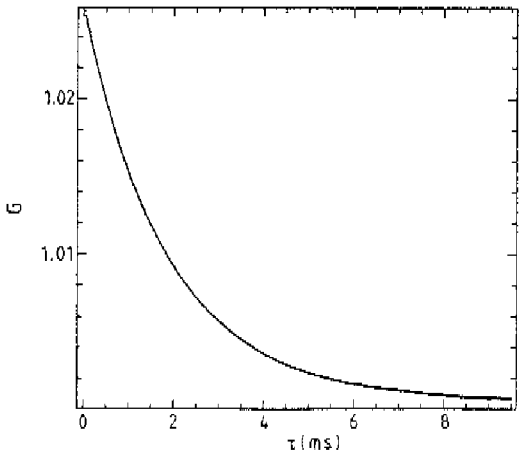

Fig. 5.11 *Transverse mode photon correlation function (dots) and its least squares single exponential fit (line).* $\underline{q}$ *in* [100] *direction,* $Q = 0.06$. *The crystal:* $a = 0.053\ \mu$m, $R_0 = 0.80\ \mu$m, $L = 36\ \mu$m.

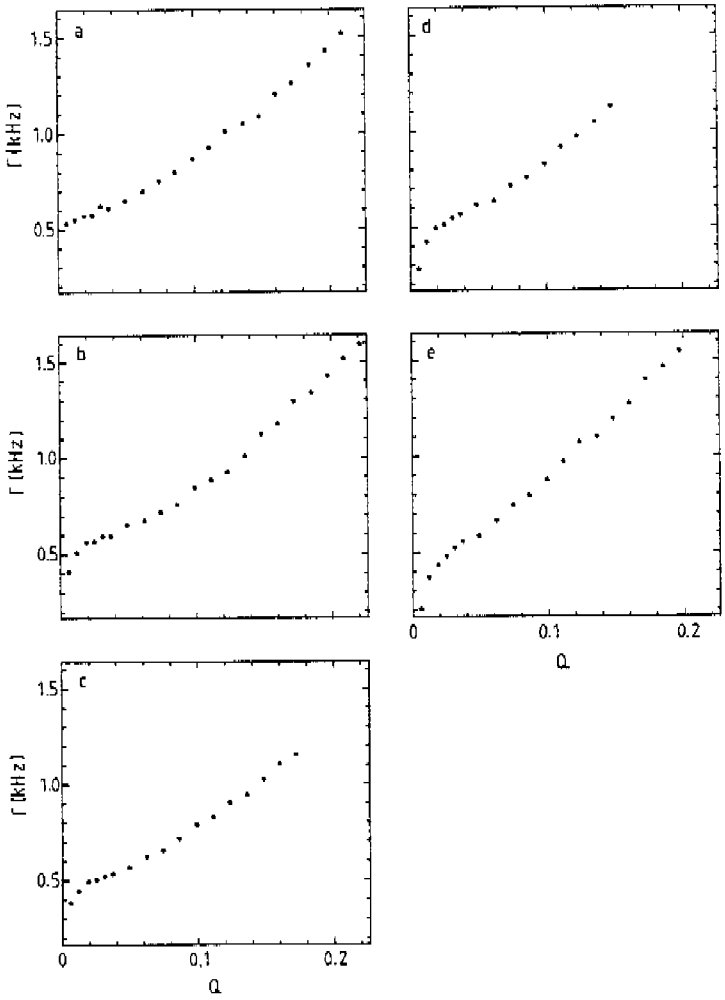

Fig. 5.12 *Transverse mode dispersion curves at various cell thicknesses. Heterodyne correlation functions have been fitted to* $c_1 e^{-\Gamma\tau} + c_2$ *over a time interval* $<0{,}5\Gamma^{-1}]$. $Q = q R_0/4\pi$. *Particle radius* $a = 0.053$ μm.
(a) $L = 128$ μm, $R_0 = 0.74$ μm. *(b)* $L = 78$ μm, $R_0 = 0.76$ μm.
(c) $L = 49$ μm, $R_0 = 0.79$ μm. *(d)* $L = 34$ μm, $R_0 = 0.77$ μm.
(e) $L = 27$ μm, $R_0 = 0.79$ μm.

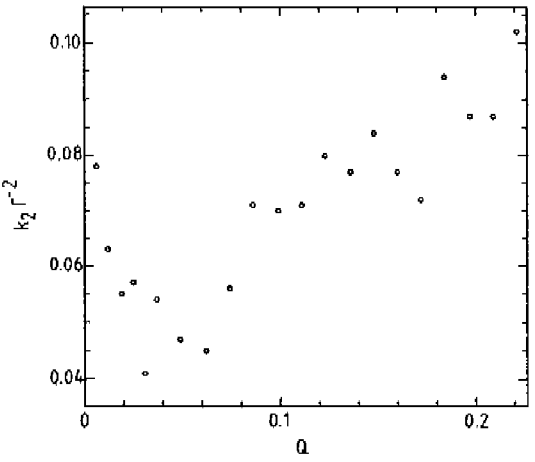

Fig. 5.13 The dispersion of non-exponentiality of transverse mode correlation functions. The correlation functions that constitute Fig. 5.12b have been fitted to $c_1(1 + k_2\tau^2)\, e^{-\Gamma\tau} + c_2$ *over the time interval* $<0,5\Gamma^{-1}]$.

in Fig. 5.13. Comparison with Fig. 5.9b again illustrates the stronger deviation of longitudinal mode correlation functions from single exponential functions. Cell-spacing adjustment caused melting of, or at least severe damage to the crystals. Therefore all five transverse mode dispersion curves (Fig. 5.12) were taken from five different crystals, each with its own lattice parameter and elastic constants. Two features in Fig. 5.12 immediatly attract attention. The first is the finite decay rate at small Q of the transverse modes in Fig. 5.12a, i.e. at the largest cell thickness. This is in accordance with Hurd's theory but in contrast to his experimental findings. The second is the influence of the cell spacing on the shape of the dispersion curves near Q = 0. It seems that the bounding walls have a strong impact on the transverse modes near Q = 0; the thinner the cell, the larger the wall-affected Q-interval.

Figure 5.14 (a and b) shows two fits of the dispersion curves of Fig. 5.12a and 5.12b to the theoretical prediction

$$\Gamma = \frac{1}{6\pi\eta a}\Big[8(A_1 + B_1/3)[1 - \cos(2\pi Q)] + 4A_2 \sin^2(2\pi Q)\Big] \times$$

$$\times\Big[1 - \kappa^{T}_{100}(Q)\phi^{1/3} + \frac{3\,a}{4\pi R_0 Q^2}\Big],$$

where $\kappa^{T}_{100}(Q)$ is given in polynomial form in Hurd *et al* (1985). The only two fitting parameters were the elastic constants $8(A_1 + B_1/3)$ and $4A_2$. A fit with three degrees of freedom to Fig. 5.12a:

$$\Gamma = \frac{1}{6\pi\eta a}\Big[8(A_1 + B_1/3)[1 - \cos(2\pi Q)] + 4A_2\sin^2(2\pi Q)\Big]\Big[1 - \kappa^{T}_{100}(Q)\phi^{1/3} + \frac{C}{Q^2}\Big],$$

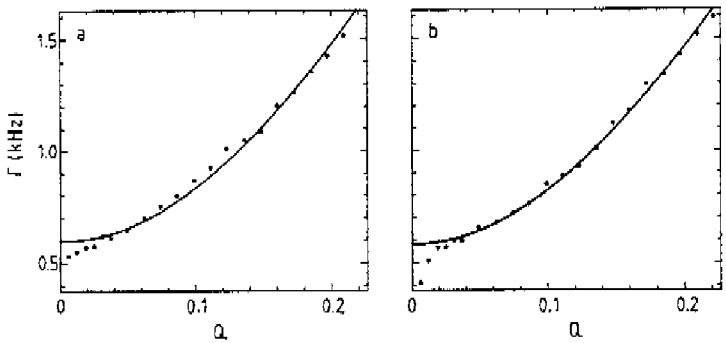

Fig. 5.14 *Fit to two transverse mode dispersion curves. The curves have been fitted to*

$$\Gamma = (6\pi\eta a)^{-1}\Big[c_1[1 - \cos(2\pi Q)] + c_2 \sin^2(2\pi Q)\Big] \times$$

$$\times\Big[1 - \kappa^{T}_{100}(Q)\phi^{1/3} + \frac{3\,a}{4\pi R_0 Q^2}\Big].$$

(a) Fit to Fig. 5.12a, the fit extends over the points 2 to 20.
Result: $c_1 = 1.92\ 10^{-6}$ Nm^{-1}; $c_2 = -7.69\ 10^{-8}$ Nm^{-1}.
(b) Fit to Fig. 5.12b, the fit extends over the points 3 to 21.
Result: $c_1 = 1.87\ 10^{-6}$ Nm^{-1}; $c_2 = -5.32\ 10^{-8}$ Nm^{-1}.

gave $C = 0.016$. The (hydrodynamic) theory predicts $C = 3a/(4\pi R_0) = 0.017$. On the basis of a Debye-Hückel potential ($\psi(r) \simeq e^{-\kappa r}/r$) it follows from Eq. 4.17 with $\kappa R_0 = 3$ that

$$\frac{8(A_1+B_1/3)}{4A_2} = -\frac{2}{3}\, e^{-\kappa r_0}\, e^{\kappa R_0}\, \kappa^2 R_0{}^2\, \frac{1}{r_0/R_0+\kappa r_0} \approx -2.6 .$$

This is in contrast to our experimental results, from the fits of Fig. 5.14 the ratios -25 and -35 are obtained. The elastic constant derived from the longitudinal mode dispersion function is comparable to the elastic constants derived from the transverse mode dispersion functions, although the former dispersion function was obtained on the basis of quite arbitrary assumptions (i.e. the fitting procedure with a second cumulant k_2, Eq. 5.25, has no theoretical basis).

Long-wavelength transverse waves have low damping, see for instance the expression for λ_q^χ that is given immediatly after Eq. 4.30. Therefore the fast mode contained in these waves (see Eq. 5.15, the second term on the right-hand side) should be observable in a dynamic light scattering experiment because its decay rate $\lambda_q^T/\mu_q^T = \eta q^2/\rho$ is (for q small enough) within the reach of photon correlation spectroscopy. This mode is closely connected to the relaxation of shear waves in the fluid (see e.g. Joanny 1979 or Boon & Yip 1980). We indeed observed a fast mode (see Fig. 5.15a) that seems to be uniquely connected with transverse waves, i.e. it is not observed in long-wavelength longitudinal modes as is demonstrated in Fig. 5.15b. Both are homodyne correlation functions. Therefore the observed fast mode was in fact the cross product of the slow and the fast term of Eq. 5.15. Because both decay rates are widely separated the decay rate of the cross product is very close to λ_q^T/μ_q^T. Homodyne measurements were prefered here because they allow detection of high scattered light intensities so that low-noise photon correlation functions could be obtained. A high signal to noise ratio is needed because the relative amplitude of the fast mode is small. The experiments suffered from an inaccurate determination of the length of the crystal wavevector; because the offset angle φ was very small ($\varphi = 0.5^\circ$ to 1.4°, see the geometry of Fig. 5.3), the relative error in q^2 was large (of the order of 20 %). The experiments on the fast modes were performed on a thin crystal ($L = 31\ \mu m$).

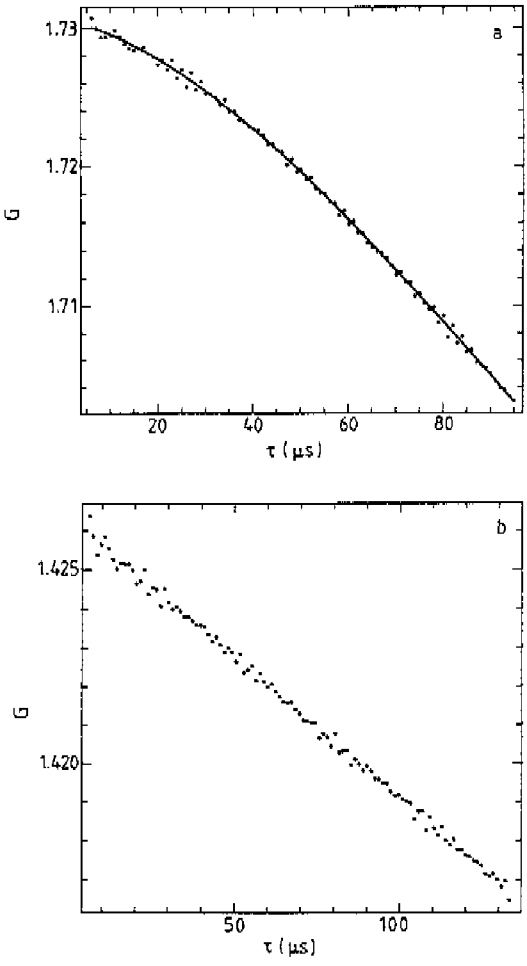

Fig. 5.15 *Small-time homodyne photon correlation functions of long-wavelength modes. The crystal:* $a = 0.053\ \mu m$, $R_0 = 0.67\ \mu m$, $L = 31\ \mu m$. *(a) Transverse mode correlation function with* q *in* [100] *direction.* $Q = 0.0062$. *The solid line represents* $c_1 - \Gamma\tau - c_2 e^{-\Gamma_2 \tau}$ *with* $c_1 = 1.75$, $c_2 = 1.6\ 10^{-2}$, $\Gamma = 440\ s^{-1}$, $\Gamma_2 = 2.3\ 10^4\ s^{-1}$. *(b) Longitudinal mode correlation function with* q *in* [110] *direction.* $Q = 0.013$.

Figure 5.16 shows the dispersion of the fast mode. There are clear deviations from the $\eta q^2/\rho$ -line. They could be manifestations of wall-damping. Therefore we compare them with the behaviour of the transverse mode dispersion functions of the slow mode near $Q = 0$ at comparable sample-cell thicknesses (see Fig. 5.12). Apart from direct observation of the fast mode, λ_q^T/μ_q^T can be

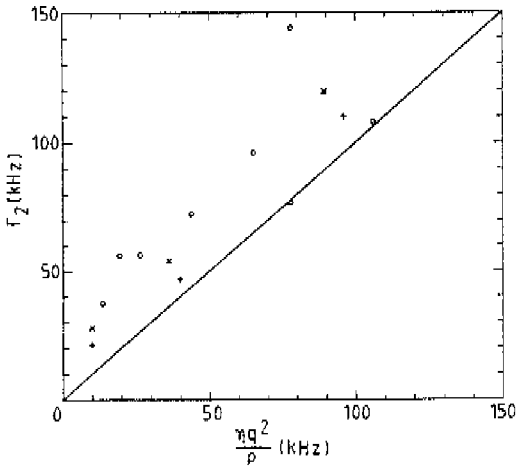

Fig. 5.16 Dispersion of the fast mode of the long-wavelength transverse mode correlation functions (dots). The solid line represents $\eta q^2/\rho$. The x and + represent λ_q^T/μ_q^T calculated on the basis of Figs 5.12d and 5.12e respectively and the elastic constants obtained from the fit of Fig. 5.14b.

estimated on the basis of the slow mode decay rates and the elastic constants (e.g. those that were obtained from the fitting procedure of Fig. 5.14). Results for cell spacings of 34 μm and 27 μm are plotted in Fig. 5.16 (the x's and the +'s). The deviations of the directly observed and the indirectly obtained λ_q^T/μ_q^T from the $\eta q^2/\rho$ -line are of the same order of magnitude. This suggests that also the fast-mode deviations are due to wall effects.

We did not observe underdamped modes. The criterion for modes to be underdamped is:

$$\lambda_q^\alpha < 2\sqrt{\mu_q^\alpha}\,\omega_q^\alpha\,. \tag{5.26}$$

Transverse modes have vanishing damping for $q \to 0$, therefore long-wavelength transverse modes could possibly show oscillatory behaviour. We focus on the [100] direction. For small Q we can write:

$$\lambda_Q^Y = \frac{6\pi\eta a}{m}\left[1 - \kappa_{100}^Y(0)\ \phi^{1/3} + \frac{3a}{4\pi R_0 Q^2}\right]^{-1};$$

$$(\omega_Q^Y)^2 = \frac{8\pi^2}{m} Q^2\ (A_1 + B_1/3 + 2A_2)\ ;$$

$$\mu_Q^Y = m_f/m\ ;$$

We use the numerical values of the experiment of Fig. 5.14a: $R_0 = 0.74\ \mu m$; $a = 0.053\ \mu m$; $8(A_1 + B_1/3) = 1.9\ 10^{-6}\ Nm^{-1}$ and $4A_2 = -7.7\ 10^{-8}\ Nm^{-1}$. The criterion, Eq. 5.26, gives $Q < 2.0\ 10^{-3}$ which corresponds to a phonon wavelength of 0.18 mm. At $Q = 1.0\ 10^{-3}$, $\Omega = 240\ s^{-1}$ (see Eq. 5.14). The first photon correlation function in Fig. 5.12a was taken at $Q = 0.006$.

5.6. Discussion

The discussion on single colloidal crystals and on light scattering techniques in order to probe their dynamics has, especially since the work by Hurd *et al.* (1982), been focussed on a few topics. One that plays a minor role in this thesis is concerned with the description of the electrostatic interaction. The most popular model used in this field is the Debye-Hückel potential interaction which can be derived from the linearized Poisson-Boltzmann equation. At first sight this linearization is not allowed because the condition $Zze^2/(4\pi\epsilon a k_B T) << 1$ is not satisfied (with Z of the order of 10^3 the parameter is of the order of 10^1). However, the elastic constants derived by Hurd *et al.* (1982) from their longitudinal dispersion curves are at least not in contrast to the linear theory. Grüner & Lehmann (1982) argued on the basis of measurements on the dependence of the velocity of sound on the solid state fraction in colloidal crystals that a linear theory is inadequate in describing electrostatic interaction.

Our most reliable experimental evidence on elastic constants was derived from the transverse mode dispersion curves. It deviates significantly from Debye-Hückel theory (see the previous section).

A second point of discussion is whether the Siegert relation for light scattered by Brownian crystal waves is valid or not. In section 5.2 we argued that in the small-amplitude approximation, i.e. if the particle excursions extend over distances that are much smaller than the reciprocal scattering vector, the scattered electric field has Gaussian statistics (which is the key condition for validity of the Siegert relation). Crucial in the argumentation was the assumption of Gaussian statistics of the random driving force of Brownian motion. A comparison between a heterodyne and a homodyne photon correlation function demonstrated the validity of the Siegert relation (see Fig. 5.7).

The damping of long-wavelength transverse modes has been a subject of discussion since Hurd *et al.* (1982) published their dispersion curves. In long transverse waves the particles and the fluid move in concert. Therefore the damping of these waves is determined by the damping mechanism in the fluid itself: its viscosity. Transverse, or shear waves in the fluid have relaxation rates $\eta q^2/\rho$. Hence, the damping of long transverse waves in colloidal crystals should be proportional to q^2. This was not observed in the experiments by Hurd *et al.* (1982). In the first place they did not find propagating modes which should appear if the damping approaches zero. In the second place the decay rate of transverse overdamped modes ($\Gamma = (\omega_q^T)^2/\lambda_q^T$) approached zero instead of a finite value for small q. The latter was to be expected because $\omega_q^T \simeq q$ for small q. This prompted Felderhof & Jones (1987) to extend the dynamics of colloidal crystals with the effects of the finite diffusivity of counter ions in the fluid. Their theory indeed covers the experimental findings on transverse mode dispersion by Hurd *et al.* (1982) but at the same time raises a few questions. In the first place it seems impossible that their theory, which neglects the counter ionic transport by convection, can provide an adequate description of the dynamics of transverse modes (see Fixman 1987). In the second place there is, neither in our experiments, nor in the literature, any evidence on the ionic relaxation rate $D_i\kappa^2$ predicted by the theory.

Another suggestion for explaining the discrepancies between experiment and theory concerning long-wavelength transverse modes has been brought up by Pieranski (1983) and Hurd *et al.* (1985). They pointed out that the walls that

bound the crystal could provide an extra damping mechanism that becomes apparent in regions of reciprocal space with low damping. This suggestion was confirmed by our experiments, see Fig. 5.12; the behaviour of the transverse mode dispersion curves near the zone center depends on the cell thickness. For large enough cell spacings the discrepancy between experiment and theory disappears. Our results suggest that the size of the area in reciprocal space that is affected by the walls is approximately proportional to $1/L$. As a consequence one needs very thick samples to obtain propagating modes. In the previous section (section 5.5) it was pointed out that (in the absense of walls) the q-interval in which transverse modes are underdamped in general is very small. In order to obtain underdamped modes in real (finite size) crystals the sample thickness should be such that the wall affected q-interval is typically smaller than the underdamped-mode q-interval.

Wall effects were also clear in the dispersion of the fast mode with decay rate λ_q^T/μ_q^T . Direct observation in a light scattering experiment of these modes in long transverse waves was possible. The measured decay rates appeared to be higher than the expected $\eta q^2/\rho$, indicating extra (wall) damping. In the next section (section 5.7) I present a preliminary model for the contribution of the bounding walls to the transverse mode damping. Because the wall effects are observed in a region of reciprocal space characterized by coherent motion of fluid and particles the model is based on the relaxation of shear waves in the fluid without taking account of the fluid flow induced by the colloidal spheres moving through the fluid. As a consequence the wall effects should only have one characteristic length: the cell spacing L (and not the sphere radius a or the lattice parameter R_0).

The direct observation of the fast mode in transverse waves also has an indirect consequence. It demonstrates the feasibility of our experimental setup to detect relaxations with decay rates of the order of 10 μs, which is a time scale comparable to the characteristic time of ionic diffusion: $(D_i\kappa^2)^{-1}$. It appears in the theory of Felderhof & Jones (1987) as an approximate root in both the longitudinal and transverse mode characteristic equation (Eq. 4.37). Until now we have not observed it.

An intriguing problem is the difference in shape of correlation functions of light scattered by longitudinal and transverse modes. Although both modes are clearly overdamped the transverse modes behave as simple harmonic oscillators

with one slow (i.e. kHz) relaxation rate while longitudinal modes show strong non-exponential behaviour and therefore seem to incorporate more than one relatively slow relaxation rate. In such a situation the ill condition of the inverse Laplace transform (McWhirter & Pike 1978) is a nuisance; it is impossible to objectively distinguish the characteristic times in the non-exponential correlation function. A few obvious causes for non-exponentiality (e.g. higher-order phonon scattering, non-linear springs between the particles, mixing of light scattered by various modes due to the thin scattering volume, the effect of the bounding walls on crystal dynamics) have in common that they would affect both longitudinal and transverse modes and therefore can be rejected (maybe the transverse modes would be even more affected because they have larger amplitudes and therefore would suffer more from higher-order phonon scattering and/or non-linear springs). Perhaps the solution can be found in the effects caused by the finite-diffusive counter ions in the fluid. The main difference between transverse and longitudinal modes is their motion relative to the fluid. Longitudinal modes are always accompanied by backflow while in long-wavelength transverse modes fluid and particles almost move in phase. Ionic double layers will therefore be more distorted in case of longitudinal modes. The current theory on double-layer effects in colloidal crystals (i.e. Felderhof & Jones 1987) does not predict non-exponential scattered light correlation functions. We have demonstrated, however, that this theory does not give a complete description of the effects of finite-diffusive counter ions in the fluid.

5.7 A tentative model for wall effects in colloidal crystals

Our light scattering experiments on colloidal crystals suggest that the dynamics of long-wavelength transverse modes is influenced by the walls that bound the crystal. In this section I present a provisional theory in order to account for these wall effects. The results of the theory are compared to our experimental findings (i.e. Fig. 5.12).

Wall effects are observed in a region of reciprocal space characterized by coherent motion of fluid and particles. In this region the mode damping is determined by the relaxation of shear waves in the fluid. In an infinite medium

the relaxation rate of the shear modes equals $\eta q^2/\rho$, where q is the length of the mode's wavevector. Now the fluid is confined to a layer with thickness L. Stick boundary conditions are imposed at the planes $z = 0$ and $z = L$. The fluid velocity $\underline{v}(\underline{r},t)$ can then be written as

$$\underline{v}(\underline{r},t) = \sum_{n=1}^{\infty} \int \underline{v}^{(n)}(q_x,q_y,t)\, e^{i(q_x x+q_y y)} dq_x dq_y \sin\frac{n\pi z}{L} . \qquad (5.27)$$

The pressure $p(\underline{r},t)$ is written in a similar way. The equations for fluid flow (i.e. Eqs. 4.1 and 4.2) then read

$$\rho \frac{\partial v_\alpha^{(n)}}{\partial t} = -iq_\alpha p^{(n)} - \eta(q_x^2 + q_y^2 + \frac{n^2\pi^2}{L^2})\, v_\alpha^{(n)} , \qquad (5.28)$$

$$q_x v_x^{(n)} + q_y v_y^{(n)} = 0 \quad \text{and} \quad v_z^{(n)} = 0 , \qquad (5.29)$$

where α equals x or y. This yields $p^{(n)} = 0$ and

$$v_\alpha^{(n)}(q_x,q_y,t) = v_\alpha^{(n)}(q_x,q_y,0)\, e^{-\eta(q_x^2 + q_y^2 + n^2\pi^2/L^2)t/\rho} . \qquad (5.30)$$

The relaxation rate now equals $\eta(q_x^2 + q_y^2 + n^2\pi^2/L^2)/\rho$. If we focus on modes in the [100]-direction (i.e. $q \equiv q_x$) we find a transverse mode damping coefficient of (see Eq. 4.30)

$$\lambda_q^y = \frac{1}{m}\Big[[1 - \kappa_{yy}(q)\phi^{1/3}]/(6\pi\eta a) + \rho/[(q^2+n^2\pi^2/L^2)\eta m_f]\Big]^{-1} . \qquad (5.31)$$

We can write $\kappa_{yy}(q)$ instead of $\kappa_{yy}[\sqrt{q^2 + n^2\pi^2/L^2}\,]$ because the function $[1 - \kappa_{yy}(q)\phi^{1/3}]$ depends only weakly on q for the values of the volume fraction used in the experiment.

The experiments of Fig. 5.12 probe the slow decay rate $(\omega_q^\alpha)^2/\lambda_q^\alpha$ of transverse modes with wavevector and polarization direction parallel to the walls. It is not clear in what way the elastic properties of the crystal are affected by the presence of walls. One could think of the influences of electrostatic interaction between the walls and particles close to the walls. Because of the short-range character of electrostatic interactions we assume these wall effects to be of

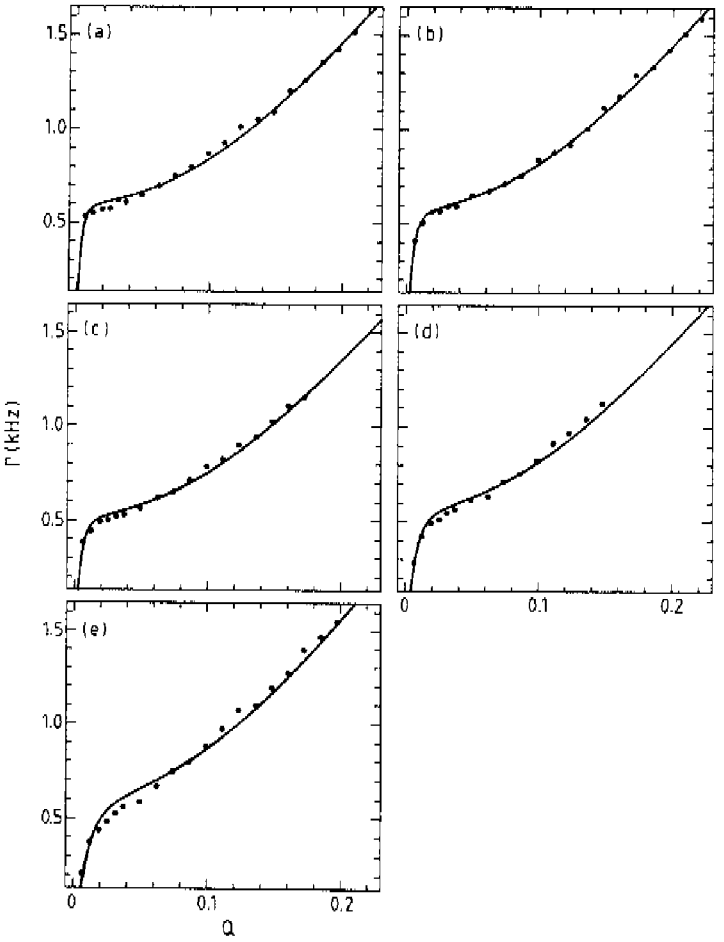

Fig. 5.17 *Fit of the transverse mode dispersion curves of Fig. 5.12 to the prediction on the basis of a model for wall effects (i.e. Eq. 5.33). The results are:* *(a)* $c_1 = 1.8\ 10^{-6}$ Nm^{-1}; C = 2.1 kHz *(b)* $c_1 = 1.8\ 10^{-6}$ Nm^{-1}; C = 5.1 kHz *(c)* $c_1 = 1.7\ 10^{-6}$ Nm^{-1}; C = 4.6 kHz *(d)* $c_1 = 1.8\ 10^{-6}$ Nm^{-1}; C = 13.1 kHz *(e)* $c_1 = 1.9\ 10^{-6}$Nm^{-1}; C = 27.3 kHz.

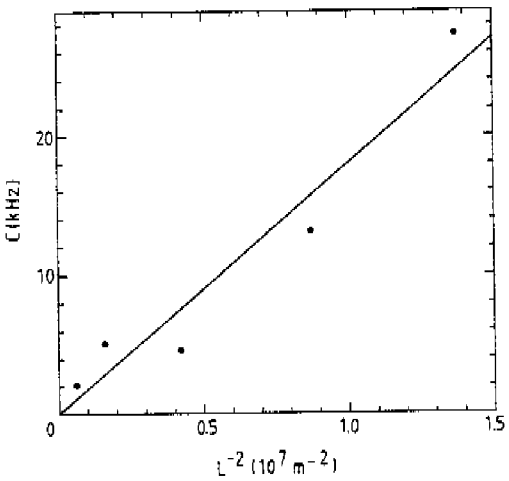

Fig. 5.18 *The wall damping coefficient* C *(see Fig. 5.17 and Eq 5.33) versus* L^{-2}. *The model on wall effects predicts (at mode number* $n = 1$*)* $C = \pi^2\eta/(\rho L^2) = 9.9\ 10^{-6}/L^2$. *The solid line represents a least squares fit. The slope of the line equals* $2.0\ 10^{-5}\ m^2s^{-1}$.

minor importance and use the bulk elastic properties of the crystal in order to calculate the slow decay rate. In the [100]-direction we then have

$$\Gamma = \frac{1}{6\pi\eta a}\Big[8(A_1 + B_1/3)[1 - \cos(2\pi Q)] + 4A_2 \sin^2(2\pi Q)\Big] \times$$

$$\times\Big[1 - \kappa T_{00}(Q)\phi^{1/3} + \frac{3\,a}{4\pi R_0 Q^2 + \pi R_0{}^3 n^2/(4L^2)}\Big], \qquad (5.32)$$

where $Q = qR_0/4\pi$. Note the disputable step that is taken here: the hydrodynamics and the electrostatics employ different mode expansions. Another problem is which number n is selected in the light scattering experiment. A fair choice seems to be $n = 1$ ($n = 0$ is a trivial solution for the

velocity field). Probing a higher order mode would imply a scattering vector not parallel to the walls.

In order to compare theory and experiment we fitted the dispersion curves of Fig. 5.12 to

$$\Gamma = \frac{1}{6\pi\eta a} c_{\perp}[1-\cos(2\pi Q)]\times\left[1-\kappa^{T}_{00}(Q)\phi^{1/3}+\frac{3\,a}{4\pi R_0 Q^2 + R_0{}^3 C\rho/(4\pi\eta)}\right] \quad (5.33)$$

(we dropped the elastic constant $4A_2$ which seems to be of less importance; see e.g. Fig. 5.14). Results are shown in Fig. 5.17. Figure 5.18 shows C versus L^{-2}. The linear relationship between both variables is quite clearly observed. The slope of the line fitted to the points of Fig. 5.18 is, however, approximately twice the slope predicted by the theory.

An alternative approach of wall effects in colloidal crystals may be based on the continuum model of Joanny (1979) applied in a narrow slit. In that case we have to impose stick boundary conditions for both fluid and particles at the cell walls. The stick boundary condition for the particles is not obvious because the lattice plane closest to a wall will be separated from the wall by a fluid layer. The continuum approach, however, cannot cope with more subtle boundary conditions. The consequence is that not only in the hydrodynamic part of Γ but also in the elastic part q needs to be replaced by $\sqrt{q^2 + n^2\pi^2/L^2}$ (cf. Eq. 5.32). This would, in contrast to our experimental findings, leave us with a finite decay rate Γ at $q = 0$, just as in the theory for unbounded crystals.

From the remark on Joanny's theory and from the reservations made in our model it is clear that a full description of wall effects at long-wavelength transverse modes is not yet available.

1. Free Brownian motion of charged spheres in a low ionic strength fluid

In section 4.4 ionic friction was introduced. When a charged colloidal particle moves through water the counter ionic layer which surrounds the particle exerts a drag force on the particle. This phenomenon has been observed in a dynamic light scattering experiment on charged colloidal particles undergoing free Brownian motion (Schumacher & Van de Ven 1987): the diffusion constant of the particles appeared to be dependent on the counter ion concentration in the fluid. Because ionic friction may be of importance for colloidal crystal dynamics we did some experiments on the diffusion of colloidal particles in a fluid with a low ionic strength, i.e. with small counter ion concentration. The results are presented in this appendix.

The experiments by Schumacher & Van de Ven (1987) were guided by a theory of Ohshima *et al.* (1984). For $\kappa a << 1$, i.e. the ionic double layer radius κ^{-1} is much larger than the particle radius a, the reduction of the diffusion constant due to ionic friction is linear in κa . In the simple case of one type of counter ions with valence $z = 1$ and diffusion constant D_i one can conclude from the theory in Ohshima *et al.* (1984):

$$\frac{D}{D_0} = 1 - \frac{Z^2 e^2 \kappa a}{144\pi^2 \eta D_i \epsilon a^2}, \qquad \text{(a1.1)}$$

where D is the diffusion constant of the colloidal particles in the low ionic strength fluid, D_0 is the diffusion constant in the absense of ionic friction (i.e. the Stokes diffusion constant $k_B T/6\pi\eta a$). Equation a1.1 is in accordance with the expression for ionic friction by Felderhof & Jones (1987). They derived an ionic friction coefficient $\zeta_e(\omega)$, Eq. 4.33. For $\omega \to 0$ (the sedimentation limit):

$$\zeta_e(0) = \frac{\kappa Z^2 e^2}{24\pi D_i \epsilon}. \qquad \text{(a1.2)}$$

If $\zeta_e(0) << 6\pi\eta a$ the diffusion constant of the particles becomes

$$D = D_0(1 - \zeta_e(0)/6\pi\eta a), \qquad \text{(a1.3)}$$

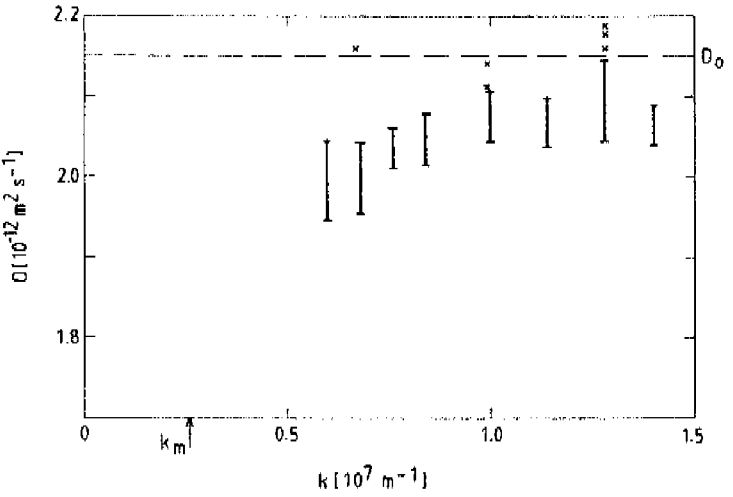

Fig. a1.1 Diffusion constant D versus the length of the scattering vector k *for spheres with radius* $a = 0.099$ μm *at number concentration* $n = 7\ 10^{15}$ m^{-3} *in low ionic strength water of* 20 °C. *The Stokes diffusion constant* $k_B T/6\pi\eta a$ *equals* $2.15\ 10^{-9}$ $m^2 s^{-1}$, *it is represented by the dashed line. The* x*'s represent the experiment on Stokes diffusion (see section 2.5).*

which is equivalent to Eq. a1.1.

We probed a dilute sample of polystyrene spheres in water (radius $a = 0.099$ μm, number concentration $n = 7\ 10^{16}$ m^{-3}). The sample cell contained some ion-exchange resin in order to remove extraneous ions from the water. Over a range of scattering angles heterodyne photoncorrelation functions were measured. The scattering vectors were larger than the characteristic wavenumber of the suspension $k_m = 2\pi(n)^{1/3} \approx 2.6\ 10^6$ m^{-1}. Therefore the experiment probed the diffusion constant D of single particles, although there might have been direct particle interactions in the sample due to the low ionic concentration (Pusey & Tough 1985). The correlation functions could be very

well fitted to single exponentials. Diffusion constants were calculated from the decay rate of the exponential functions (Γ) and the length of the scattering vectors (k) (see Eq. 2.15):

$$D = \Gamma/k^2 .$$

Figure a1.1 shows the results. The diffusion constant slightly depends on the scattering vector indicating some particle interaction. A comparison to the experiment of section 2.5, where the same particles were probed, shows that the diffusion constant D in the low ionic strength fluid lies about 4 % below the value obtained in the absense of ionic friction. On the basis of this observation and Eq. a1.1 we can estimate the fluid's ionic strength. We take $D_i \approx 7\ 10^{-9}\ m^2s^{-1}$, then $Z^2\kappa a \approx 10^5$. If Z is of the order of 10^3 (Pieranski 1983), the Debye-length $\kappa^{-1} \approx 1\ \mu m$ (for comparison: the average particle distance $n^{-1/3} \approx 2.4\ \mu m$). A Debye-length of 1 μm corresponds to a counter-ionic concentration of $1.2\ 10^{20}\ m^{-3}$. This seems to be consitent with $nZ \approx 7\ 10^{19}\ m^{-3}$

2. Determination of the size of the colloidal crystal particles

To compare the results of the dispersion measurements in colloidal crystals to the hydrodynamic theory it is important to know the size of the colloidal crystal particles. Heterodyne photoncorrelation spectroscopy is an excellent tool for particle sizing, as we already saw in section 2.5. A sample cell was filled with a dilute suspension of the same spherical particles that were used to make the colloidal crystals whose phonon dispersion curves are shown in the Figs. 5.9, 5.12 and 5.16. The volume fraction of the spheres in water was $\phi = 5\ 10^{-5}$. The sample temperature was 20 °C. Figure a2.1 shows the results: the decay rates Γ of the exponential correlation functions are proportional to the squared length of the scattering vectors. The slope of the line equals the diffusion constant (Eq. 2.15): $D = 4.07\ 10^{-12}\ m^2s^{-1}$. With $D = k_BT/6\pi\eta a$ it follows that $a = 0.053\ \mu m$.

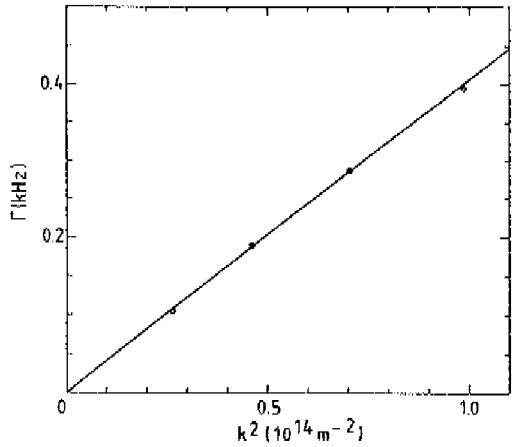

Fig. a2.1 Sizing the colloidal crystal particles. The heterodyne photon correlation function decay rate Γ versus k^2. The slope of the line equals the diffusion constant: $D = 4.07\ 10^{-12}\ m^2s^{-1}$.

3. Cross correlations in colloidal crystals

The theory on light scattering off colloidal crystals suggests that a single phonon scatters light in specific directions with wavevectors that are separated by reciprocal lattice vectors (Eq. 5.12). This is expressed in the symmetry of phonon dispersion curves around Brillouin zone centers and boundaries, see for instance the dispersion curves in Hurd *et al.* (1982) and Fig. 5.9. The dispersion curves, however, just show a time-averaged symmetry. The statement made by the theory is stronger. It says that there is instantaneous symmetry, i.e. the light scattered in directions separated by a reciprocal lattice vector is mutually coherent. In this appendix we describe a cross-correlation experiment which studies this mutual coherence of light scattered off a colloidal crystal in two separate directions.

We introduce a light scattering experiment with two scattering vectors $\underline{k}_1$ and $\underline{k}_2$. The electric field cross-correlation function reads

$$g_1(\underline{k}_1,\underline{k}_2,\tau) = \sum_{i,j} E_1^*(\underline{R}_i)\, E_2(\underline{R}_j)\, e^{-i\underline{k}_1.\underline{R}_i}\, e^{i\underline{k}_2.\underline{R}_j} < e^{-i\underline{k}_1.\underline{s}_i(0)}\, e^{i\underline{k}_2.\underline{s}_j(\tau)} > . \quad (a3.1)$$

The procedure that led to Eq. 5.12 is employed to rewrite Eq. a3.1 in terms of normal mode amplitude correlations. With a restriction to the time-dependent part of $g_1(\underline{k}_1,\underline{k}_2,\tau)$ the result is

$$g_1(\underline{k}_1,\underline{k}_2,\tau) \simeq \sum_{l_1 l_2} \sum_{\underline{q}} \left[P_1^*(\underline{k}_1 - \underline{q} - \underline{K}_{l_1})\, P_2(\underline{k}_2 - \underline{q} - \underline{K}_{l_2}) \sum_{\alpha} C_{\underline{q}}^{\alpha}\, k_1^{\alpha}\, k_2^{\alpha}\, I_{\underline{q}}^{\alpha}(\tau) \right], \quad (a3.2)$$

where $P_m(\underline{q})$ (m = 1, 2) is the spatial Fourier transform of the scattering volume profile function $E_m(\underline{r})$. The function $I_{\underline{q}}^{\alpha}(\tau)$ is expressed in Eq. 5.13. If $\underline{k}_1 = \underline{k}_2$ the autocorrelation result is obtained. In that case $l_1 = l_2$ because $\underline{q}$ is confined to the FBZ. The cross-correlation function $g_1(\underline{k}_1,\underline{k}_2,\tau)$ is non zero if $\underline{k}_1 - \underline{k}_2 \approx \underline{K}_{l_1} - \underline{K}_{l_2}$. This means that the two scattered light signals are correlated if $\underline{k}_1$ and $\underline{k}_2$ are oriented such that their difference approximately equals a reciprocal lattice vector. The time dependence of the cross-correlation function is represented by $I_{\underline{q}}^{\alpha}(\tau)$. The width of the functions $P_1(\underline{q})$ and $P_2(\underline{q})$ determines the size of the interval of $\underline{k}_1 - \underline{k}_2$ for which cross correlation can be

observed; the wider the functions $P_1(\underline{q})$ and $P_2(\underline{q})$ (i.e. the smaller the scattering volume) the more deviation of $\underline{k}_1 - \underline{k}_2$ from $\underline{K}_{1_1} - \underline{K}_{1_2}$ can be tolerated. If the scattering volume has a linear size d, the width of $P_1(\underline{q})$ and $P_2(\underline{q})$ is of the order of $1/d$. The detectors then have to be aligned with a scattering angle accuracy of $\Delta\theta \approx \lambda/(2\pi d)$ in order to observe cross correlation. In our setup the accuracy that can be reached is approximately $0.2°$, therefore the linear size of the scattering volume will have to be of the order of 30 μm.

Starting point of the experiment was detection of Bragg diffraction (see Fig. a3.1a). One detector was placed as to accept Bragg scattered light, the other was placed in the beam. The difference between the two scattering vectors

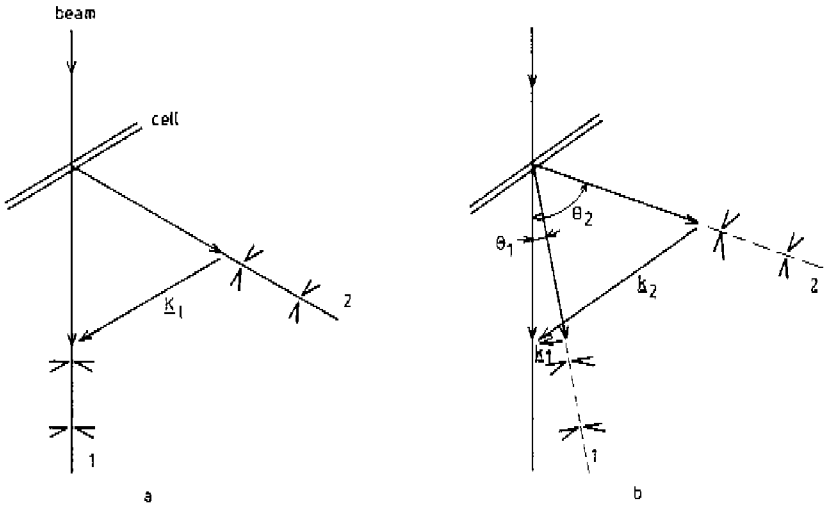

Fig. a3.1 *Cross-correlation light scattering geometry. (a) in the initial position there is Bragg diffraction. This allows us to align the detectors such that the scattering vectors are a reciprocal lattice vector apart. (b) the setup (cell and detectors) is rotated over an angle θ_1. This is the geometry in which cross-correlation functions are measured.*

thus equaled a reciprocal lattice vector. Next the cell and the two detectors were rotated over an angle θ_1 around a vertical axis (Fig. a3.1b). Scattered light was detected and a homodyne photon cross-correlation function was measured. It is assumed that the Siegert relation is valid (see section 5.2 and Dhont & De Kruif 1983), i.e. intensity correlation functions can be calculated from field correlation functions.

The experiment was done on a $L = 31$ μm thick crystal of $a = 0.053$ μm polystyrene spheres with lattice parameter $R_0 = 0.71$ μm. The beam diameter in the cell was approximately 40 μm. Starting point was (110) Bragg scattering. For practical reasons we had to restrict θ_1 to small values. In our setup the vertical axis did not cross exactly the scattering volume, therefore rotation led to a displacement of the scattering volume. If the cell was rotated over an angle that is too large the scattering volume moved out of the cones defined by the collecting optics and no scattered light was detected.

Figure a3.2 shows a result for $\theta_1 = 2.5^\circ$; the direction of rotation is indicated in Fig. a3.1b. Figures a3.2a and a3.2b are both autocorrelations. Notice that the contrast in a3.2a is smaller than in a3.2b. The first autocorrelation function originated from detector 1 which was close to the beam where there probably was much static stray light. This led to partial heterodyning of the autocorrelation function. Figure a3.2b was from the detector close to the (110) Bragg scattering direction (detector 2). Figure a3.2c shows the cross-correlation function $<I_1(0)\ I_2(\tau)>$, the mutual coherence of light scattered towards detector 1 and detector 2 is clearly observed. The low contrast of the cross-correlation function is probably due to a slight mismatch of the scattering vectors with respect to the reciprocal lattice. The time scales of all three correlations are close to one another. Their mutual differences are explained by the effects of partial heterodyning.

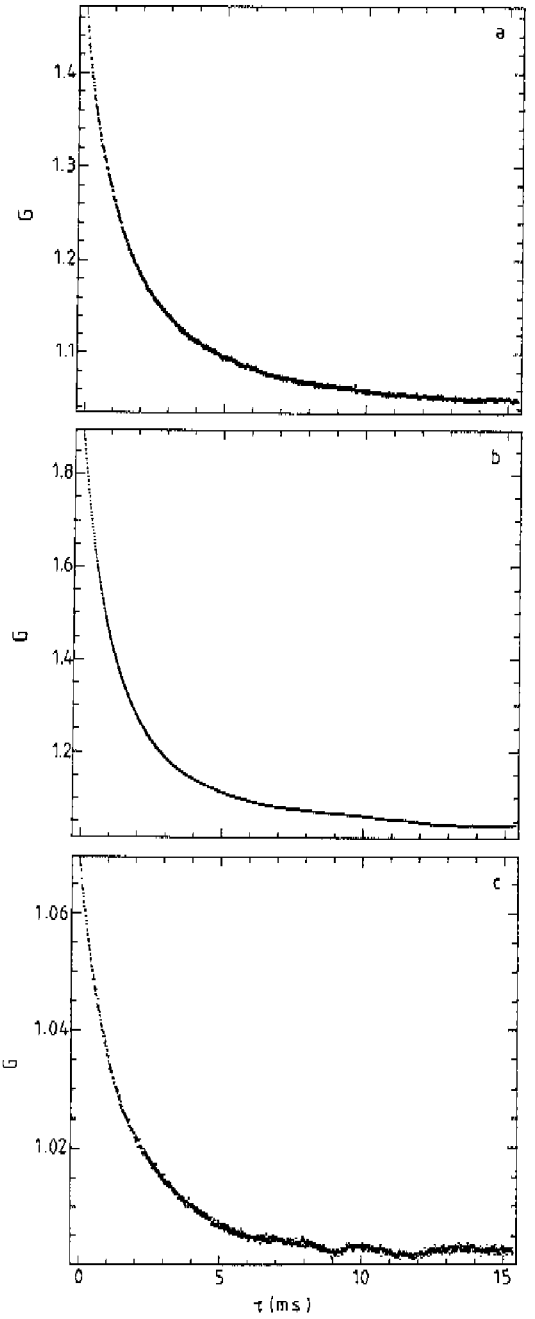

Fig. aS.2 *Results of a homodyne cross-correlation experiment. The crystal was probed with a* $\lambda = 0.633$ μm *laser beam. The difference between the two scattering vectors* $\underline{k}_1$ *and* $\underline{k}_2$ *approximately equaled the vector between the origin and the* (110) *point of the reciprocal lattice. The two scattering angles were* $\theta_1 = 2.5°$; $\theta_2 = 80.5°$. *(a) and (b) show the normalized autocorrelation functions* $\langle I_1(0)\, I_1(\tau)\rangle / \langle I_1\rangle^2$ *and* $\langle I_2(0)\, I_2(\tau)\rangle / \langle I_2\rangle^2$ *respectively. (c) shows the cross-correlation function* $\langle I_1(0)\, I_2(\tau)\rangle / [\langle I_1\rangle\, \langle I_2\rangle]$.

References

B.J. Ackerson & N.A. Clark, J. Physique 42, 929 (1981).

J.P. Boon & S. Yip, *Molecular Hydrodynamics* (McGraw-Hill, London, 1980).

S. Chandrasekhar, Rev. Mod. Phys. 15, 1 (1943).

N.A. Clark, A.J. Hurd & B.J. Ackerson, Nature (London) 281, 57 (1979).

W. Cochran, *The Dynamics of Atoms in Crystals* (Edward Arnold, London, 1973).

J.K.G. Dhont & C.G. de Kruif, J. Chem. Phys. 79, 1658 (1983).

A. Einstein, Ann. Phys. 17, 549 (1905).

B.U. Felderhof & R.B. Jones, Z. Phys. B 64, 393 (1986).

B.U. Felderhof & R.B. Jones, Faraday Discuss. Chem. Soc. 83, 69 (1987).

M. Fixman, Faraday Discuss. Chem. Soc. 83, 106 (General Discussion) (1987).

R.T. Foister & T.G.M. van de Ven, J. Fluid Mech. 96, 105 (1980).

G.G. Fuller, J.M. Rallison, R.L. Schmidt & L.G. Leal, J. Fluid Mech. 100, 555 (1980).

C.W. Gardiner, *Handbook of Stochastic Methods* (Springer, Berlin, 1983).

F. Grüner & W.P. Lehmann, J. Phys. A 15, 2847 (1982).

R. Hanbury-Brown & R.Q. Twiss, Nature 177, 27 (1956).

J. Happel & H. Brenner, *Low Reynolds number hydrodynamics*, second edition (Noordhoff, Leiden, 1973).

H. Hasimoto, J. Fluid Mech. 5, 317 (1959).

A.J. Hurd, R.C. Mockler & W.J. O'Sullivan, *4th International Conference on Photon Correlation Techniques in Fluid Dynamics*, edited by W.T. Mayo & A.E. Smart (Stanford University, Stanford, 1980).

A.J. Hurd, Ph.D. thesis, University of Colorado, Boulder, Colorado, 1981 (unpublished).

A.J. Hurd, N.A. Clark, R.C. Mockler & W.J. O'Sullivan, Phys. Rev. A 26, 2869 (1982).

A.J. Hurd, N.A. Clark, R.C. Mockler & W.J. O'Sullivan, J. Fluid Mech. 153, 401 (1985).

E. Jakeman & E.R. Pike, J. Phys. A 2, 411 (1969).

E. Jakeman, C.J. Oliver & E.R. Pike, J. Phys. A 3, L45 (1970).

E. Jakeman, *Photon Correlation and Light Beating Spectroscopy*, edited by H.Z. Cummins & E.R. Pike (Plenum, New York, 1974).

J.F. Joanny, J. Colloid Interface Sci. 71, 622 (1979).

M. Kerker, *The Scattering of Light* (Academic Press, New York, 1969).

C. Keveloh & W. Staude, Applied Optics 22, 333 (1983).

C. Kittel, *Introduction to Solid State Physics*, fourth edition (John Wiley & Sons, New York, 1971).

A. Kose, M. Ozaki, K. Takano, Y. Kobayashi & S. Hachisu, J. Colloid Interface Sci. 44, 330 (1973).

H.M. Lindsay & P.M. Chaikin, J. Chem. Phys. 76, 3774 (1982).

D. Marcuse, *Light Transmission Optics*, second edition (Van Nostrand Reinhold, New York, 1982).

P. Mazur & D. Bedeaux, Physica 76, 235 (1974).

J.G. McWhirter & E.R. Pike, J. Phys. A 11, 1729 (1978).

W.J. Moore, *Physical Chemistry* (Prentice-Hall, Englewood Cliffs, New Jersey, 1972).

H. Ohshima, T.W. Healy, L.R. White & R.W. O'Brien, J. Chem. Soc., Faraday Trans. 2 80, 1299 (1984).

P. Pieranski, Contemp. Phys. 24, 25 (1983).

P.N. Pusey & R.J.A. Tough, *Dynamic Light Scattering*, edited by R. Pecora (Plenum, New York, 1985).

P.N. Pusey & W. van Megen, Physica A 157, 705 (1989).

P.G. Saffman, Stud. Appl. Math. 52, 115 (1973).

M. San Miguel & J.M. Sancho, Physica 99A, 357 (1979).

K. Schätzel, Appl. Phys. B 42, 193 (1987).

G.A. Schumacher & T.G.M. van de Ven, Faraday Discuss. Chem. Soc. 83, 75 (1987).

M.C. Wang & G.E. Uhlenbeck, Rev. Mod. Phys. 17, 323 (1945).

D.H. van Winkle & C.A. Murray, Phys. Rev. A 34, 562 (1986).

a	particle radius	m
$\underline{a}_q$	normal mode amplitude	m
A_1, A_2, B_1, B_2	elastic constants	N m^{-1}
$A_{qq}^{\alpha\beta}(\tau)$	crystal mode correlation function	m^2
$B(\underline{k},\tau)$	spatial Fourier transform of $P(\underline{r},\tau)$	–
c	speed of light (3.00 10^8 m s^{-1})	
c_0, c_1, c_2	least squares fit parameters	
C_1, C_2, C_3, C_4	transverse mode equation parameters	s^{-1},s^{-2},s^{-3},s^{-1}
d	linear size of the scattering volume	m
$\underline{d}$	position on sphere surface	m
D	diffusion constant	m^{2}s^{-1}
D	potential tensor	N m^{-1}
e	elementary charge (1.60 10^{-19} C)	
e_s	scattered electric field component	V m^{-1}
$\underline{e}$	unit vector	–
E	electric field amplitude	V m^{-1}
$E_0[\underline{r}]$	electric field amplitude distribution	V m^{-1}
$\underline{f}_j$, $\underline{f}_q$	drag force density	N m^{-3}
$\underline{F}_j$	elastic interaction force	N
$g_1(\underline{k},\tau)$	field correlation $<E^*(\underline{k},0)\, E(\underline{k},\tau)>$	V^{2}m^{-2}
$g_1(\underline{k}_1,\underline{k}_2,\tau)$	cross correlation $<E^*(\underline{k}_1,0)\, E(\underline{k}_2,\tau)>$	V^{2}m^{-2}
$g_2(\underline{k},\tau)$	4th order field correlation function	V^{4}m^{-4}
$G(j\tau_s)$	normalized photon correlation function	–
$G_{het}(\tau)$	heterodyne correlation function	W^{2}m^{-4}
$G_{hom}(\tau)$	homodyne correlation function	W^{2}m^{-4}
$G^{(1)}(\tau)$	normalized heterodyne correlation function	–
$G^{(2)}(\tau)$	normalized homodyne correlation function	–
$\underline{G}_j$	ionic friction force	N
$h_1(\underline{k},\tau)$	field correlation $<E(\underline{k},0)\, E(\underline{k},\tau)>$	V^{2}m^{-2}
$\underline{H}_j, \underline{H}_q$	dipole interaction force	N

I	intensity	$W\ m^{-2}$
$\mathbf{I}$	unit tensor	–
$I_q^{\alpha}(\tau)$	correlation function integral	s^3
k_B	Boltzmann constant ($1.38\ 10^{-23}$ J K^{-1})	
k_2	second cumulant	s^{-2}
$\underline{k}$	scattering vector	m^{-1}
$\underline{k}_i$	incident wave vector	m^{-1}
$\underline{k}_s$	scattered light vector	m^{-1}
$\underline{K}_l$	reciprocal lattice point	m^{-1}
L	sample cell thickness	m
m	mass	kg
m_f	mass of fluid in a unit cell	kg
n	refractive index	–
n	number concentration	m^{-3}
n_0	counter ion density	m^{-3}
n_i	number of photon counts in sample i	–
N	number	–
p	pressure	Pa
$\underline{p}_j$, $\underline{p}_q$	dipole strength	C m
$P(\underline{r},t)$	probability density	m^{-3}
$P(\underline{q})$	spatial Fourier transform of $E_0[\underline{r}]$	V m^2
P	mean free path of a photon	m
$\underline{q}$	phonon wave vector	m^{-1}
Q	normalized component of $\underline{q}$	–
Q_{sca}	scattering efficiency	–
$\underline{Q}_l$	$\underline{q} - \underline{K}_l$	m^{-1}
$\underline{r}$	position vector	m
$\underline{r}_j$	position of particle j	m
$\tilde{\underline{r}}$	stochastic part of particle motion	m
$\underline{R}$	position at detector surface	m
$\underline{R}_j$	lattice point	m
R_0	lattice parameter	m
r_0	$\sqrt{3}\ R_0/2$	m
$\mathbf{S}(\underline{q})$	part of hydrodynamic interaction tensor	$N^{-1}m\ s^{-1}$

$\underline{s}_j$	position relative to $\underline{R}_j$	m
t	time	s
T	temperature	K
$\mathbf{t}(\underline{q},\omega)$	Oseen tensor in reciprocal space	$N^{-1}m^4s^{-1}$
T	hydrodynamic interaction tensor	$N^{-1}m\ s^{-1}$
$\underline{u}_j$	particle velocity	$m\ s^{-1}$
U	dipole interaction tensor	m^{-3}
V	scattering volume	m^3
$\underline{v}$	fluid velocity	$m\ s^{-1}$
v_c	volume of a unit cell	m^3
W	weight factor	–
x,y,z	Cartesian coordinates	m
$\underline{X}_j$, $\underline{X}_q$	random force	N
$\mathbf{Y}(\underline{q},\omega)$	part of hydrodynamic interaction tensor	$N^{-1}m\ s^{-1}$
z	valence of counter ions	–
Z	valence of a colloidal particle	–
α	$\sqrt{-i\omega\rho/\eta}$	m^{-1}
β	inverse velocity autocorrelation time	s^{-1}
γ	shear rate	s^{-1}
Γ	decay rate	s^{-1}
δ	opening angle of detector	–
ϵ_0	dielectric constant of vacuum ($8.85\ 10^{-12}\ N^{-1}m^{-2}C^2$)	
ϵ	dielectric constant ($\epsilon = \epsilon_0\ \epsilon_r$)	$N^{-1}m^{-2}C^2$
ζ_e	ionic friction factor	$N\ m^{-1}s$
η	dynamic viscosity	Pa s
θ	scattering angle	–
κ	inverse Debye length	m^{-1}
$\kappa(\underline{q})$	hydrodynamic lattice sum	–
λ	wavelength	m
λ	$\sqrt{\kappa^2 - i\omega/D_i}$	m^{-1}
λ_q^α	damping coefficient of the mode with wavevector $\underline{q}$ and polarization α	s^{-1}
Λ	characteristic damping	s^{-1}
μ_q^α	mass coefficient of the mode with	

	wavevector $\underline{q}$ and polarization α	–
ρ	density	kg m^{-3}
σ	particle cross-section	m^2
τ	correlation time	s
τ_s	sample time	s
φ	angle	–
ϕ	volume fraction	–
$\psi(\underline{r})$	screened Coulomb potential	V
ω	angular frequency	s^{-1}
ω_q^α	characteristic frequency of the mode with wavevector $\underline{q}$ and polarization α	s^{-1}
ω_κ	ionic frequency	s^{-1}
Ω	characteristic angular frequency	s^{-1}

Subscripts

b	Brownian
c	convective
i	ionic
i	incident
i,j,l	particle number
l	reciprocal lattice point number
nn	nearest neighbour
nnn	next nearest neighbour
q	normal mode
r	reference beam
s	scattered
x,y,z	x,y or z-component

Superscripts

k	projection on scattering vector $\underline{k}$
L	longitudinal
T	transverse
x,y,z,α,β	x,y,z,α or β-component
$\hat{}$	e.g. $\hat{r} \equiv \underline{r}/r$
*	complex conjugate

Summary

Colloidal particles immersed in a fluid exhibit Brownian motion. The random driving force of this motion is due to collisions of the thermally excited fluid molecules with the particles. The scattering of light off a system of particles and fluid is a prime tool for the study of Brownian motion. The fluctuating scattered light reveals the fluctuating particle positions. Therefore the statistical properties of the scattered light, which can be characterized by means of time correlation functions, contain information on Brownian motion. In this thesis two dynamic light scattering experiments on Brownian motion are described. In the first experiment the interaction between fluid flow and Brownian motion is studied. A special optical setup with two incident laser beams is employed to unravel the influences of Brownian motion and pure convection on the scattered light. The second experiment probes the dynamics of so-called colloidal crystals. Charged colloidal particles in a low ionic strength fluid can behave as solids; they form crystalline structures. The dispersion of Brownian crystal waves can be measured in a dynamic light scattering experiment.

After an introductory chapter, chapter 2 reviews the technique of dynamic light scattering. We distinguish between so-called homodyne and heterodyne detection of scattered light. In a homodyne experiment only scattered light is detected. Because the scattered intensity and not the scattered electric field is detected certain phase information is lost in this experiment. This phase information can be obtained in a heterodyne experiment where scattered light interferes on the detector with a reference beam, a so-called local oscillator. The research on colloidal crystals prompted us to develop a special optical setup for heterodyne experiments. In this setup the reference beam is guided through a single-mode optical fiber. Results of test experiments with this setup are presented in chapter 2.

A surprising phenomenon of Brownian motion in shear flow is the theoretical prediction that the mean-square displacement is proportional to time to the third power (diffusion has a mean-square displacement proportional to time, pure convection has mean-square displacement proportional to time squared). In a conventional dynamic light scattering experiment this prediction cannot be tested because the fluctuations of the scattered light are dominated by deterministic motion of the particles due to fluid flow, fluctuations due to

Brownian motion are obscured. The reason for this is that the characteristic times of both processes (Brownian motion and convection) in the experiment are widely separated. The smallest time belongs to convection, it obscures processes on larger time scales. A cross-correlation experiment, that is an experiment that determines the correlation between light scattered in two separate directions, can introduce a time shift which brings the Brownian motion time scale within sight. In chapter 3 results of cross-correlation experiments are presented. Cross-correlation functions were obtained by measuring autocorrelation functions of light scattered from the region within the flow where two incident laser beams cross. The results are in fair agreement with the theory. From a more practical point of view it is interesting that these experiments show the possibility of accurate point measurements of shear rates.

Under certain circumstances charged colloidal particles can form crystalline structures. The dynamics of these colloidal crystals is determined by relatively short-range electrostatic interactions and by hydrodynamic interactions; the moving particles exchange momentum through the fluid. Hydrodynamic interactions are long ranged. It appears that hydrodynamic interaction is more important in a lattice of Brownian particles than in random swarms of particles. Because the particles are arranged on a lattice explicit expressions for the frequency and damping of crystal waves initiated by Brownian motion can be derived. Hydrodynamic interaction and damping are intimately connected. There is a fundamental difference between the behaviour of longitudinal and transverse lattice waves. Longitudinal modes always show relative motion of fluid and particles. Therefore they are strongly damped. Long-wavelength transverse modes are characterized by coherent motion of fluid and particles and are weakly damped. Lattice parameters of colloidal crystals are of the order of 1 μm. Therefore crystallography can be done with visible light. Autocorrelation functions of light scattered by lattice waves contain information on the frequency and damping of these waves.

In chapter 4 the theory on colloidal crystals is reviewed. In chapter 5 the light scattering experiments are described and results are presented. To avoid detection of multiple scattered light the crystals are grown in a thin-film sample cell. The experiments were focussed on long-wavelength transverse modes. The results show that the walls of the sample cell have a strong impact on the dynamics of the crystal in regions of reciprocal space characterized by weak

damping. This discovery leads to a better understanding of discrepancies between theory and experiment observed earlier by other researchers. Furthermore it was possible to measure the damping of long-wavelength transverse modes directly, i.e. without interference of the elastic properties of the crystal. These measurements also showed significant wall-effects. A still unsolved problem is why longitudinal and transverse correlation functions have different shape. Longitudinal correlation functions are highly non-exponential while transverse correlation functions behave as the theoretically predicted exponential functions. This phenomenon shows that there is not yet a complete and adequate description of colloidal crystal dynamics.

In vloeistof gesuspendeerde colloïdale deeltjes voeren Brownse beweging uit. De drijvende kracht voor deze beweging is stochastisch van aard, ze is het gevolg van botsingen van de thermisch bewegende vloeistofmoluculen met de deeltjes. Verstrooiing van coherent licht aan een systeem van vloeistof en deeltjes is een methode om de dynamica van Brownse beweging te bestuderen. De positie-fluctuaties van de colloïdale deeltjes geven aanleiding tot fluctuaties van het strooilicht. De statistische eigenschappen van het strooilicht, welke kunnen worden gekarakteriseerd met behulp van tijdcorrelatiefuncties, bevatten daarom informatie over Brownse beweging. In dit proefschrift worden twee dynamische lichtverstrooiingsexperimenten aan Brownse deeltjes beschreven. Met het eerste experiment wordt de wisselwerking tussen Brownse beweging en stroming bestudeerd. Door gebruik te maken van een bijzondere optische configuratie met twee lichtbundels kunnen de invloeden op het verstrooide licht van pure convectie en Brownse beweging gescheiden worden. In het tweede experiment wordt de dynamica van zogenaamde colloïdale kristallen onderzocht. Onder bepaalde omstandigheden kunnen elektrisch geladen colloïdale deeltjes zich gedragen als een vaste stof; ze ordenen zich in een kristalrooster. De dispersie van Brownse roostergolven kan worden bepaald met behulp van dynamische lichtverstrooiing.

Na een inleidend hoofdstuk wordt in hoofdstuk 2 een beeld gegeven van de techniek van dynamische lichtverstrooiing. Er wordt onderscheid gemaakt tussen zogenaamde homodyne en heterodyne detectie van strooilicht. In een homodyn experiment wordt alleen strooilicht gedetecteerd. Omdat niet het elektrisch veld maar de intensiteit van het strooilicht wordt gedetecteerd gaat bepaalde fase-informatie verloren. Deze fase-informatie kan wel worden verkregen in een heterodyn experiment waarbij strooilicht op het detector-oppervlak interfereert met een referentie lichtbundel, een zogenaamde locale oscillator. Voor het onderzoek aan colloïdale kristallen werd een bijzondere optische configuratie voor het doen van heterodyne experimenten ontwikkelt waarbij de locale oscillator door een mono-mode optisch fiber wordt geleid. De resultaten van testexperimenten met deze configuratie zijn beschreven in hoofdstuk 2.

Een verrassend aspect van Brownse beweging in een stroming met een snelheidsgradiënt is de theoretische voorspelling dat de gemiddelde kwadratische verplaatsing van een Browns deeltje evenredig is met de tijd tot de derde macht (bij louter diffusie is de gemiddelde kwadratische verplaatsing evenredig met de tijd, bij convectie met de tijd in het kwadraat). Als men vervolgens deze voorspelling in een lichtverstrooiingsexperiment wil verifiëren blijkt dat een elementair experiment alleen uitspraken doet over convectieve deeltjes-bewegingen, niet over Brownse beweging. De reden hiervoor is dat de karakteristieke tijden van beide processen in het experiment ver uit elkaar liggen; de kleinste tijd behoort bij convectie, ze beheerst het experiment volledig. Een kruiscorrelatie experiment, dit is een experiment dat de correlatie bepaalt tussen licht dat wordt verstrooid onder twee verschillende hoeken, kan een tijdvertraging introduceren die het mogelijk maakt een beeld te krijgen van de fenomenen die zich afspelen op de tijdschaal van Brownse beweging. In hoofdstuk 3 worden resultaten van een dergelijk kruiscorrelatie experiment gepresenteerd. Kruiscorrelatiefuncties werden verkregen door het meten van autocorrelatiefuncties van het strooilicht afkomstig uit het gebied in de stroming waar twee invallende laserbundels elkaar snijden. De resultaten vertonen redelijke overeenstemming met de theorie. Vanuit een praktisch oogpunt is het zeer interessant dat deze experimenten nauwkeurige puntmetingen van snelheids-gradiënten mogelijk maken.

Elektrisch geladen colloïdale deeltjes kunnen onder bepaalde omstandigheden kristallijne structuren vormen. De dynamica van deze colloïdale kristallen wordt bepaald door over betrekkelijk korte afstanden werkende elektrostatische interacties en door hydrodynamische interacties; de vloeistof waarin de deeltjes zijn gesuspendeerd geeft de impuls van een deeltje door aan de omringende deeltjes. Hydrodynamische interacties werken over relatief grote afstanden. Het blijkt dat colloïdale deeltjes in een rooster veel sterkere hydrodynamische interacties aangaan dan deeltjes die willekeurig over de ruimte zijn verdeeld. Omdat de deeltjes zijn geordend in een rooster kunnen expliciete uitdrukkingen worden afgeleid voor de frequentie en demping van roostertrillingen die geïnitieerd worden door Brownse beweging. Hydrodynamische interactie en demping zijn nauw met elkaar verbonden. Er is een fundamenteel verschil tussen het gedrag van longitudinale en transversale roostergolven. Omdat longitudinale golven altijd gepaard gaan met relatieve beweging tussen vloeistof en deeltjes

zijn ze sterk gedempt. Lange transversale golven worden juist gekenmerkt door coherente beweging van deeltjes en vloeistof en worden daarom veel zwakker gedempt. De roosterafstand van colloïdale kristallen is typisch van de orde van 1 μm. Daardoor kan kristallografie worden gedaan met zichtbaar licht. Autocorrelatiefuncties van licht dat door roostergolven wordt verstrooid verschaffen informatie over de frequentie en de demping van de golven.

In hoofdstuk 4 wordt een overzicht gegeven van de theorie van colloïdale kristallen. In hoofdstuk 5 worden de lichtverstrooiingsexperimenten beschreven en worden resultaten gepresenteerd. Om meervoudige lichtverstrooiing te voorkomen worden de kristallen gegroeid in een dunne cel. De experimenten concentreren zich op lange transversale golven. Uit de resultaten blijkt dat de wanden van de cel sterke invloed hebben op de dynamica van het kristal in gebieden van de reciproke ruimte die gekenmerkt worden door een geringe demping. Door deze ontdekking kunnen eerder door anderen geconstateerde discrepanties tussen theorie en experiment beter worden begrepen. Verder bleek het mogelijk voor zeer kleine golfvectoren de demping van transversale golven direct te meten, dat wil zeggen zonder de tussenkomst van de elastische eigenschappen van het kristal. Ook de resultaten van deze metingen vertonen wandinvloeden. Nog onopgehelderd is de vraag waarom de vorm van longitudinale en transversale correlatiefuncties sterk verschillend is. Longitudinale correlatiefuncties vertonen in hoge mate niet-exponentieel gedrag terwijl transversale correlatiefuncties in zeer goede benadering de door de theorie voorspelde exponentiële vorm hebben. Dit fenomeen toont aan dat er nog geen volledige beschrijving van de dynamica van colloïdale kristallen voorhanden is.

Nawoord

De afgelopen vier en een half jaar heb ik me bewogen in een bijzondere wereld. Enerzijds waren er de fysische verschijnselen die ik heb bestudeerd. Dit proefschrift is de neerslag van die studie. Anderzijds was er de omgeving waarin het onderzoek is verricht. Vele mensen gaven gestalte aan die omgeving en zorgden voor een prettig en stimulerend klimaat. Zij leverden essentiële bijdragen aan het onderzoek en aan het op schrift stellen ervan. Ik ben hen daarvoor zeer dankbaar. In het bijzonder wil ik dank zeggen aan C.J. Arends, J.G.M. Niessen, P.P.J.M. Schram, J.C. Stouthart en W. van de Water.

Jos Derksen.

Stellingen bij het proefschrift van J.J. Derksen, 12 februari 1991.

1. De invloed van de wanden op de dynamica van een colloïdaal kristal in een dunne cel uit zich in de demping van de door Brownse beweging geïnitieerde kristalgolven die worden gekarakteriseerd door coherente beweging van deeltjes en vloeistof. Daarom zal deze demping in goede benadering kunnen worden beschreven met behulp van een model voor de demping van hydrodynamische fluctuaties in louter vloeistof begrensd door wanden.

   Dit proefschrift.

2. Het grote belang dat op het terrein van dynamische lichtverstrooiing wordt gehecht aan de beschrijving van fotoncorrelatiefuncties met twee of meer zogenaamde cumulanten is misplaatst. Men gaat voorbij aan het feit dat de inverse Laplacetransformatie een slecht geconditioneerd probleem is.

   J.G. McWhirter and E.R. Pike, J. Phys. A 11, 1729 (1978).

3. De numerieke oplossing en haar analytische benadering voor de sedimentatiesnelheid van elektrisch geladen colloïdale deeltjes in een vloeistof, beiden gevonden door Ohshima *et al.*, wijken minder sterk van elkaar af dan Schumacher en Van de Ven ons willen doen geloven.

   H. Ohshima, T.W. Healy, L.R. White and R.W. O'Brien, J. Chem. Soc., Faraday Trans. 2 80, 1299 (1984).

   G.A. Schumacher and T.G.M. van de Ven, Farady Discuss. Chem. Soc. 83, 75 (1987).

4. Compressibiliteit zorgt niet alleen voor een snelle relaxatie van de autocorrelatiefunctie voor de snelheid van een Browns deeltje in een vloeistof van de beginvoorwaarde $k_B T/m$ naar $k_B T/m^*$, waarbij m en m^* de massa's zijn van respectievelijk het deeltje zonder en met de helft van de verplaatste vloeistof, k_B de Boltzmann constante en T de absolute temperatuur, *maar ook* voor de opheffing van de $|\tau|^{-3/2}$-singulariteit van de autocorrelatiefunctie van de fluctuerende kracht op het deeltje, die volgt uit de theorie van Bedeaux en Mazur.

   D. Bedeaux and P. Mazur, Physica 76, 247 (1974).

   R. Zwanzig and M. Bixon, J. Fluid Mech. 69, 21 (1975).

5. Gezien het feit dat een stroming die gekenmerkt wordt door compactheid, een hoog Reynolds-getal en een laag Mach-getal adequaat beschreven kan worden in termen van werveldynamica is het verbazingwekkend dat Fletcher wervels gegenereerd door de interactie van de vrije straal met het labium in een orgelpijp als een onbelangrijk (tweede orde) effect meent te kunnen verwaarlozen.

   N.H. Fletcher, Ann. Rev. Fluid Mech. 11, 123 (1979).
   N.H. Fletcher and S. Thwaites, Scientific American 248, 84 (1983).

6. Mono-mode polarisatie behoudende optische fibers hebben een grote toekomst in dynamische lichtverstrooiingsexperimenten. Het feit dat dankzij deze fibers de laser en de rest van de optische configuratie mechanisch gescheiden kunnen worden kan de stabiliteit van de laatste zeer ten goede komen.

7. De mens zoekt naar het wezen der dingen. Zijn fantasie loopt hem daarbij voortdurend in de weg.

   Louis-Ferdinand Céline, Reis naar het einde van de nacht (G.A. van Oorschot, Amsterdam 1968).

8. Het zou veel ergernis en wellicht verkeersslachtoffers schelen als bromfietsen uitsluitend werden gebruikt door lieden waarvoor ze oorspronkelijk waren bedoeld. Daarom verdient het aanbeveling de minimum leeftijd waarop het is toegestaan een bromfiets te berijden te verhogen van 16 naar 65 jaar.